

Charles University  
Faculty of Mathematics and Physics

## Doctoral Thesis



**Veronica Goian**

### **Infrared spectroscopy of multiferroics**

Department of Dielectrics  
Institute of Physics  
Academy of Sciences of the Czech Republic

**Supervisor:** RNDr. Stanislav Kamba, CSc.

Study Programme: 4F3  
Physics of Condensed Matter and Materials Research

Prague 2011

*I would like to dedicate this work to my family which supported and encouraged me  
all this time.*

*I am among those who think that science has great beauty. A scientist in his laboratory is  
not only a technician: he is also a child placed before natural phenomena which impress  
him like a fairy tale.*

*Marie Curie-Skłodowska*

## **Acknowledgements**

Any work is not complete without the support and guidance of learned people. There are many people which I would like to thank and to express my sincere gratitude for their help and encouragement.

I would like firstly to express my deepest gratitude and to thank to my supervisor Stanislav Kamba for his patience guidance, useful critiques and encouragements of this research work and his guidance in this field of research.

It is also my pleasure to thank Dmitry Nuzhnyy, Volodymyr Skoromets and Christelle Kadlec for helping with THz measurements, Fedir Borodavka for Raman measurements, Viktor Bovtun for microwave measurements, Maxim Savinov for dielectric measurements and also, but not the least, Jan Prokleška from Faculty of Mathematics and Physics of the Charles University, for helping me with magnetic measurements. Furthermore, I would like to thank to Jan Petzelt, Petr Kužel and Jiří Hlinka for their suggestions and helpful discussions during my PhD studies.

I wish to thank also to M. Kittler and J. Bajgar from Optical Workshop in our Institute for polishing of all the samples which we investigated. Special thanks also to O. Pacherová, J. Drahoukoupil, X. Martí and F. Laufek for X-ray diffraction analysis of some samples, which I investigated.

I would like to express also my gratitude to the groups which provide us the samples, especially to Přemysl Vaněk from our Institute, to R. Pisarev from Ioffe Technical Institute, St. Petersburg, Russia and finally to Prof. D. Schlom from Cornell University. It is also my pleasure to thank to our colleagues K. Rushchanskii and M. Ležaič from Forschungszentrum Jülich, Germany for their theoretical calculations.

I would like to thank to my family for their support and patience as well as to my closest friends for their support and friendship.

Finally, I would like to acknowledge financial support of the Czech Science Foundation (Project 202/09/0682) and AVOZ 10100520. In addition, the contribution of my Ph.D. study has been supported last year by Czech Science foundation project 202/09/H0041 and by project SVV-2010-261303 from Faculty of Mathematics and Physics of Charles University.

## **Declaration and confession**

I declare that I carried out this doctoral thesis independently, and only with the cited sources, literature and other professional sources.

I understand that my work relates to the rights and obligations under the Act No. 121/2000 Coll., the Copyright Act, as amended, in particular the fact that the Charles University in Prague has the right to conclude a license agreement on the use of this work as a school work pursuant to Section 60 paragraph 1 of the Copyright Act.

In Prague, on September 12, 2011

Veronica Goian

## Abstrakt v českém jazyce

**Název doktorské práce: Infračervená spektroskopie multiferoik**

**Autor:**Veronica Goian

**Ústav:** Oddělení dielektrik, Fyzikální ústav AV ČR v.v.i, Na Slovance 2, 182 21, Praha 8

**Školitel:** RNDr. Stanislav Kamba, CSc.

**Školící pracoviště:** Oddělení dielektrik, Fyzikální ústav AV ČR v.v.i, Na Slovance 2, 182 21, Praha 8

**Konzultanti:** Ing. Dmitry Nuzhnyy, Ph.D. a RNDr. Jan Prokleška, Ph.D.

### Abstrakt:

Pomocí infračervené spektroskopie jsme studovali řadu multiferoických a magnetoelektrických látek. Náš výzkum byl často kombinován radiofrekvenčními, mikrovlnnými, terahertzovými, ramanovskými a strukturními měřeními mých kolegů, jakož i magnetickými, a elastickými studii, na kterých jsem se podílela. Naším hlavním cílem bylo komplexní studium kvantově-paralelektrického antiferomagnetika  $\text{EuTiO}_3$  ve formě krystalů, keramik i tenkých vrstev. V objemových vzorcích  $\text{EuTiO}_3$  jsme objevili u 300 K antiferodistortivní přechod z kubické  $Pm\bar{3}m$  do tetragonální  $I4/mcm$  struktury. Nízkoteplotní dielektrické vlastnosti v  $\text{EuTiO}_3$  jsme vysvětlili anomálním teplotním chováním polárních fononů. Velký a anizotropní magnetoelektrický jev, který jsme našli v  $\text{EuTiO}_3$ , jsme objasnili a experimentálně potvrdili pozorováním ladění fononových frekvencí vnějším magnetickým polem. Naše studia tahově napnutých vrstev  $\text{EuTiO}_3$  odhalila u 250 K posuvný ferroelektrický fázový přechod. Naši američtí kolegové objevili pod 4.2 K feromagnetické uspořádání ve stejných tenkých vrstvách. Tím jsme experimentálně potvrdili nedávno teoreticky předpovězenou novou možnost přípravy silných ferroelektrických feromagnetik se silnou magnetoelektrickou vazbou.

Multiferoické keramiky  $\text{Eu}_{0.5}\text{Ba}_{0.5}\text{TiO}_3$  a  $\text{Eu}_{0.5}\text{Ba}_{0.25}\text{Sr}_{0.25}\text{TiO}_3$  keramiky jsme navrhli použít pro hledání elektrického dipólového momentu elektronu. Zároveň jsme určili magnetické a ferroelektrické fázové diagramy těchto nových multiferoik. V IČ a THz spektrech jsme identifikovali ferroelektrické měkké módy, které vyvolávají posuvné ferroelektrické přechody v těchto materiálech.

V THz a IČ spektrech  $\text{YMnO}_3$  jsme objevili kromě antiferomagnetické resonance další kvalitativně nové excitace, které mají nižší frekvence než optické fonony. Ty jsme vysvětlili pomocí multifononové a paramagnon-fononové absorpce.

V antiferoelektrickém  $\text{Bi}_{0.85}\text{Nd}_{0.15}\text{FeO}_3$  jsme našli fononové anomálie i silnou dielektrickou relaxaci v THz oblasti, které vysvětlují pokles permittivity při fázovém přechodu. U  $\text{Ba}_{0.5}\text{Sr}_{1.5}\text{Zn}_2\text{Fe}_{12}\text{O}_{22}$  se strukturou Y-hexaferitu jsme porovnávali dielektrické, magnetické a fononové chování v keramických a monokrystalických vzorcích. Mimo jiné jsme zjistili, že žíhání vzorků má pozitivní vliv na rozšíření feroelektrické fáze, která je indukována vnějším magnetickým polem.

**Klíčová slova:** multiferoika, feroelektrické měkké módy, magnony, infračervená spektroskopie.

## Abstract in English

**Title:** Infrared Spectroscopy of Multiferroics

**Author:** Veronica Goian

**Institute:** Department of Dielectrics, Institute of Physics of the Academy of Sciences, Na Slovance 2, 182 21 Prague 8

**Advisor of the doctoral work:** RNDr. Stanislav Kamba, CSc.

**Training institute:** Department of Dielectrics, Institute of Physics of the Academy of Sciences, Na Slovance 2, 182 21 Prague 8

**Consultants:** Ing. Dmitry Nuzhnyy, Ph.D. and RNDr. Jan Prokleška, Ph.D.

**Abstract:** We have investigated numerous multiferroic and magnetoelectric materials mainly using infrared (IR) spectroscopy. Nevertheless, the studies were frequently combined with radio-frequency, microwave, THz, Raman and structural measurements provided by our colleagues, as well as by magnetic and elastic investigations, where we participated. Our main aim was the complex study of quantum-paraelectric antiferromagnet  $\text{EuTiO}_3$  in the form of crystals, ceramics and thin films. Near 300 K we have discovered an antiferrodistorive phase transition from cubic  $Pm\bar{3}m$  to tetragonal  $I4/mcm$  structure in bulk  $\text{EuTiO}_3$  and explained its low-frequency dielectric properties by anomalous polar phonon behavior. Large and anisotropic magnetodielectric effect, which we found in  $\text{EuTiO}_3$ , was successfully explained and experimentally confirmed by observation of tuning of phonon frequency with magnetic field. Our IR studies of tensile strained  $\text{EuTiO}_3$  thin films revealed a displacive ferroelectric phase transition near 250 K. Our American colleagues revealed the ferromagnetic order below 4.2 K in the same strained  $\text{EuTiO}_3$  thin film. In such way we have experimentally confirmed recent theoretical prediction of a new route for preparation of strong ferroelectric ferromagnets with a strong magnetoelectric coupling.

We have suggested to use multiferroic  $\text{Eu}_{0.5}\text{Ba}_{0.5}\text{TiO}_3$  and  $\text{Eu}_{0.5}\text{Ba}_{0.25}\text{Sr}_{0.25}\text{TiO}_3$  ceramics for the search of electric dipole moments of electrons. We also determined the magnetic and ferroelectric phase diagram in these new multiferroics. In IR and THz spectra we have found the ferroelectric soft modes driving the displacive phase transitions in these compounds.

In antiferroelectric  $\text{Bi}_{0.85}\text{Nd}_{0.15}\text{FeO}_3$  we have found phonon and dielectric relaxation anomalies explaining the drop-down of permittivity below the phase transition. In the case of Y-type hexaferrite  $\text{Ba}_{0.5}\text{Sr}_{1.5}\text{Zn}_2\text{Fe}_{12}\text{O}_{22}$ , we have compared dielectric and phonon properties of

ceramics and single crystals. We have found that the temperature annealing has positive influence on a broadening of ferroelectric region induced by an external magnetic field.

**Keywords:** multiferroics, ferroelectric soft modes, magnons, infrared spectroscopy.



## Contents

Aknowledgements	<i>iii</i>
Declaration and confession	<i>iv</i>
Abstrakt v českém jazyce	<i>v</i>
Abstract in English	<i>vii</i>
Contents	<i>ix</i>
Preface	1
<b>1. Magnetolectrics and Multiferroics</b>	
1.1. Passing through time	2
1.2. ...and a bit of theory...	3
1.3. Type-I multiferroics	4
1.3.1. Multiferroic perovskites	4
1.3.2. Compounds in which ferroelectricity is induced by lone pair	5
1.3.3. Compounds where the ferroelectricity originates from charge ordering	6
1.3.4. Compounds with „geometric“ ferroelectricity	6
1.4. Type-II multiferroics	7
1.4.1. Multiferroics with spiral magnetic ordering	8
1.4.2. Type-II multiferroics with collinear magnetic structure	9
1.4.3. Type-II multiferroics where the ferroelectricity induces a weak magnetic order	11
1.5. Ferrotoroidic order	11
1.6. Some other types of multiferroics	12
1.7. Applications	14
<b>2. Theoretical backgrounds</b>	
2.1. Interaction of lattice dynamics with electromagnetic radiation	16
A. The Response of Transverse Optical (TO) phonons	18
B. Longitudinal Optical (LO) phonons	20

2.2. Ferroelectricity	21
2.2.1 General properties of ferroelectric materials	21
2.2.2 Classification of ferroelectric crystals	23
2.2.3 The concept of soft mode and critical dynamics near ferroelectric phase transitions	24
2.3. Elementary excitations in magnetic material	26
2.3.1. General descriptions	26
2.3.2. Spin waves in ferromagnets: Magnons	27
2.3.3. Antiferromagnetic and ferromagnetic resonances	29
<b>3. Experimental techniques</b>	
3.1. Infrared spectroscopy	33
3.1.1. Interferogram	33
3.1.2. Models for evaluation of complex dielectric function in IR region	34
3.1.3. Advantages and disadvantages of Fourier Transform spectroscopy	40
3.1.4. Experimental setup	41
3.2. Time domain THz spectroscopy	43
3.2.1. THz radiation	43
3.2.2. Sources of THz radiation	44
3.2.3 Time domain THz spectroscopy	44
3.3. Techniques for magnetic measurements	46
3.3.1. Introduction in magnetic measurements	46
3.3.2. SQUID	46
3.3.3. Measurements of AC susceptibility in PPMS	47
<b>4. Our experimental results</b>	
4.1. List of investigated materials and their preparation	49
4.2. $\text{EuTiO}_3$	51
4.3. $\text{Eu}_{0.5}\text{Ba}_{0.5}\text{TiO}_3$ and $\text{Eu}_{0.5}\text{Ba}_{0.25}\text{Sr}_{0.25}\text{TiO}_3$ ceramics	61
4.3.1. $\text{Eu}_{0.5}\text{Ba}_{0.5}\text{TiO}_3$ ceramics	61
4.3.2. $\text{Eu}_{0.5}\text{Ba}_{0.25}\text{Sr}_{0.25}\text{TiO}_3$ ceramics	66

4.4. EuTiO <sub>3</sub> thin films	69
4.4.1. Biaxially tensile strained EuTiO <sub>3</sub> thin films	70
4.4.2. Compressively strained EuTiO <sub>3</sub> thin films	77
4.4.2.1. EuTiO <sub>3</sub> /LSAT	78
4.4.2.2. EuTiO <sub>3</sub> /LaAlO <sub>3</sub>	84
4.4.2.3. EuTiO <sub>3</sub> /NdGaO <sub>3</sub>	87
4.5. Hexagonal manganites	90
4.5.1. Y <sub>1-x</sub> Eu <sub>x</sub> MnO <sub>3</sub> ceramics, x=0-0.2	91
4.5.2. YMnO <sub>3</sub> single crystal	95
4.5.3. InMnO <sub>3</sub> ceramics	102
4.6. SrMnO <sub>3</sub> ceramics	105
4.7. Sr <sub>2</sub> TiMnO <sub>6</sub> ceramics	107
4.8. Nd substituted BiFeO <sub>3</sub> (Bi <sub>0.85</sub> Nd <sub>0.15</sub> FeO <sub>3</sub> )	108
4.9. Ba <sub>0.5</sub> Sr <sub>1.5</sub> Zn <sub>2</sub> Fe <sub>12</sub> O <sub>22</sub> with Y-type hexaferrite structure	118
<b>5. Conclusions</b>	125
<b>Bibliography</b>	127
<b>Publications</b>	133
List of Tables	135
List of variables	136
List of abbreviations	137



## Preface

Multiferroics are materials which exhibit simultaneously some magnetic and ferroelectric order. They might be the key to the future for new generation of memory devices due to the presence of magnetoelectric coupling, which allows in principle a switching of the ferroelectric state with magnetic field and vice versa. Unfortunately, nowadays there are known only few materials in the nature exhibiting multiferroic order above room temperature.

In our work we try to understand the origin of magnetoelectric coupling in various magnetoelectric materials and search for new multiferroic materials. We demonstrate a new route for preparation of new strong ferroelectric ferromagnets using a mechanical strain in the thin films. Besides it we suggest to use some multiferroic materials for the search of electric dipole moment of electron with up to now not reached sensitivity. Discovery of electric dipole moment of electron would have significant impact on proving of various particle theories going beyond the standard model.

In this work we investigate multiferroic and magnetoelectric materials using mainly far infrared and THz spectroscopy.

The thesis is divided in five chapters, as follows:

- Chapter 1 gives an introduction in multiferroics and magnetoelectrics materials. It is an overview of what is known in this field up to now;
- Chapter 2 presents the theoretical concepts about phonons and magnons;
- Chapter 3 describes our used experimental techniques, i.e. the Fourier Transform Infrared (FTIR) spectrometer, time domain THz spectrometer and the magnetometer techniques e.g SQUID and PPMS;
- In Chapter 4 we present the experimental results and compare them with theoretical predictions or with some other results from literature. The main results are focused on bulk  $\text{EuTiO}_3$  and strained  $\text{EuTiO}_3$  thin films, but also on other materials as: bulk  $\text{YMnO}_3$  ceramics and single crystals,  $\text{InMnO}_3$ ,  $\text{Sr}_2\text{TiMnO}_6$ ,  $\text{Bi}_{0.85}\text{Nd}_{0.15}\text{FeO}_3$  and Y-type hexaferrite  $\text{Ba}_{0.5}\text{Sr}_{1.5}\text{Zn}_2\text{Fe}_{12}\text{O}_{22}$ ;
- Chapter 5 shows the conclusions of the present work.

# CHAPTER 1 Magnetoelectrics and Multiferroics

## 1.1 Passing through time ...

The purpose of this chapter is to make an overview of magnetoelectric (ME) and multiferroic materials. Two outstanding events sealed the beginnings of ME effect (i.e. influence of electric field on magnetization or impact of magnetic field on electric polarization): a) Röntgen in 1888 discovered that a moving dielectric placed in electric field became magnetized<sup>1</sup> - followed by reversed effect much later<sup>2</sup> and b) in 1894 P. Curie pointed out the existence of intrinsic ME coupling in crystals due to symmetry considerations<sup>3</sup>. However, many decades passed when first successful measurement of ME behavior occurred. One important step for understanding of this behavior was when it was proposed in 1959 that this phenomenon is allowed only in time asymmetric media<sup>4</sup> with breaking of time reversal symmetry.

Dzyaloshinskii predicted theoretically<sup>5</sup> and then Astrov confirmed experimentally that antiferromagnetic  $\text{Cr}_2\text{O}_3$  exhibits a linear ME effect i.e. electric field induced magnetization.<sup>6,7</sup> One year later was experimentally proved that magnetic field can induce polarization.<sup>8,9</sup> After these experiments, the scientific community started intensively search for new ME materials. The tensor form of the linear ME coupling coefficient ( $\alpha_{ij}$ ) was first determined by Indenbom, but with an incomplete list of point groups.<sup>10</sup> Complete tables of point groups which allowed linear ME effect can be found in several textbooks<sup>11,12</sup> and reviews<sup>13</sup>. The largest ME coupling were observed in  $\text{LiCoPO}_4$ <sup>14</sup>, yttrium iron garnet (YIG) films<sup>15</sup> and  $\text{TbPO}_4$ <sup>16</sup>, but still very weak to be useful in applications e.g. in ME devices like memories, sensors, actuators, etc.

The situation changed when it was observed that some materials can have two or more “ferroic” orders and can coexist simultaneously in absence of external fields. In 1994, Schmidt called these materials multiferroics.<sup>17</sup> The original definition in that time was “... *those materials, having two or more primary ferroics properties in the same phase*” where primary ferroics mean ferroelectric, ferromagnetic, ferroelastic and much more recently ferrotoroidal materials. The definition suffered some adjustments during last years, and today, the term multiferroic is mostly used for materials, which are simultaneously magnetically and ferroelectrically ordered.

The first multiferroics (e.g.  $\text{PbFe}_{1/2}\text{Nb}_{1/2}\text{O}_3$  and  $\text{PbFe}_{1/2}\text{Ta}_{1/2}\text{O}_3$ <sup>18</sup>) were obtained in 1959. Today more than 100 single phase multiferroics are known. However, in natural form crystallizes only two of them:  $\text{Fe}_3\text{B}_7\text{O}_{13}\text{Cl}$  and  $\text{Mn}_3\text{B}_7\text{O}_{13}\text{Cl}$ <sup>19</sup>. All others were prepared in labs by different methods. Recently, in 2003 it was discovered a new class of multiferroics (e.g.  $\text{TbMnO}_3$ <sup>20</sup>,  $\text{DyMnO}_3$ <sup>21</sup>) in which electric polarization is induced by a special magnetic ordering of spins.

## 1.2 ...and a bit of theory....

By definition, the ME effect describes the coupling between electric and magnetic field in matter or better said induction of magnetization ( $M$ ) by an electric field ( $E$ ) or polarization ( $P$ ) generated by a magnetic field ( $H$ ). Thermodynamically, this effect can be understood within the Landau theory framework by expansion of free energy for a ME system.<sup>22</sup> In this case we have

$$F(E, H) = F_0 - P_i^s E_i - M_i^s H_i - \frac{1}{2} \varepsilon_0 \varepsilon_{ij} E_i E_j - \frac{1}{2} \mu_0 \mu_{ij} H_i H_j - \alpha_{ij} E_i E_j - \frac{1}{2} \beta_{ijk} E_i H_j H_k - \frac{1}{2} \gamma_{ijk} H_i E_j E_k - \frac{1}{4} \delta_{ijkl} H_i H_j E_k E_l - \dots \quad (1.1)$$

where  $F_0$  is the ground state free energy, ( $i, j, k, l$ ) are the subscripts for those four components of a variable in spatial coordinates,  $E_i$  and  $H_i$  are the components of the electric  $\mathbf{E}$  and magnetic field  $\mathbf{H}$ ,  $P_i^s$  and  $M_i^s$  are the components of spontaneous polarization and magnetization,  $\varepsilon_0$  and  $\mu_0$  are the dielectric permittivity and magnetic permeability, respectively, in vacuum,  $\varepsilon_{ij}$  and  $\mu_{ij}$  are the second-order tensors of dielectric permittivity and magnetic permeability,  $\alpha_{ij}$  are the coefficients of linear ME tensor,  $\beta_{ijk}$  and  $\gamma_{ijk}$  are the third order tensors describing quadratic coupling and  $\delta_{ijkl}$  is the fourth order tensor expressing biquadratic coupling.

After derivation of the free energy, we can obtain the polarization

$$P_i(E, H) = -\frac{\partial F}{\partial E_i} = P_i^s + \varepsilon_0 \varepsilon_{ij} E_j + \alpha_{ij} H_j + \frac{1}{2} \beta_{ijk} H_j H_k + \gamma_{ijk} H_i E_j + \frac{1}{4} \delta_{ijkl} H_k H_j E_l \quad (1.2)$$

and the magnetization

$$M_i(E, H) = -\frac{\partial F}{\partial H_i} = M_i^s + \mu_0 \mu_{ij} H_j + \alpha_{ij} E_j + \beta_{ijk} H_j E_i + \frac{1}{2} \gamma_{ijk} E_j E_k + \frac{1}{4} \delta_{ijkl} H_j E_k E_l \quad (1.3)$$

The linear ME coefficient  $\alpha_{ij}$  is limited by the relation<sup>23</sup>

$$\alpha_{ij}^2 < \varepsilon_{ii} \mu_{jj} \quad (1.4)$$

Where  $\varepsilon_{ij}$  and  $\mu_{ij}$  are permittivity and magnetic permeability, respectively.

The ME effect in single phase compound is often small to be practically applicable. In order to obtain a high value of ME coefficient, we need compound with high electric and magnetic susceptibilities. It is well known that ferroelectric/ferromagnets have the highest value of dielectric/magnetic susceptibility. Therefore it is believed that multiferroic materials with ferroelectric and magnetic order will have the highest ME coupling. Nevertheless, in this stage should be stressed, that not all multiferroic materials do not automatically fulfill the basic condition for linear ME effect, i.e. the broken time symmetry. Anyway, the quadratic and biquadratic ME effect is less symmetry restricted and in some multiferroics the nonlinear ME coupling can reach comparable values with the linear ME materials.

Khomskii proposed in the review<sup>24</sup> two general groups (or classes) of multiferroics. First group is called *type-I multiferroics*, where the ferroelectricity with rather large spontaneous polarization (of order 10-100  $\mu\text{C}/\text{cm}^2$ ) appears usually at high temperatures and magnetic order occurs below ferroelectric  $T_C$ . The second group is called *type-II multiferroics* where the special ordering of spins induces ferroelectricity with rather low polarization implying strong ME.

### 1.3 Type-I multiferroics

In this category, we can distinguish four groups of compounds: multiferroics with perovskite structure, compounds with ferroelectricity induced by lone pair electrons, materials with ferroelectricity originating from charge orderings and the last one compound with geometric ferroelectricity. A brief description of each group can be found below:

#### 1.3.1 Multiferroic perovskites

It is the most intensively investigated class of multiferroics. During the time there were a lot of discussions about the mechanism of ferroelectricity and how the polarization can interplay with magnetic order. One of the problems is that ferroelectricity and magnetism seems to be mutually exclusive. The reason is the magnetism requires a partially filled  $d$  shell of transition metals (TM) whereas the ferroelectrics should have  $d$ -shell empty.<sup>25</sup> On the other hand, the hybridization between B-site cations and the anions (i.e. covalent bond) in ferroelectrics can be seen as the virtual hopping of electrons from oxygen filled  $p$ -shell to the empty  $d$ -shell of the transition metal



ion. In contrast, to have magnetism, the uncompensated spin exchange interaction between adjacent magnetic ions induces the long range spin order and macroscopic magnetization.

The apparent impossibility to fulfill simultaneous both conditions for magnetic and ferroelectric order was overcome when researchers prepared perovskites  $ABO_3$ , where the B magnetic TM ions with  $d$  electrons were partially replaced with ferroelectrically active TM ions with  $d^0$  configurations keeping the perovskite structure stable. In such way appeared already in 1959  $Pb(Fe^{3+}_{1/2}Nb^{5+}_{1/2})O_3$  (PFN) and  $PbFe_{1/2}Ta_{1/2}O_3$  (PFT)- multiferroics- in which  $Nb^{5+}$ ,  $Ta^{5+}$  ions are ferroelectric cations and  $Fe^{3+}$  ions are magnetically active. In PFN, Néel temperature is around 143 K and ferroelectric Currie temperature is approximately 385 K. Unfortunately, the coupling between magnetic and ferroelectric order is rather weak in PFN and PFT materials because the ferroics orders originate from different kinds of ions.

### ***1.3.2 Compounds in which ferroelectricity is induced by lone pair electrons***

In this category belong perovskites  $BiFeO_3$  (see Fig.1.1),  $BiMnO_3$  and  $PbVO_3$  where  $Bi^{3+}$  and  $Pb^{2+}$  play a major role in origin of ferroelectricity. In these compounds,  $Bi^{3+}$  and  $Pb^{2+}$  have 6s shell with two outer electrons which do not participate at chemical bonding i.e. they order in one direction with certain mixture of  $p$  orbitals. Therefore, they are called ***lone pairs or dangling bonds***<sup>26,27,28</sup> (Fig.1.1). The most studied single-phase multiferroic is bismuth ferrite ( $BiFeO_3$ ) because its polarization, ferroelectric  $T_C$  and antiferromagnetic  $T_N$  are pretty high ( $P_S \sim 90 \mu C cm^{-2}$ ,  $T_C = 1120 K$ ,  $T_N = 643 K$ ).<sup>29,30</sup> The magnetic structure consist from a spiral spin structure in which the antiferromagnetic axis rotates through the crystal with an incommensurate long-wavelength period of 620 Å.<sup>31</sup> This ordering inhibits the linear ME effect in  $BiFeO_3$ . A strong ME coupling and a significant magnetization were observed in epitaxial thin film suggesting that the spiral structure can be suppressed.<sup>32</sup> Nevertheless, the magnetic structure and the origin of large magnetization are still unclear in thin film form.<sup>32</sup> Rather large ME coupling, comparable with spin-induced multiferroics, was observed in  $BiFeO_3$  at high magnetic fields above 17 T, where the magnetic structure changed.<sup>33</sup>

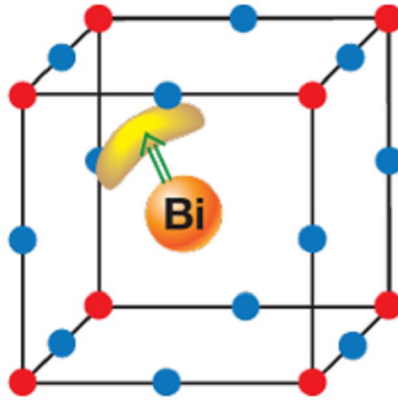


Fig. 1.1. The sketch of ordering of lone pairs electrons (yellow lobes) in  $\text{BiFeO}_3$ . Red points are Fe ions and blue points are oxygens (after Ref. 24)

### 1.3.3 Compounds where the ferroelectricity originates from charge ordering

These are compounds containing transition metal ions with different valences. We can enumerate  $\text{Pr}_{1/2}\text{Ca}_{1/2}\text{MnO}_3$ <sup>34</sup>,  $\text{LuFe}_2\text{O}_4$ <sup>35</sup>. In this compound the ferroelectricity has *electronic* origin where the charge carrier become localized at low temperatures and form periodic structure (ex.  $\alpha\text{-Fe}_3\text{O}_4$  where below so-called Verwey transition around 125 K, the charge of iron ions orders in complex pattern<sup>36</sup>).

In  $\text{Pr}_{1/2}\text{Ca}_{1/2}\text{MnO}_3$  was suggested three kinds of charge orderings e.g. checkerboard pattern.<sup>34</sup> There are some models which try to explain how can appear ferroelectricity in such materials but it is still not completely clarified.

### 1.3.4 Compounds with “geometric” ferroelectricity

In this category enter hexagonal manganites ( $\text{RMnO}_3$ ,  $\text{R}=\text{Sc}, \text{Y}, \text{Yb}, \text{In}, \text{Yb}$ ). One of the most studied materials from this class of materials is  $\text{YMnO}_3$  (Fig.1.2). Its ferroelectricity is caused by tilting of the rigid  $\text{MnO}_5$  block and as result the oxygens move close to Y ions.<sup>37</sup> The Néel temperatures  $T_N$  are generally below 100 K in  $\text{RMnO}_3$ , but strong spin-phonon coupling was frequently revealed in phonon spectra near  $T_N$  which is responsible for an anomalous decrease of dielectric permittivity seen below  $T_N$ .<sup>38</sup>

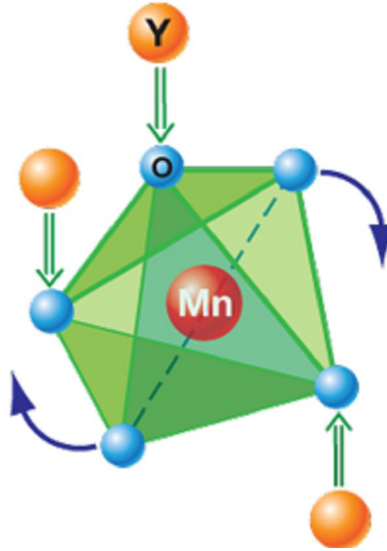


Fig. 1.2 Schematic picture of appearance of geometric ferroelectricity in  $\text{YMnO}_3$  due to tilting of a rigid  $\text{MnO}_5$  octahedra (after Ref. 24).

In literature, there are many other multiferroics of the type I, but we do not describe them here due to lack of space. It can be mentioned: fluorides<sup>39</sup> ( $\text{BaMF}_4$ ,  $M=\text{Mg}, \text{Mn}, \text{Co}, \text{Ni}, \text{Zn}$ ) and boracites ( $\text{M}_3\text{B}_7\text{O}_{13}\text{X}$ ,  $M= \text{Cr}, \text{Mn}, \text{Fe}, \text{Co}, \text{Cu}, \text{Ni}$  and  $\text{X}=\text{Cl}, \text{Br}, \text{I}$ ).<sup>40,41</sup>

## 1.4 Type-II Multiferroics

This group of compounds was discovered in 2003. Generally, the ferroelectricity appears due to certain magnetic order which induces a breaking of the centre of symmetry, a shift of some cations and appearance of an electric polarization. Here, we distinguished two sub classes of type-II multiferroics:

- 1) the magnetic frustration is the source of spiral magnetic ordering in insulators, and the ferroelectricity can arise in such systems ( $\text{TbMnO}_3$ ,  $\text{GdMnO}_3$ ,  $\text{DyMnO}_3$ , etc.) due to inverse Dzyaloshinskii-Moriya (DM) interaction describing a coupling of non-parallel spins.
- 2) The collinear magnetic order can create a polarization via exchange striction. Typical examples of such materials are  $\text{Ca}_3\text{CoMnO}_6$  and  $\text{TbMn}_2\text{O}_5$ .

### 1.4.1 Multiferroics with spiral magnetic ordering

The group is composed mainly by orthorhombic rare-earth manganites  $\text{RMnO}_3$  where R=Y, Tb, Gd, Dy, but also  $\text{Ni}_3\text{V}_2\text{O}_6$  enters in this class. All known multiferroic manganites with orthorhombic  $Pbnm$  perovskite structure are so called pseudo-proper ferroelectrics, because the polarization is a secondary order parameter induced by a magnetization as the primary order parameter.<sup>42,43</sup> In such case the inversion space symmetry is broken by some complex spiral magnetic ordering.

In order to understand this mechanism we consider  $\text{TbMnO}_3$ <sup>20</sup>. It has a antiferromagnetic phase transition at  $T_N= 41$  K where the magnetic structure has form of a sinusoidal spin wave (all the spins have the same size, but local magnetic moment varies periodically in the space) with a modulation wave vector  $(0, k, 1)$  where wavenumber  $k$  ( $\sim 0.29$ ) has incommensurate value at  $T_N$  along  $b$  axis. Below 28 K the structure changes in such way that moment describes an elliptic modulated cycloid<sup>44</sup>. In this case, the wavevector  $k$  ( $=1/3$ ) becomes commensurate. It was proved experimentally and theoretically explained that spiral cycloid structure induces a net polarization parallel to  $c$  direction via spin-orbit interaction.<sup>42</sup> It is important to note that the magnetic structure is collinear in paraelectric antiferromagnetic phase, while in ferroelectric phase shows a noncollinear cycloidal spiral spin structure.<sup>45</sup> The mechanism is ascribed by inverse DM interaction. The non-collinear magnetic alignment in the Mn-O-Mn bonds creates off-centrosymmetric displacements of the oxygen ions. One has to stress one thing: Due to the fact that the ferroelectric polarization creates due to special magnetic order, which can be influenced by external magnetic field, direction of the polarization can be easily changed by magnetic field. Actually the rotation of polarization from initial  $c$  direction (without magnetic field) to the  $a$  direction was observed after applying of a magnetic field over 5 T along the  $b$  axis.<sup>20,46</sup> The polarization  $\mathbf{P}$  is given by the relation<sup>47,48</sup>

$$\mathbf{P} \sim r_{ij} \times [\mathbf{S}_i \times \mathbf{S}_j] \sim [\mathbf{Q} \times \mathbf{e}], \quad (1.5)$$

where  $r_{ij}$  is the vector connecting neighboring spins  $\mathbf{S}_i$  and  $\mathbf{S}_j$ ,  $\mathbf{Q}$  is the wavevector describing the spiral and  $\mathbf{e} \sim [\mathbf{S}_i \times \mathbf{S}_j]$  is the spin rotation axis. The microscopic mechanism of the polarization is connected with the spin-orbit interaction.

The mechanism of appearance of polarization is similar also in  $\text{DyMnO}_3$ .<sup>49</sup> This compound exhibits also polarization flop from  $\mathbf{P} \parallel c$  to  $\mathbf{P} \parallel a$  by applied magnetic field along the  $b$  axis. Similar mechanism was described also in Kagome staircase  $\text{Ni}_3\text{V}_2\text{O}_6$ .<sup>50</sup> Another compound

which belongs in this category is Y-hexaferrite  $\text{Ba}_{0.5}\text{Sr}_{1.5}\text{Zn}_2\text{Fe}_{12}\text{O}_{22}$ .<sup>51</sup> The induced polarization can also be explained by DM mechanism. Unfortunately, the values of the electric polarization achieved in spin-induced ferroelectrics are three or four orders of magnitude smaller than in multiferroics with traditional ferroelectricity (Type-I multiferroics).

#### ***1.4.2 Type II multiferroics with collinear magnetic structure***

The polarization in this case is created by a collinear arrangement of spins without involving of spin-orbit interaction. The exchange striction associated with symmetric superexchange interaction plus charge-ordered state can also induce ferroelectricity.<sup>52</sup> In this case, the magnetic order is formed by one-dimensional Ising spin chain ( $\uparrow\uparrow\downarrow\downarrow$ ) with competing nearest-neighbour ferromagnetic interaction ( $J_{FM}$ ) and next nearest-neighbour antiferromagnetic interaction ( $J_{AFM}$ ). The exchange constants must fulfill an inequality for such ordering of spins:  $|J_{AFM} / J_{FM}| > 1/2$ . If the magnetic ions align alternatively along the chain, the exchange striction associated with the symmetric superexchange interaction shortens the bonds between parallel spins, while stretches those between antiparallel spins. This arrangement breaks the inversion symmetry and an electric polarization is produced along the chain direction.

An example of these materials is  $\text{Ca}_3\text{CoMnO}_6$ <sup>53</sup> (see Fig.1.3) where the exchange striction arises from transition metal ions with different valences ( $\text{Co}^{2+}$  and  $\text{Mn}^{4+}$ ).

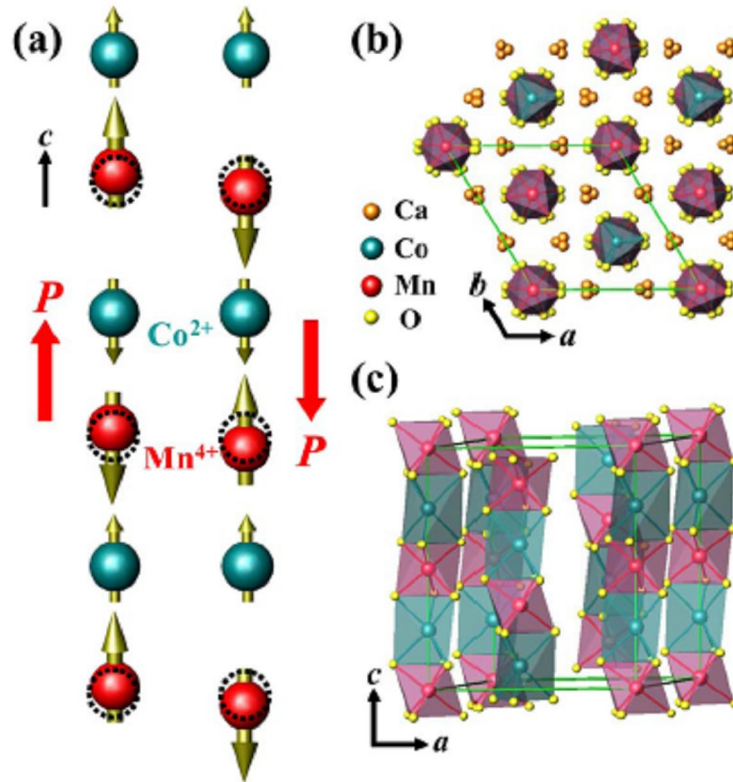


Fig. 1.3. The Ising chain of spin configuration and alternating ionic order in  $\text{Ca}_3\text{CoMnO}_6$ <sup>53</sup>

In this group enters also another important type of perovskite compounds  $\text{RMn}_2\text{O}_5$ , where  $R = \text{Tb, Dy, Y, Er}$  which exhibits similar behavior.<sup>42</sup> For example  $\text{TbMn}_2\text{O}_5$  belongs to the orthorhombic space group of  $Pbam$  hosting  $\text{Mn}^{3+}$  ( $S=2$ ) ions surrounded by oxygen pyramids and  $\text{Mn}^{4+}$  ( $S=3/2$ ) ions surrounded by oxygen octahedra. Along the  $c$  axis, the Mn spins are arranged in the five-spin loop:  $\text{Mn}^{4+}-\text{Mn}^{3+}-\text{Mn}^{3+}-\text{Mn}^{4+}-\text{Mn}^{3+}$ . Experimentally, it was found that this compound exhibits several complex magnetic phase transitions and ferroelectric transitions accompanied by the appearance of electric polarization and dielectric anomalies along the  $b$ -axis.<sup>54</sup>

However, by theoretical calculations the space group of this material does not allow spatial-inversion symmetry and thus no ferroelectricity would be seen. In such circumstances, it was postulated that the charge ordering state plus the commensurate magnetic order is responsible for the polarization where the Mn spins form an antiferromagnetic zigzag chain along the  $a$ -axis.

### ***1.4.3 Type-II multiferroics where the ferroelectricity induces a weak magnetic order***

Recently, there was theoretically proposed using a density-functional theory a new mechanism of creation of multiferroicity, where the magnetic order could be induced by a ferroelectricity.  $\text{FeTiO}_3$ ,  $\text{MnTiO}_3$ ,  $\text{NiTiO}_3$  and  $\text{BaNiF}_4$  were suggested as the best candidates for the search of such multiferroics.<sup>55</sup> We can consider them as new class of Type-II multiferroics. Two years ago, it was really experimentally proved that electric polarization induces weak ferromagnetism in  $\text{FeTiO}_3$ .<sup>56</sup> Moreover, it was predicted that the magnetization should be switchable  $180^\circ$ , but the experimental evidence for it is still missing. It should be also admitted that ferroelectrically induced by weak ferromagnetism was first time suggested by Scott in  $\text{BaMnF}_4$  already 33 years ago.<sup>57</sup>

## **1.5 Ferrotoroidic order**

A new ferroic order (ferrotoroidicity) was observed and described already many years ago.<sup>58</sup> Theoretical prediction was published already in 1957 when Ya. B. Zel'dovich<sup>59</sup> showed that some systems have a special distribution of magnetic fields like in toroidal windings. However, much later the “toroidal moment” term was coined in order to explain some properties of superconductors<sup>60</sup>. A magnetic toroidic moment  $\vec{T}$  is given by time-odd polar vector<sup>58,61</sup>

$$\vec{T} = \frac{1}{2} \sum_i \vec{r}_i \times \vec{S}_i \quad (1.6)$$

where  $\vec{r}_i$  and  $\vec{S}_i$  are the  $i^{\text{th}}$  positional vector and magnetic moment, respectively. The concept of  $\vec{T}$  is generally associated with a “circular” or “ring-like” arrangement of spins.

In fact, this toroidic moment is a vortex of magnetic moment e.g. atomic spins or orbital currents. So we can say that a system in which the toroidic moments are aligned spontaneously in cooperative way is named ferrotoroidic system. Recently there were observed ferrotoroidic domains in  $\text{LiCoPO}_4$ .<sup>62</sup> Some other typical examples of materials which possess ferrotoroidic properties are  $\text{GaFeO}_3$ ,<sup>63,64</sup> and  $\text{LiNiPO}_4$ .<sup>65</sup>

After introducing of ferrotoroidicity, we can summarize all ferroic orders in one diagram (Fig.1.4). It was considered that ferrotoroidic order is the fourth type of ferroics. We know

already that in ferroelectrics the order parameter change the sign upon the spatial reversal while in ferromagnets the order parameter change the sign upon time reversal. In ferroelastic systems no such change occur under two reversals. Thus the ferrotoroidic order which change sign simultaneously under spatial and time reversals can be considered as fundamental ferroic order.


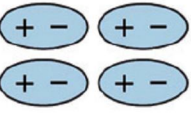
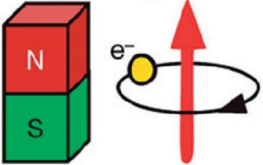
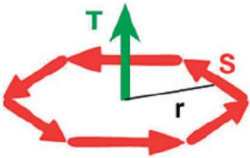
		Space	
		Invariant	Change
Time	Invariant	Ferroelastic 	Ferroelectric 
	Change	Ferromagnetic 	Ferrotoroidic 

Fig. 1.4. The diagram of four fundamental ferroic orders<sup>62</sup>

## 1.6 Some other types of multiferroics

### a) Multiferroic composites

Multiferroic composites incorporate piezoelectric and magnetic substances, where a huge ME coupling can emerge due to elastic coupling. The ME effect in composites materials is known as product tensor property:

$$ME_H = \frac{\text{magnetic}}{\text{mechanical}} \times \frac{\text{mechanical}}{\text{electric}}$$

$$ME_E = \frac{\text{electric}}{\text{mechanical}} \times \frac{\text{mechanical}}{\text{magnetic}}$$

These relations can be understood as follows: for  $ME_H$  effect, when a magnetic field is applied upon composites, the magnetic phase changes its shape magnetostrictively. The strain is passed to piezoelectric phase, resulting in electric polarization. For second relation,  $ME_E$  effect, the behavior is described in similar way, only the external field is electrical one and the result is a magnetization. Nevertheless, the ME effect in composites is extrinsic depending on the coupling



interaction across magnetic-piezoelectric interfaces. The most studied ME composites schemes are a combination of Terfenol D or ferrite ( $\text{CoFe}_2\text{O}_4$ ) with piezoelectrics ( $\text{BaTiO}_3$ , PZT,  $\text{PbMg}_{1/3}\text{Nb}_{2/3}\text{O}_3$ - $\text{PbTiO}_3$ ).<sup>66</sup>

***b) Multiferroic thin films***

In 2003 was shown that the multiferroic properties of  $\text{BiFeO}_3$  thin films are superior in comparison with  $\text{BiFeO}_3$  bulk ceramics and crystals.<sup>67</sup> From that reason many researchers focused their interest on deposition and characterization of various multiferroic thin films. During the last few years was really shown that the magnetization, polarization, Curie and Néel temperatures can be remarkably enhanced, antiferromagnetic order can be changed by strain to ferromagnetic one and even strong ferroelectric ferromagnets can be induced by strain in thin film systems, which are paraelectric and antiferromagnetic in the bulk form. Planar and columnar thin film heterostructures (see Fig.1.5) of magnetic and ferroelectric materials are also frequently investigated<sup>68</sup>

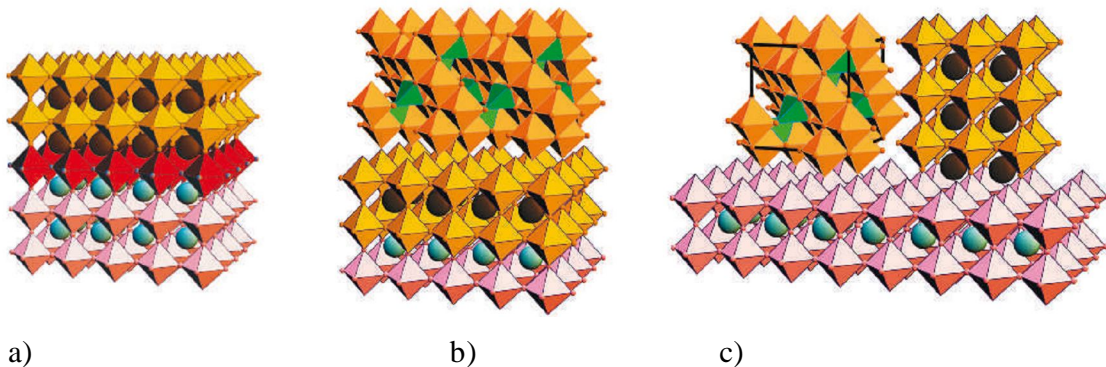


Fig. 1.5. Three types of model thin film architectures a) Single phase epitaxial films grown on single-crystal substrates b) horizontal heterostructures in which magnetic phase is epitaxially interleaved with a ferroelectric (piezoelectric) phase in order to create a magnetoelectrics c) the vertical analogue of b) in which nanopillars (or nanodots) of one phase are embedded epitaxially in a matrix of the other phase<sup>68</sup>

The first multiferroic investigated in thin film form was hexagonal  $\text{YMnO}_3$  obtained by radiofrequency magnetron sputtering.<sup>69</sup> However, it wasn't so much studied as  $\text{BiFeO}_3$  (mentioned above). Unlike  $\text{BiFeO}_3$ ,  $\text{BiMnO}_3$  thin film was proposed as a potential barrier material for magnetically and electrically controllable tunnel junctions.<sup>70</sup> This film exhibits ferroelectric phase demonstrated by writing of polarization bits using Kelvin force microscopy.<sup>71</sup>

Nevertheless, the high level of leakage has prevented a direct transport measurement of ferroelectric response. Other compounds as  $\text{BiCrO}_3$  and  $\text{PbVO}_3$  were reported in thin film form.<sup>72,73</sup>

Thin film growth techniques provide also the ability to vary the lattice mismatch between film and substrate (epitaxial strain). In conventional ferroelectrics, strain effects can lead to an increase of spontaneous polarization and Curie temperature and can even drive paraelectric materials such as  $\text{SrTiO}_3$  into ferroelectric phase.<sup>74</sup>

In epitaxial heterostructures we are able to engineer by atomic-level layering specific magnetic ordering through superexchange interactions and compositional ordering that breaks inversion symmetry to increase the polarizations. One example is ferromagnetic/ferroelectric heterostructure (e.g.  $\text{Fe}/\text{BaTiO}_3$ ) where a ME effect arises from a purely electronic mechanism, not mediated by strain.

For the case of vertical heterostructure, a prototypical multiferroic nanostructure consists of a magnetic spinel phase which is embedded into the ferroelectric matrix. In such conditions, several nanostructures were obtained:  $\text{CoFe}_2\text{O}_4$  pillars in a  $\text{BaTiO}_3$  matrix or  $\text{NiFe}_2\text{O}_4$  and  $\text{Fe}_3\text{O}_4$  in different combinations of perovskites ( $\text{BaTiO}_3$ ,  $\text{PbTiO}_3$ ,  $\text{BiFeO}_3$  and  $\text{SrTiO}_3$ ).<sup>75</sup>

## 1.7 Applications

Multiferroics may offers possibilities for new device functions. The dream of the researchers is to combine ferroelectricity and ferromagnetism for obtaining multiferroic memory or so called MERAM (ME random access memory),<sup>76,67</sup> where the magnetization would be written by electric field. A sketch of possible device and its functionality is shown and explained in Figure 1.6. Important point is that in MERAMs, the ME coupling gives the possibility to control the exchange coupling at interface between multiferroic and ferromagnetic layer by an applied voltage. The binary information is stored by the magnetization of bottom ferromagnetic layer (blue) which is read by monitoring the resistance of the magnetic trilayer and written by applied a voltage across the multiferroic ferroelectric/antiferromagnetic layer (green). If the magnetization of the bottom ferromagnetic layer is coupled to the ferroelectric/antiferromagnetic layer a reversal of the polarization  $P$  in the multiferroic layer stimulates the switching of the magnetic configuration in the trilayer from parallel alignment to antiparallel alignment. In such conditions, the lower state  $R_P$  go to higher state  $R_{AP}$ .

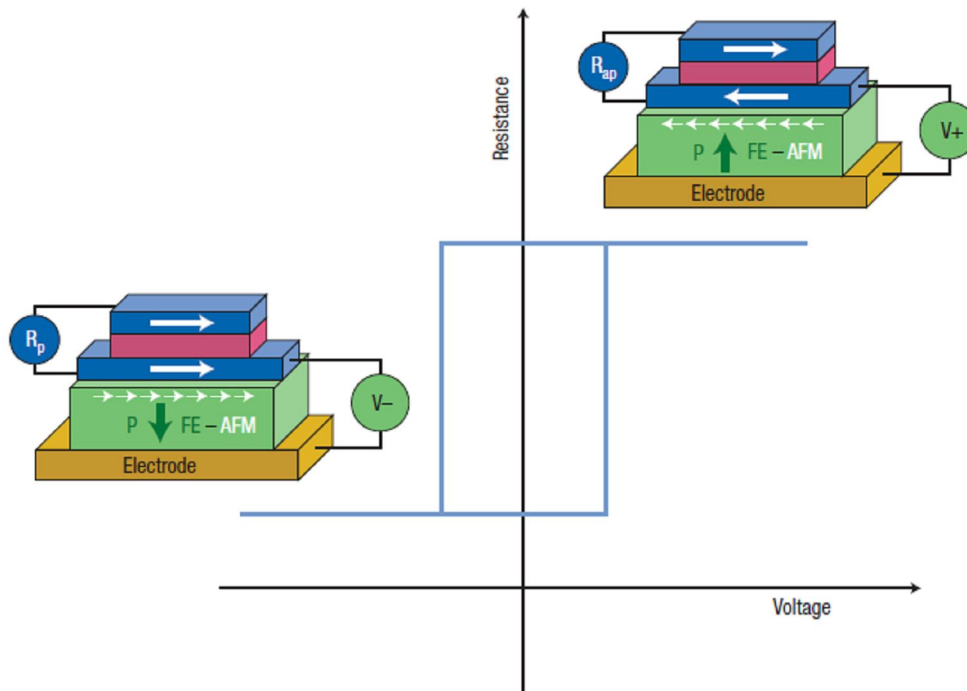


Fig. 1.6. The design of MERAM element. The information is encoded by the magnetization of the bottom ferromagnetic layer (blue), read by the resistance of the magnetic trilayer and written by applying a voltage across the multiferroic ferroelectric-antiferromagnetic layer (FE-AFM green). The existence of strong coupling between magnetization of bottom ferromagnetic layer and multiferroic spins will affect magnetic configuration of trilayer from parallel to antiparallel by reversing the electric polarization in multiferroic. This behavior can be done by applying a voltage [after reference 76].

However, there are other possible applications for multiferroics which make them very useful e.g the magnetic sensors, spintronics, microwave devices (e.g. tunable devices, resonators, and filters), transformers and gyrators<sup>77</sup>. These are usually proposed for multiferroic composites which allow large ME couplings. In the case of intrinsic multiferroics, the situation is not quite easy due to small magnetoelectric ME coupling above room temperature and low  $T_C$  and  $T_N$  values.

## CHAPTER 2 Theoretical backgrounds

### 2.1 Interaction of lattice dynamics with electromagnetic radiation

Lattice dynamic plays an important role in many areas of solid state physics. As a result of their thermal motion, the lattice ions vibrate about their equilibrium positions. All the thermal and elastic properties are related to it.

If we supply thermal energy to the lattice ion, it will rapidly be distributed throughout the entire lattice by the mutual interaction between the ions. Local excitation will therefore lead to collective vibrations of the whole ionic system. The lattice vibration can be readily quantized and the associated quantum is called *phonon*. It is a quasiparticle characterized by its frequency ( $\omega$ ) and wavevector ( $\vec{q}$ ).

Electromagnetic waves can interact with lattice vibrations in different ways: long wavelength vibrations caused by oscillating dipole moments (polar phonons) interact with the light in the infrared (IR) range leading to absorption and reflection bands. The acoustic hyper-sound waves and optical phonons that modulate the electronic polarizability of the crystal are also able to scatter the light.

The frequencies  $\omega_i$  of the lattice vibrations depend on the wavevector  $\vec{q}$ . The relations  $\omega = \omega_i(\vec{q})$  are called the *dispersion relations and they can be plotted in the Brillouin zone* (see Fig.2.1). When we have  $N$  primitive unit cells in the crystal, dispersion relation becomes a set of equations. Three branches of this equations called *acoustic branches* are translational and they approach zero frequency for  $q=0$ . The remaining  $3N-3$  branches are the *optical branches*. Vibrations in which the displacements of atoms are parallel to the wavevector  $\vec{q}$  are called longitudinal modes. When the displacements are perpendicular to  $\vec{q}$ , the modes are called *transversal*.

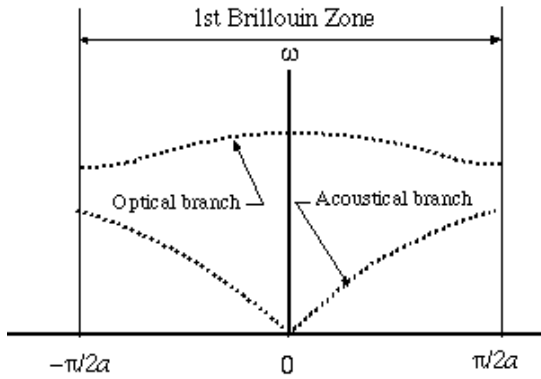


Fig.2.1. Dispersion relations  $\omega(q)$  for the linear atomic chain with a basis e.g. two atoms in the unit cell<sup>78</sup>

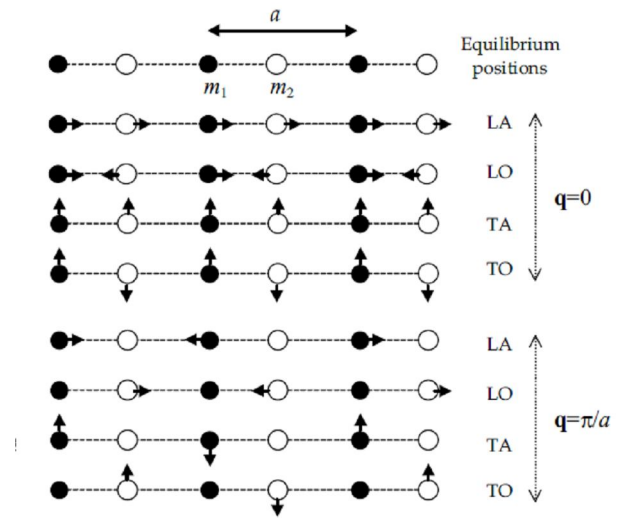


Fig.2.2. Atomic displacement patterns of a diatomic chain for transverse and longitudinal modes in  $q=0$  and  $q=\pi/a$ <sup>79</sup>

In polar crystals, a number of vibrational modes are polar, i.e they carry a dipole moment. Ionic vibrational modes, which involve oscillating electric dipoles, are termed optically active since these displacements can couple directly to electromagnetic radiation. This interaction produces a resonant absorption when the frequency of the radiation is equal to the frequency of the phonon with  $\vec{q} \rightarrow 0$ . This can be probed measuring the infrared (IR) reflectivity and absorption spectrum using an IR spectrometer. Thus by analyzing the IR absorption or reflectivity one can obtain detailed information concerning the frequency and damping of the IR active (i.e. polar) optic phonons. This technique will be described in other sub-chapter.

Other tool used for probing phonons is a Raman spectroscopy. The Raman spectra show the frequency shift of inelastically scattered light produced by phonon creation or annihilation.<sup>80</sup> The selection rules for the Raman spectra are in general different from those for the equivalent IR lines so that the two methods are considered complementary for the study of lattice vibrations. In order to analyze the Raman activity for the phonons, it is necessary to examine the transformation properties of all the lattice vibrations under the operations of the point group. In such circumstances, the irreducible representation of the point group according to which the relevant phonon transforms is contained in the representation formed by the components of the electronic susceptibility tensor.

However, the Raman spectra are often very complicated. Symmetry identification is usually obtained by examination of the polarization properties of incident and scattered radiation.

Difficulties can appear in separating the one-phonon from multiphonon components and therefore complementary measurements are necessary in IR or neutron scattering on the same material.

Absorption at phonon frequency has the shape of  $\delta$ -function in harmonic approximation and their frequency does not depend on temperature. But, the harmonic description is unable to account for thermophysical properties of solids. In reality, the vibrational modes are anharmonic. The simplest way to account for anharmonicity is to consider that the modes are damped. Within the description of classical theory, a constant damping statistically accounts for all anharmonic coupling processes that relax the phonon mode under consideration. If the description is often good in the immediate vicinity of the mode frequency, it is poor in the other region of the spectrum. Actually, damping  $\Gamma_j$  is a function of frequency and turns out to be the imaginary part of complex function called the phonon self-energy

$$P_j(\omega, T) = \Delta\omega_j(\omega, T) \pm i\Gamma_j(\omega, T) \quad (2.1)$$

Its real part  $\Delta\omega_j$  is called frequency shift function.<sup>81</sup>

### ***A. The Response of Transverse Optical (TO) phonons***

In cubic crystals the motion of one type of ions is all in the phase against the other type of ions. Their equilibrium position is associated with a microscopic instantaneous dipole moment,

$$\vec{p} = e_T \vec{x} \quad (2.2)$$

where  $x$  represents the displacement of the cations relative to the anion in normal coordinates. The transverse effective charge  $e_T$  is named in such way because only transverse modes can interact with an electromagnetic field.

In a cubic diatomic crystal the interaction of electromagnetic radiation with an undamped TO mode is described simply by an harmonic oscillator driven by the periodic field

$$\ddot{\vec{x}} + \omega_{TO}^2 \vec{x} = (e_T / \mu) \vec{E} \quad (2.3)$$

where  $\mu$  is the reduced mass of the ions and  $\omega_{TO} = (k / \mu)^{1/2}$  is the TO resonance frequency of the oscillator. The solution is a plane-wave function which is written in the form

$$(\vec{E}, \vec{P}, \vec{x}) = (\vec{E}_0, \vec{P}_0, x_0) e^{i(\omega t - \vec{k}\vec{r})} \quad (2.4)$$

Taking the derivatives, we obtain

$$(\omega_{TO}^2 - \omega^2) \vec{x} = (e_T / \mu) \vec{E} \quad (2.5)$$

Using the definition of the ionic susceptibility  $\vec{P} = \chi_i \varepsilon_v \vec{E}$ , where  $\varepsilon_v$  is the dielectric constant of vacuum, and equation (2.2) and (2.3) we obtain the ionic susceptibility in the form

$$\chi_i(\omega) = \left( \frac{e_T^2}{\mu \varepsilon_v V} \right) \left( \frac{1}{\omega_{TO}^2 - \omega^2} \right) \quad (2.6)$$

where  $V$  is the volume of the unit cell. The resonance term in the right side of Eq. (2.6) is characteristic of the response of TO mode to the IR electromagnetic field. The dielectric function is the response of all transverse excitations (not only ionic, but also electronic etc.) to the macroscopic field.

$$\varepsilon = 1 + \chi_{electronic} + \chi_{ionic} + \chi_{plasma} + \chi_{relaxation} + \dots \quad (2.7)$$

If we ignore plasmon and low-frequency relaxation effects in a first approximation, the dielectric function can be written

$$\varepsilon(\omega) = \varepsilon_\infty + \left( \frac{e_T^2}{\mu \varepsilon_v V} \right) \left( \frac{1}{\Omega_{TO}^2 - \omega^2} \right) \quad (2.8)$$

where  $\varepsilon_\infty = 1 + \chi_{el}$  is the “high frequency” dielectric constant.

If a phenomenological damping is introduced into the equation of motion (2.3), we can have

$$\ddot{\vec{x}} + \gamma_{TO} \dot{\vec{x}} + \omega_{TO}^2 \vec{x} = \frac{e_T}{\mu} \vec{E} \quad (2.9)$$

The oscillator strength is defined as

$$\Delta\varepsilon = \left( \frac{1}{\omega_{TO}^2} \right) \left( \frac{e_T^2}{\mu \varepsilon_v V} \right) \quad (2.10)$$

The Eq.2.8 gives for  $\omega=0$  static permittivity

$$\varepsilon(0) = \varepsilon_\infty + \Delta\varepsilon \quad (2.11)$$

and the classical complex dielectric function is obtained as<sup>81</sup>

$$\varepsilon(\omega) = \varepsilon_\infty + \Delta\varepsilon \frac{\omega_{TO}^2}{\omega_{TO}^2 - \omega^2 + i\gamma_{TO}\omega} \quad (2.12)$$

## B. Longitudinal Optical (LO) Phonons

In the case of longitudinal modes,  $\text{div}\vec{E} = 0$  and thus  $\varepsilon = 0$  is necessarily. In other words, the longitudinal modes are the zeros of the dielectric function. Therefore, the Eq. (2.12) yields

$$\varepsilon_\infty + \Delta\varepsilon \frac{\omega_{TO}^2}{\omega_{TO}^2 - \omega_{LO}^2} = 0 \quad (2.13)$$

The TO-LO splitting of polar vibrational mode is thus straightforwardly related to the dielectric strength  $\Delta\varepsilon$  the following relation

$$\frac{\omega_{LO}^2 - \omega_{TO}^2}{\omega_{TO}^2} = \frac{\Delta\varepsilon}{\varepsilon_\infty} \quad (2.14)$$

By combining Eqs (2.11) and (2.14) we obtain

$$\frac{\varepsilon(0)}{\varepsilon_\infty} = \frac{\omega_{LO}^2}{\omega_{TO}^2} \quad (2.15)$$

This is an important relation called Lyddane-Sachs-Teller (LST) relation derived first time by Lyddane et al.<sup>82</sup> in 1941. Making the sum over the all ionic susceptibilities of independent oscillator that vibrate along a given polarization, we have the general formula for classical dispersion model

$$\varepsilon = \varepsilon_\infty + \sum_j \Delta\varepsilon_j \frac{\omega_{jTO}^2}{\omega_{jTO}^2 - \omega^2 + i\gamma_{jTO}\omega} \quad (2.16)$$

One important feature of the longitudinal modes is the accumulation of charge in the nodal planes of the crystal lattice which results in the depolarizing field  $\vec{E}_{dep} = -4\pi\vec{P}$ . For TO mode, there is no accumulation of charge and the depolarizing field is zero. In this case the local field is parallel to the polarization and follows the lattice distortion (Fig 2.3). In normal incidence IR experiment, only the transverse phonons absorb the electromagnetic field i.e. just TO frequencies are directly seen at maxima of absorption  $\varepsilon''$ . Nevertheless, LO frequency can be determined from frequency of maxima of  $\text{Im}\left(\frac{1}{\varepsilon^*}\right)$ <sup>81</sup>



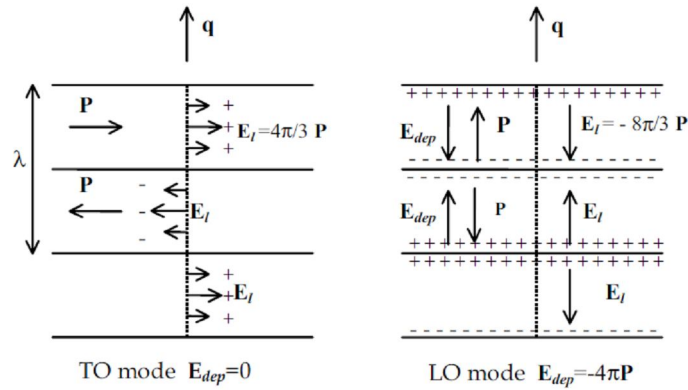


Fig.2.3. Polarization, local field and depolarizing field for TO and LO modes due to charge accumulation in nodal planes

## 2.2 Ferroelectricity

### 2.2.1 General properties of ferroelectric materials

A ferroelectric (FE) crystal is a solid which, below a critical temperature, exhibits a spontaneous polarization, i.e. it is polarized in the absence of an external electric field. Generally, the direction of spontaneous polarization may be switched under the influence of an applied field. The direction of spontaneous polarization does not need be the same throughout a macroscopic crystal. The crystal consists of a number of domains; within each domain the polarization has a specific direction, but this direction varies from one domain to another. The ferroelectricity is characterized by a hysteresis loop. The occurrence of hysteresis in the  $P$  versus  $E$  relationship can be explained if we consider for instance a crystal which initially has an overall polarization equal to zero i.e. the sum of the vectors representing the dipole moments of the individual domains vanishes. When an electric field is applied to the crystal, the domains with polarization components along the applied field direction grow at the expense of the “antiparallel” domains; thus the polarization increases (line OA in Fig. 2.4). When all domains are aligned in the direction of the applied field (BC), the polarization saturates and the crystal becomes single-domain. The extrapolation of the linear part BC to zero external field gives the spontaneous polarization  $P_s$ . The value of  $P_s$  is evidently the same as the polarizations which already existed within each of domains in the virgin state corresponding to the origin O (Fig.2.4). Spontaneous polarization means in fact the polarization within single domain. When the applied field goes from B to D point, the polarization of the crystal decreases. For zero applied fields there remains the remnant polarization  $P_r$ , where  $P_r$  refers to the crystal as whole. In order to remove the remnant



The static dielectric constant refers to the slope of the curve OA at origin, i.e.  $\varepsilon(0)$  is measured for small applied fields ( $E \rightarrow 0$ ) so that no motion of domain boundaries occurs. The static dielectric constant is defined

$$\varepsilon(0) = 1 + 4\pi \lim_{E \rightarrow 0} (P/E) \quad (2.17)$$

and it can be very large in the vicinity of the transition temperature (the order of  $10^4$  to  $10^5$ ). Above the transition temperature  $\varepsilon(0)$  obeys the Curie-Weiss law

$$\varepsilon(0) = \frac{C'}{T - T_0} + \varepsilon_\infty, \quad (2.18)$$

where  $C'$  is the Curie-Weiss constant, and  $T_0$  is defined as the temperature at which the extrapolated curve of the inverse dielectric constant cuts the temperature axis. For a first-order transition  $T_0 < T_c$ , but for a second-order phase transition  $T_0 = T_c$ .  $\varepsilon_\infty$  is the high-frequency dielectric constant contributed by the electronic and hard polar phonon's polarization.

### 2.2.2 Classification of ferroelectric crystals

We saw above that FE crystals exhibit polarized state below Curie point and above they are in unpolarized state. Thermal motion tends to destroy the ferroelectric order. Some FE crystals have no Curie points because they melt before leaving the ferroelectric phase. Other PE crystals tends to FE phase on cooling (their permittivity increases on lowering temperature), but they never reach FE phase due to quantum fluctuations at low T. These materials are called quantum paraelectrics or incipient ferroelectrics. FE crystals may be classified into two main groups with order disorder and displacive type of phase transition (PT).

One may define the character of the PT in terms of the dynamics of the lowest frequency (soft) optical phonon. If a soft phonon drives the transition, the transition is displacive. If the soft mode is not a phonon but some dielectric relaxation describing a large amplitude hopping motion of same cations among more equivalent minima of potential, the PT is of the order-disorder type. The order-disorder class of ferroelectrics includes crystals with hydrogen bonds in which the motion of the protons is related to the FE properties, as in potassium dihydrogen phosphate ( $\text{KH}_2\text{PO}_4$ ) and isomorphous salts. These phosphate groups are bounded together by hydrogen bonds.<sup>84</sup>

The most famous example of displacive ferroelectrics is  $\text{BaTiO}_3$  (Fig.2.5) but we can mention also  $\text{KNbO}_3$  and  $\text{PbTiO}_3$  or many others. In the case of  $\text{BaTiO}_3$ , the crystal is cubic in

paraelectric state with  $\text{Ba}^{2+}$  ions at the cube corners,  $\text{O}^{2-}$  ions at the centers of the cube faces and  $\text{Ti}^{4+}$  ions at the cube centers.

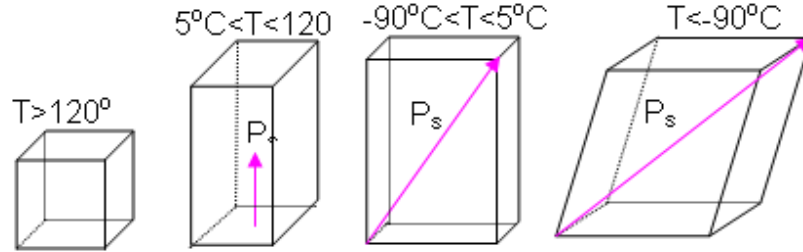


Fig.2.5. The perovskite structure of  $\text{BaTiO}_3$  in PE and FE phases (adapted after Ref. 85 )

Above  $T_C = 120^\circ\text{C}$ ,  $\text{BaTiO}_3$  ceramic has cubic structure. The titanium ions are all in equilibrium positions in the centre of the oxygen octahedra. When the temperature is lowered below the Curie temperature the crystal structure changes from cubic to tetragonal. The titanium ions displace off-center along the  $c$ -axis and induce a polarization in the same direction. As the temperature is lowered, the Ti cations displace gradually in the  $[110]$  and  $[111]$  crystallographic directions and the crystal structure changes gradually to orthorhombic and rhombohedral one.

### 2.2.3 The concept of soft modes and critical dynamics near ferroelectric phase transitions

By definition, soft phonon modes in crystals are low-frequency lattice vibrational modes whose frequencies tend to zero (soften) if the crystal approaches a structural PT. At a second order PT, the crystal structure loses its stability against the vibration given by the eigenvector of the soft mode. Such behavior holds for well-ordered and relatively weakly anharmonic crystal lattices and describes so called displacive PTs. It should be noted that the soft mode responsible for a FE PT induces a non-vanishing polarization  $\mathbf{P}$  due to the relative displacements of cations and anions. Below the transition point the displacement becomes static which produces a permanent polarization  $\mathbf{P}$ . The static displacement is limited by anharmonic forces and determines the new structure in the FE phase. The ions then vibrate around the new equilibrium positions below  $T_C$ .<sup>86</sup> The soft mode frequency  $\omega_{SM}$  versus temperature should obey the Cochran law

$$\omega_{SM}^2 = A(T - T_C) \quad (2.19)$$

where  $T_C$  is the critical Curie temperature and  $A$  is a constant. For proper FE transitions, where the order parameter is polarization, the soft mode is IR active in both PE and FE phases and we may readily assume that IR oscillator strength

$$f_{SM} = \Delta\varepsilon_{SM} \omega_{SM}^2 \quad (2.20)$$

of the soft mode is temperature independent across the PT. Cochran law then implies the Curie-Weiss law for static permittivity

$$\varepsilon(0) = \varepsilon_B + C/(T - T_C), \quad (2.21)$$

where the Curie-Weiss constant  $C = f_{SM} / A$  is determined by the temperature dependence of the soft mode frequency and  $\varepsilon_B$  is the sum of electronic contribution and contributions from other polar transverse optical (TO) modes to permittivity, which can be considered as temperature independent.

Frequently, the materials undergoing FE transitions are partially structurally disordered and/or strongly anharmonic and the simple optical soft mode picture does not hold. This is the case of order-disorder PTs. Here, the ions have two or more close sites in lattice of disordered phase. Their dynamical hopping among available sites gives rise to a dielectric relaxation below the polar phonon frequencies (typically in the microwave (MW) range), which slows down when the crystal approaches the PT. This is so-called critical slowing down and the relaxation frequency  $\omega_R$  (given by the frequency of maximum in the dielectric loss spectra) in the classical form obeys the dependence

$$\omega_R = A_R(T - T_C) \quad (2.22)$$

Dielectric relaxation in MW or radio-frequency region is usually described by Debye model. In some cases, when the relaxational mode lies near THz region, it can be fitted using an overdamped oscillator. In such case damping  $\gamma$  of the soft mode is twice larger than the oscillator eigenfrequency  $\omega_{SM}$ . The  $\omega_{SM}$  has no clear physical meaning, but we can estimate the relaxation frequency  $\omega_R$  from maximum in the dielectric loss spectra which corresponds to the frequency

$$\omega_R = \omega_{SM}^2 / \Gamma . \quad (2.23)$$

In many cases the dynamical anomalies around a FE PT are more complicated and contain features of both displacive as well as order-disorder mechanism e.g. optic soft mode plus relaxation mode. In such case far above  $T_C$  the optic soft mode reduces its frequency, i.e. it drives the PT. Several tens or hundreds of K above  $T_C$  the soft mode frequency saturates and appears a

new dielectric relaxation (central mode), which drives the phase transition near  $T_C$ . Such situation is usually referred to as crossover from displacive to order disorder PT and it occurs in the most FE systems.<sup>87</sup>

In perovskite structure (the most studied materials) zone-center modes and zone-corner (unit-cell doubling) modes are potentially unstable in the cubic phase. In this phase, the soft mode is Raman inactive. In fact, all optic modes are Raman inactive in cubic phase and neutron spectroscopy and infrared spectroscopy is better able to study the critical dynamics. Below transition point, there will always be a zone-center totally symmetric component of the soft mode Raman active, regardless of the symmetry or wavevector of the soft mode above the phase transition. In other words, the soft mode is always Raman active below  $T_C$ . Above  $T_C$  the soft mode can be seen in IR spectra of proper-ferroelectrics. If the PT is improper FE, the soft optic phonon comes from Brillouin zone boundary and cannot be seen in IR spectra of PE phase, but it becomes IR and Raman active below  $T_C$ . Its study in PE phase is possible only using inelastic neutron or X-ray scattering.<sup>80</sup>

## 2.3 Elementary excitations in magnetic material

### 2.3.1 General descriptions

The exchange interaction plays an important role for explaining the magnetic ordering in magnetic materials. Also, it is responsible for collective excitations of the ion spins system, known as spin waves. Thus, the associated quasiparticles are called *magnons*.

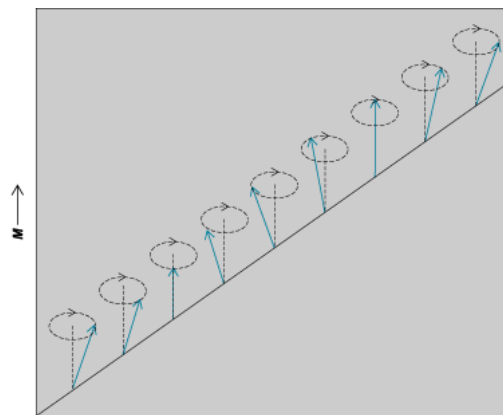


Fig.2.6. Spin wave in the linear ferromagnetic array (Internet sources<sup>88</sup>)

Collective excitations are low-lying excited states above a ground state. The ground state of the spin system is therefore important. If all spins are arranged in the same direction, the material is ferromagnet. In ferrimagnet and antiferromagnets, spins are aligned in different sublattices.

A ferromagnet is perfectly ordered at  $T=0$  K but at non-zero temperature the order is disrupted by spin waves. The crucial feature of these is that it costs a vanishingly small energy to produce a magnon, provided its wavelength is long enough. Thus the magnons play the same role in magnetically ordered materials as phonons in solids. As in the case of phonons, the energy of spins is quantized in units of  $\hbar\omega(\vec{q})$ , where  $\omega(\vec{q})$  is the frequency of the spin wave mode with wavevector  $\vec{q}$ . Whenever we have broken a continuous global symmetry, it is possible to produce long-wavelength excitations in the order parameter for vanishingly small energy cost. Such excitations are called Goldstone modes.<sup>89</sup>

### 2.3.2 Spin waves in ferromagnets: Magnons

In the classical description of excitations, the ground state has the net spin of the valence electrons zero. The reason for such behavior was that each of energy states in the one-electron approximation can be occupied by two electrons with opposite spins. The ground state therefore was regarded as that state in which all the energy levels were filled up to a limiting energy  $E_F$ , and all levels above that were empty. Such a state has neither net spin nor net momentum.<sup>89</sup>

In order to study this new type of excitation we will use a general approach. The spins are mostly localized on the lattice ions. Furthermore, several electrons contribute to the total ion spin. The ferromagnetic state is then the result of exchange interaction between the total spins of different ions.

The Hamiltonian operator in Heisenberg model is written as

$$\hat{H} = -\sum_{\langle i,j \rangle} J \hat{S}_i \hat{S}_j \quad (2.24)$$

The  $S_i$  are the vector spin operators of the  $i^{\text{th}}$  lattice ion and  $J$  is exchange integral. The sum is over all pairs of lattice ions. In one dimensional chain each spin has two neighbors, so the

Hamiltonian reduces to  $\hat{H} = -2J \sum_i \hat{S}_i \hat{S}_{i+1}$

We can calculate the time dependence of  $\langle \hat{S}_j \rangle$  using a formula as

$$\frac{d\langle \vec{S}_j \rangle}{dt} = \frac{1}{i\hbar} \langle [\hat{S}_j, \hat{H}] \rangle. \quad (2.25)$$

After developing the brackets and considering that the ground state of the system has all the spins aligned in the z direction, the equation above becomes

$$\begin{aligned} \frac{dS_j^x}{dt} &\approx \frac{2JS}{\hbar} (2S_j^y - S_{j-1}^y - S_{j+1}^y) \\ \frac{dS_j^y}{dt} &\approx -\frac{2JS}{\hbar} (2S_j^x - S_{j-1}^x - S_{j+1}^x) \\ \frac{dS_j^z}{dt} &\approx 0 \end{aligned} \quad (2.26)$$

The solutions look like

$$\begin{aligned} S_j^x &= Ae^{i(q_j a - \omega t)} \\ S_j^y &= Be^{i(q_j a - \omega t)} \end{aligned} \quad \text{where } \mathbf{q} \text{ is a wavevector.} \quad (2.27)$$

$$\text{After brief calculation, we will obtain } \hbar\omega = 4JS(1 - \cos qa) \quad (2.28)$$

which is **dispersion relation** for the spin wave. For  $\mathbf{q}$  very small, we can expand the cosine as

$$\cos(qa) = 1 - q^2 a^2 + q^4 a^4 + \dots \quad (2.29)$$

$$\text{Using the equation 2.27 and (2.28) we can have } \hbar\omega = 4JSa^2 q^2 \quad (2.30)$$

i.e. the magnon branch is quadratically dependent on wavevector  $\mathbf{q}$  in centre of Brillouin zone.

In three dimensions, the density of states is given by  $g(q)dq \propto q^2 dq$ , which leads to  $g(\omega)d\omega \propto \omega^{1/2} d\omega$  at low temperature where only small  $q$  and small  $\omega$  are important.

The number of magnon modes excited at temperature  $T$ ,  $n_{magnon}$ , is calculated by integrating the magnons density of states over all frequencies after multiplying by the Bose factor,

$$(\exp(\hbar\omega/k_B T) - 1)^{-1}. \text{ Thus the results is given by } n_{magnon} = \int_0^\infty \frac{g(\omega)d\omega}{\exp(\frac{\hbar\omega}{k_B T}) - 1},$$

$$\text{which can be evaluated using substitution } x = \frac{\hbar\omega}{k_B T} \quad (2.31)$$

At low temperature where  $g(\omega) \propto \omega^{1/2}$  in three dimensions, this yields the result

$$n_{magnon} = \left(\frac{k_B T}{\hbar}\right)^{3/2} \int_0^\infty \frac{x^{1/2} dx}{e^x - 1} \propto T^{3/2} \quad (2.32)$$



Since each magnon mode, which is thermally excited, reduces the total magnetization by  $S=1$ , then at low temperature the reduction in the spontaneous magnetization from the  $T=0$  value is given by

$$\frac{M(0) - M(T)}{M(0)} \propto T^{3/2} \quad (2.33)$$

This result is known as the Bloch  $T^{3/2}$  law and it fits experimental data in the low temperature regime. The energy of the magnon modes is given by

$$E = \int_0^\infty \frac{\hbar\omega g(\omega) d\omega}{\exp(\hbar\omega/k_B T) - 1} \propto T^{5/2} \quad (2.34)$$

So that thermal capacity  $C = \frac{\partial E_{magnon}}{\partial T}$  is also proportional to  $T^{3/2}$ .<sup>89</sup> (2.35)

For experimental determination of spin wave dispersions, a technique known as inelastic neutron scattering is used. Experiments are typically performed using a neutron triple-axis spectrometer, so called because the angles of the monochromator, sample and analyzer crystals can all be separately varied. Other technique, which can measure the ferromagnetic magnons, is FMR (ferromagnetic resonance). This method works typically in GHz range.

### 2.3.3 Antiferromagnetic and ferromagnetic resonances

The antiferromagnetic (AFM) behavior occurs in systems which consist of at least two interpenetrating sublattices, with anti-parallel arrangements. The different possible arrangements also depend on the kind of crystal lattice in which the spins are arranged. A selection of possible arrangements in simple cubic structure is shown in Fig.2.7.

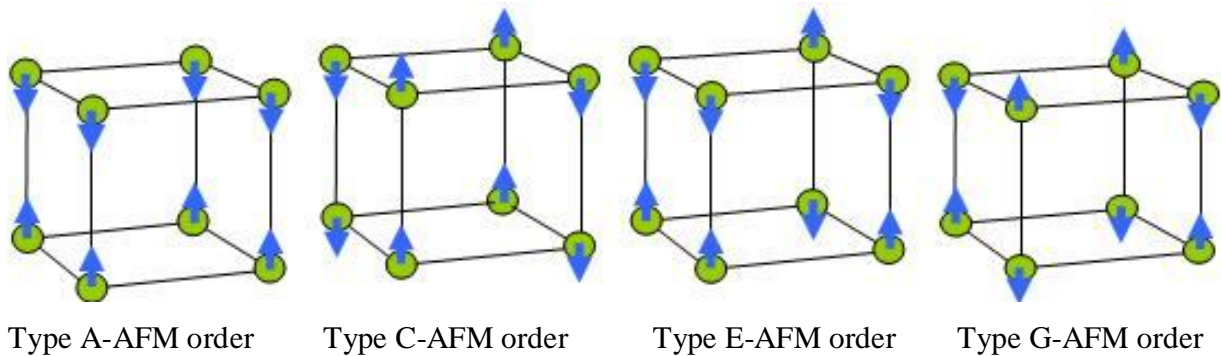


Fig. 2.7. Four types of antiferromagnetic order which can occur in simple cubic lattices<sup>89</sup>

In cubic perovskites, G-type AFM ordering is very common because superexchange interactions through oxygen atoms force all nearest-neighbor magnetic atoms to be antiferromagnetically aligned. However, there are some exceptions. For example,  $\text{LaFeO}_3$ ,  $\text{LaCrO}_3$  and  $\text{LaMnO}_3$  which are cubic perovskites, show A-type ordering.

In such circumstances the magnons branches can be different than in the case of ferromagnets and for ferrimagnets where the magnetic moments of the sublattice are unequal, the situation can be much complicated and difficult to solve it.

For Bravais lattices, the dispersion relation gives a  $q$ -dependence of the magnon energy which, similar to an acoustic branch of the phonon spectrum, starts with zero energy at  $q=0$  and increases up to the surface of the Brillouin zone. For lattice with a basis we must expect there to be other branches in the magnon spectrum, which do not start at 0 energy with  $q=0$  and therefore they remind the optical phonon branches. It will not be possible in such lattices to restrict the Heisenberg operators to exchange interactions between nearest neighbors. In most cases the ions in the individual sublattices will be different. The sublattices will then possess different total spins and often also different directions for the (individually parallel aligned) spin systems. The ground states will admittedly then show a magnetic moment. This will be the vector sum of the spins of the sublattices. For two sublattices with opposite spins, it will be therefore the differences in the spins. Such a ferrimagnet reveals differences compared with a ferromagnet.

In the Bravais lattice of a ferromagnet the spins are all aligned parallel in the ground state by exchange interaction. In such circumstances, the exchange integral is positive. The case of negative exchange integral, on the other hand, is then for nearest neighbors, which have the antiparallel spins. In the ground state, we find two sublattices of identical atoms but with opposite spin directions. This is the case of an antiferromagnet with mutually compensating spontaneous magnetic moments of two sublattices.

In the case of antiferromagnetic resonances, it will be used a similar approach as for ferromagnetic magnons. We will consider two sublattices in which the even indices  $2p$  compose sublattice  $A$  and the spins with odd indices  $2p+1$  compose sublattice  $B$ . Sublattice  $A$  has the spins up ( $S^z = S$ ) and sublattice  $B$  have the spins down ( $S^z = -S$ ). The equations written for  $A$ , if we consider the nearest neighbours, are the following

$$\begin{aligned}\frac{dS_{2p}^x}{dt} &= \frac{2JS}{\hbar}(-2S_{2p}^y - S_{2p-1}^y - S_{2p+1}^y) \\ \frac{dS_{2p}^y}{dt} &= -\frac{2JS}{\hbar}(-2S_{2p}^x - S_{2p-1}^x - S_{2p+1}^x)\end{aligned}\tag{2.36}$$

The corresponding equations for a spin on  $B$  sublattice are

$$\begin{aligned}\frac{dS_{2p+1}^x}{dt} &= \frac{2JS}{\hbar}(2S_{2p+1}^y + S_{2p}^y + S_{2p+2}^y) \\ \frac{dS_{2p+1}^y}{dt} &= -\frac{2JS}{\hbar}(2S_{2p+1}^x + S_{2p}^x + S_{2p+2}^x)\end{aligned}\tag{2.37}$$

We form  $S^+ = S^x + iS^y$ ; then

$$\begin{aligned}\frac{dS_{2p}^+}{dt} &= \frac{2iJS}{\hbar}(2S_{2p}^+ + S_{2p-1}^+ + S_{2p+1}^+) \\ \frac{dS_{2p+1}^+}{dt} &= -\frac{2iJS}{\hbar}(2S_{2p+1}^+ + S_{2p}^+ + S_{2p+2}^+)\end{aligned}\tag{2.38}$$

We look for solutions in the form

$$S_{2p}^+ = u \exp[i2pq - i\omega t] \text{ and } S_{2p+1}^+ = v \exp[i(2p+1)qa - \omega t]\tag{2.39}$$

The equations (2.37) become with  $\omega_{ex} \equiv -4JS/\hbar = 4|J|S/\hbar$

$$\begin{aligned}\omega u &= \frac{1}{2}\omega_{ex}(2u + ve^{-ika} + ve^{ika}) \\ -\omega v &= \frac{1}{2}\omega_{ex}(2v + ue^{-ika} + ue^{ika})\end{aligned}\tag{2.40}$$

Equations (2.39) have a solution if <sup>84</sup>

$$\begin{vmatrix} \omega_{ex} - \omega & \omega_{ex} \cos qa \\ \omega_{ex} \cos qa & \omega_{ex} + \omega \end{vmatrix} = 0\tag{2.41}$$

$$\text{Thus } \omega^2 = \omega_{ex}^2(1 - \cos^2 qa) \text{ and } \omega = \omega_{ex}|\sin qa|\tag{2.42}$$

The dispersion relation for magnons in an antiferromagnet is different from (2.27) for magnons in a ferromagnet. For  $qa \ll 1$ , the equation 2.42 become linear in  $q$ :  $\omega \approx \omega_{ex}|qa|$ .

The numbers of magnons branches in antiferromagnets and ferrimagnets could be decided by the magnetic space group. The magnetic unit cell may be larger than crystallographic one so the magnetic space group is only a subgroup of the space group of crystal symmetry. Many of the properties of the ordered state are determined by the spin wave-like excitations. Thus, the



## Chapter 3 Experimental techniques

### 3.1 Infrared spectroscopy

#### 3.1.1 Interferogram

Spectroscopy using Fourier Transform is a very fast method to measure IR spectra because it provides the way to measure the entire frequency range of spectrum during one scan. It is based on the classical Michelson interferometer method in which two coherent beams with different optical paths interfere.

In a Fourier interferometer each wavelength produces its own characteristic interference pattern when the difference of optical paths changes as the movable mirror is displaced. This creates a cosine variation in the intensity of the detector, whose magnitude depends on the wavelength. The interferogram is therefore the signal versus optical path difference. For a symmetric interferogram  $I(\delta) = I(-\delta)$  and the desired spectrum  $S(\omega)$  can be approximated by the Fourier series<sup>92</sup>

$$S(\omega) = 4 \sum_{\delta=0}^D [I(\delta) - \frac{1}{2}I(0)] (\cos 2\pi\omega\delta) \Delta\delta \quad (3.1)$$

Here,  $I(0)$  is the intensity at zero path difference,  $D$  is the maximum optical path difference and it equals twice the total moving mirror displacements.  $I(\delta)$  is sampled at discrete intervals  $\Delta\delta$  between  $\delta=0$  and  $\delta=D$ , therefore  $\delta = h\Delta\delta$  with  $h = 0,1,2\dots D/\Delta\delta$ . In order to obtain all the information in a spectral range  $0 < \omega < \omega_{\max}$ , it is necessary to sample points from the interferogram at intervals  $\Delta\omega = 1/D$ .

The detected interferogram is Fourier transformed by a dedicated computer. In the Fig.3.1. are showed several interferograms and their Fourier transforms.<sup>92</sup>

Several computational refinements have been developed to improve the quality of the spectra. One of them corrects the disturbing effects which arise by cutting off the interferogram at  $x_{\max} = D$  (apodization), another corrects the effects of unsymmetrical interferograms (phase-error correction). The phase-error correction can be avoided by measuring the interferogram for an equal distance on each side of  $x = 0$  and to compute the power transform of this double sided interferogram.

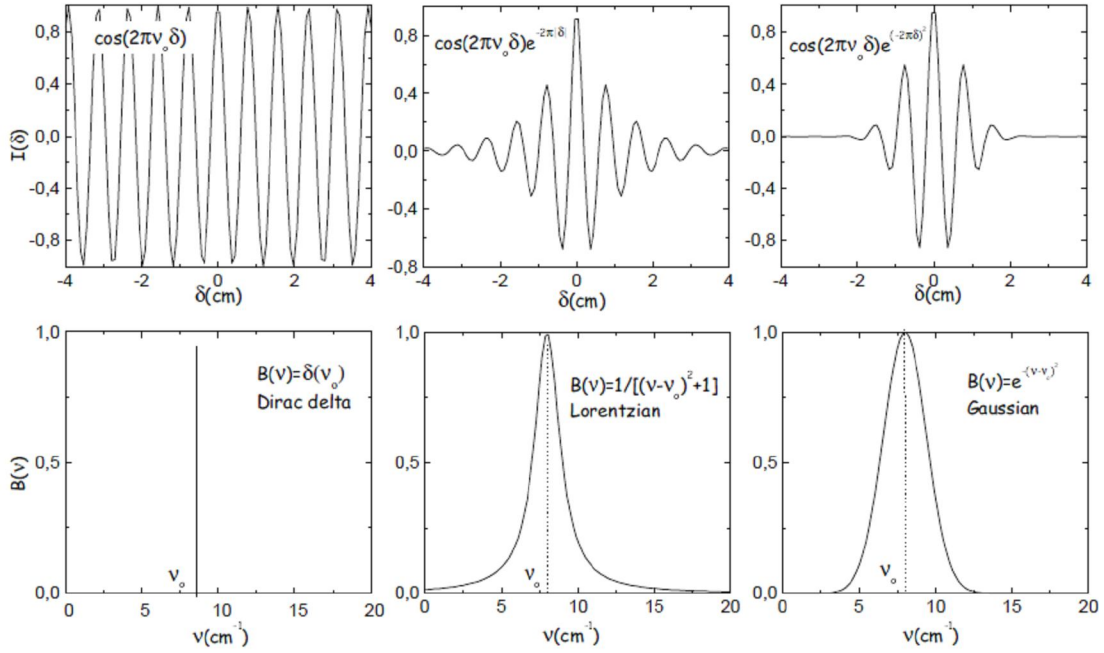


Fig.3.1. The spectra obtained by Fourier transform calculated for different interferograms (adapted after Ref[93])

If  $P(\omega) = GD(\omega)S(\omega)$  is the actual computed spectrum ( $G$ : amplifier gain,  $D(\omega)$ : detector sensitivity,  $S(\omega)$  is desired spectrum), then the transmission of the sample is given by  $T_S(\omega) = G_B P_S(\omega) / G_S P_B(\omega)$  where subscripts  $S$  and  $B$  refer to the sample and background spectra, respectively. An analogous relation holds for the reflectivity  $R_S(\omega)$ ; in this case a mirror is used at the place of the sample for the background spectrum.

### 3.1.2. Models for evaluation of complex dielectric function in IR region

From measurements of  $R$  and  $T$  it is possible to determine the optical constants. For an opaque sample  $T=0$  and  $A=1-R$ . For a black body  $A=1$ . For thick and highly reflecting metals  $R$  is close to unity,  $T$  is zero, and  $A$  is correspondingly small.

Let consider an optically isotropic materials (crystals of cubic symmetry). In the following we summarize some important relations for the optical constants. For the complex dielectric function we write

$$\varepsilon^*(\omega) = \varepsilon'(\omega) - i\varepsilon''(\omega) \quad (3.2)$$

where  $\varepsilon'$  and  $\varepsilon''$  are real and imaginary parts of complex permittivity. In crystals of lower symmetry  $\varepsilon$  has to be identified with one of the principles values of dielectric tensor  $\varepsilon_{ij}$ .

For the case of complex refractive index, we have  $n^*(\omega) = n(\omega) - ik(\omega)$ , (3.3)

where  $n$  is the refractive index and  $k$  the extinction coefficient.

We can relate permittivity in terms of  $n$  and  $k$  and therefore we have<sup>92</sup>

$$\varepsilon' = n^2 - k^2 \text{ and } \varepsilon'' = 2nk \quad (3.4)$$

The reflection from semi-infinite medium for normal and or near- normal incidence (incidence angle  $< 12^\circ$ ) is then

$$R(\omega) = \left| \frac{n^*(\omega) - 1}{n^*(\omega) + 1} \right|^2 = \left| \frac{\sqrt{\varepsilon^*(\omega)} - 1}{\sqrt{\varepsilon^*(\omega)} + 1} \right|^2 \quad (3.5)$$

In the formula above the complex index of refraction  $n^*(\omega) = \sqrt{\varepsilon^*(\omega)\mu^*(\omega)}$ . If it is considered a non- magnetic system the magnetic permeability is 1.i.e.  $\mu' = 1$  and  $\mu'' = 0$  and therefore  $n^*(\omega) = \sqrt{\varepsilon^*(\omega)}$ . The dielectric function  $\varepsilon^*(\omega)$  cannot be calculated exactly from the experimental data and therefore the reflectivity or transmission spectra has to be simulated by a model of the permittivity and Eq. (3.5). In the present, there are used three types of model for the dielectric function and fitting the experimental spectra with adjusting the parameters of the oscillators (eigen-frequencies, damping constants, dielectric strengths). They are discussed below.

#### a) 4-parameters generalized oscillator model

$$\varepsilon^*(\omega) = \varepsilon'(\omega) - i\varepsilon'' = \varepsilon_\infty \prod_{j=1}^n \frac{\omega_{LOj}^2 - \omega^2 + i\omega\gamma_{LOj}}{\omega_{TOj}^2 - \omega^2 + i\omega\gamma_{TOj}} \quad (3.6)$$

$$\Delta\varepsilon_j = \frac{\varepsilon_\infty}{\omega_{TOj}^2} \frac{\prod_{k \neq j} (\omega_{LOk}^2 - \omega_{TOk}^2)}{\prod_{k \neq j} (\omega_{TOk}^2 - \omega_{TOj}^2)} \quad (3.7)$$

where  $\omega_{TOj}$  and  $\omega_{LOj}$  are eigenfrequencies of the transverse and longitudinal  $j$ -th phonon mode, respectively and  $\gamma_{TOj}$  and  $\gamma_{LOj}$  their respective damping constants.  $\Delta\varepsilon_j$  is the contribution of each oscillator to the permittivity(see Fig.3.2).

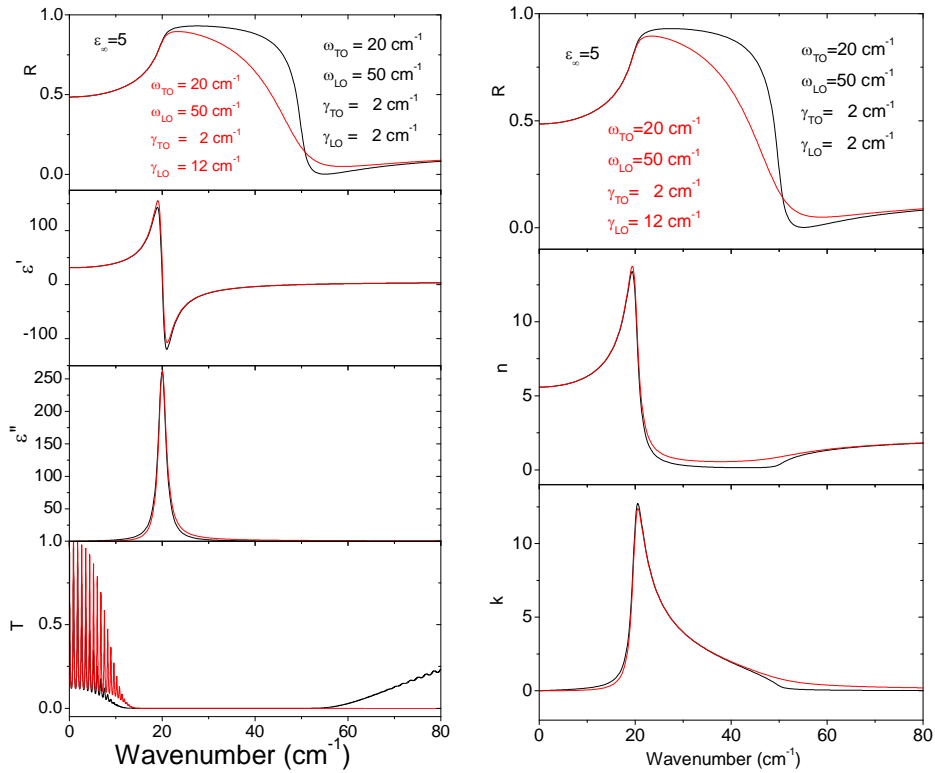


Fig.3.2. Model example of reflectivity and transmission spectra and corresponding real and imaginary parts of complex permittivity and index of refraction. in bulk - 4 parameter generalized oscillator model was used (thickness of the bulk = 1 mm).

The dielectric function is a factorization over its poles and zeros. These are complex because the eigenfrequencies are complex so their moduli  $\omega_{TOj}$ ,  $\omega_{LOj}$  are taken into account here. This model is generalization of the LST (Lyddane-Sachs-Teller) relation (Eq. 2.15). It is used when the spectra contain broad or asymmetrical bands arising from a wide TO-LO splitting. This model allows to attribute different damping constants to TO and LO modes, so that the fitting process needs four parameters for each oscillator. This model, however, has two disadvantages. One is the additional condition between the damping constants and frequencies which should be taken into account e.g.  $\gamma_{LO} > \gamma_{TO}$  and  $\gamma_{TO}/\gamma_{LO} > (\omega_{TO}/\omega_{LO})^2$  should be fulfilled in the case of one oscillator fit, otherwise non physical results with negative losses can be obtained. The second reason is that using a multiple oscillators a good criterion is to maintain the losses and optical conductivity always positive; otherwise the model is valid only in a limited range of frequencies.



**b) Classical damped oscillator model**

In the classical damped oscillator model the dielectric function is written as

$$\varepsilon^*(\omega) = \varepsilon_\infty + \sum_{j=1}^n \frac{\Delta\varepsilon_j \omega_j^2}{\omega_j^2 - \omega^2 + i\omega\gamma_j} \quad (3.8)$$

The model above can be equivalent with 4-parameter oscillator model if we consider  $\gamma_{TO} = \gamma_{LO}$  (see black curves from Fig.3.2)

The dielectric function is assumed to be a sum of  $n$  damped harmonic oscillators where  $\omega_j$  is the eigenfrequency of the  $j$ -th phonon mode,  $\gamma_j$  – its damping and  $\Delta\varepsilon_j$  its dielectric strength.  $\varepsilon_\infty$  is the value of the permittivity at frequencies much higher than all the phonon frequencies, but much lower than the electronic absorption edge. The model is appropriate when the splitting between TO and LO optical modes is weak (the IR reflection bands are narrow and symmetrical).

Both mentioned a) and b) models may fail in the transparent windows far below TO frequencies - where  $\varepsilon'$  dominates and the damping plays negligible role – because they are unable to predict accurately the frequency dependence of the weak absorption coefficient (which is dominated by  $\varepsilon''(\omega)$  and the imaginary phonon self energy) in these regions. This is the reason why transmission and reflection measurements are complementary.

**c) Mode coupling model**

For the case of two coupled modes (modes whose frequencies are near to each other enough to experience an exchange of energy) the situation can be phenomenologically described through the model of two bilinearly couples modes.<sup>94</sup> Let's give some useful formulae<sup>95</sup> for the simple case of two oscillators coupled through a real coupling constant  $\alpha$

$$\varepsilon^*(\omega) = \varepsilon_\infty + \frac{4\pi}{V} \frac{e_1(\omega_2^2 - \omega^2 + i\omega\Gamma_2) + e_2^2(\omega_1^2 - \omega^2 + i\omega\Gamma_1) - 2e_1e_2\alpha}{(\omega_1^2 - \omega^2 + i\omega\Gamma_1)(\omega_2^2 - \omega^2 + i\omega\Gamma_2) - \alpha^2} \quad (3.9)$$

where  $e_j, \omega_j$  and  $\Gamma_j$  are the effective charge, eigenfrequency and damping of the  $j^{\text{th}}$  uncoupled (bare) mode, respectively. A non-zero  $\alpha$  is introduced and it is assumed that  $\omega_1 > \omega_2$  which changes the bare eigenfrequencies to

$$\omega_\pm^2 = \frac{1}{2}(\omega_1^2 + \omega_2^2) \pm \sqrt{\frac{1}{4}(\omega_1^2 - \omega_2^2)^2 + \alpha^2} \quad (3.10)$$

effective charges to

$$\begin{aligned} e_+ &= e_1 \cos \varphi + e_2 \sin \varphi \\ e_- &= -e_1 \sin \varphi + e_2 \cos \varphi \end{aligned} \quad (3.11)$$

and dampings to

$$\begin{aligned} \Gamma_+ &= \Gamma_1 \cos^2 \varphi + \Gamma_2 \sin^2 \varphi \\ \Gamma_- &= \Gamma_1 \sin^2 \varphi + \Gamma_2 \cos^2 \varphi \\ \gamma &= (\Gamma_1 - \Gamma_2) \cos \varphi \sin \varphi \end{aligned} \quad (3.12)$$

Here  $\begin{pmatrix} \cos \varphi & \sin \varphi \\ -\sin \varphi & \cos \varphi \end{pmatrix}$  is the orthonormal transformation matrix from the old to new normal

coordinates which in the weak coupling limit  $|\alpha| \ll |\omega_1^2 - \omega_2^2|$  has the form

$$\cos \varphi \cong 1 - \frac{\alpha^2}{2(\omega_1^2 - \omega_2^2)^2}, \quad \sin \varphi \cong \frac{\alpha}{\omega_1^2 - \omega_2^2} \quad (3.13)$$

In the new coordinates the coupling becomes pure imaginary and is characterized by the mutual damping  $\gamma$ . The permittivity in new mode parameters is

$$\varepsilon(\omega) = \frac{4\pi}{V} \frac{e_+^2(\omega_-^2 - \omega^2 + i\omega\Gamma_-) + e_-^2(\omega_+^2 - \omega^2 + i\omega\Gamma_+) - 2i\omega e_+ e_- \gamma}{(\omega_+^2 - \omega^2 + i\omega\Gamma_+)(\omega_-^2 - \omega^2 + i\omega\Gamma_-) + \omega^2 \gamma^2} + \varepsilon_\infty \quad (3.14)$$

Using  $f = \Delta\varepsilon\omega^2 = 4\pi e^2$  (with reduced effective charge  $e^2 = e^{*2} / M_r V$ ), the complex permittivity becomes

$$\varepsilon^*(\omega) = \frac{\Delta\varepsilon_+ \omega_+^2 (\omega_-^2 - \omega^2 + i\omega\Gamma_-) + \Delta\varepsilon_- \omega_-^2 (\omega_+^2 - \omega^2 + i\omega\Gamma_+) - 2i\omega\gamma \sqrt{\Delta\varepsilon_+ \omega_+^2 \Delta\varepsilon_- \omega_-^2}}{(\omega_+^2 - \omega^2 + i\omega\Gamma_+)(\omega_-^2 - \omega^2 + i\omega\Gamma_-) + \omega^2 \gamma^2} + \varepsilon_\infty \quad (3.15)$$

#### d) Thin film model

In the case of thin films we can have two approaches. First approach is the coherent case where the optic waves, based on superposition of the amplitudes of the electromagnetic fields, include interference phenomena. In second approach, the incoherent case is considered where the geometrical optics, based on intensity summation, includes reflection or transmission loss but does not allow for interference.<sup>96</sup> First approach is used in the case of plane-parallel substrates, while the second one in the case of wedged samples, where the interferences do not occur.

In order to explain in details the model, we consider a beam at normal incidence on a system consisting of one with complex refractive indices  $n_1^*$  deposited on thick substrate having a

complex refractive index  $n_2^*$ . The system is surrounded from the top and the bottom by medium 0 (air or vacuum) which has a real refractive index of  $n_0$ . (Fig.3.3)

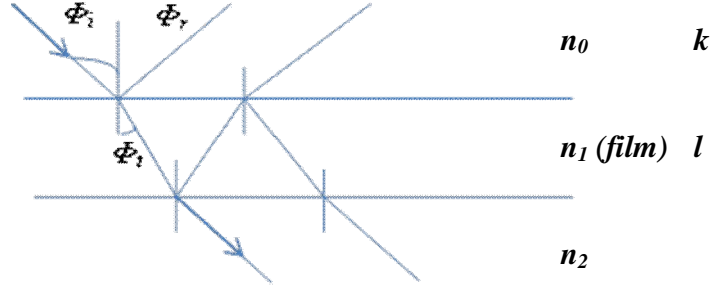


Fig.3.3. The multiple transmission and reflection by a thin film<sup>96</sup>

Using conditions for continuity of tangential components of electric and magnetic fields Fresnel's coefficients (amplitude reflection or transmission coefficients) can be obtained. They represent the ratios of the reflected ( $r$ ) and incident ( $i$ ) or of transmitted ( $t$ ) and incident electric field amplitudes at the interface between media  $k$  and  $l$ :

$$\tilde{r}_{kl} = r \exp(i\Phi_r) = \frac{E_r}{E_i} = \frac{Z_l - Z_k}{Z_l + Z_k} = \frac{n_k^* - n_l}{n_k^* + n_l} \quad (3.16)$$

$$\tilde{t}_{kl} = t \exp(i\Phi_t) = \frac{E_t}{E_i} = \frac{2Z_l}{Z_l + Z_k} = \frac{2\tilde{n}_k}{\tilde{n}_k + \tilde{n}_l} \quad (3.17)$$

where the complex surface impedance of the medium  $k$  is defined as  $Z_k = (4\pi/c) \times E_k / H_k$ . In the vacuum  $E_k = H_k$  and in the medium  $H_k = (n_k^* / \sqrt{\mu_k}) E_k$ , where  $\mu$  is the magnetic permeability.

In the coherent case, knowing these coefficients at the boundaries the total reflectance and transmittance of a layer can be calculated straightforwardly by adding up all partial waves. The overall power reflectance and transmittance of the film ( $f$ ) between the media 1 and 2 is given by

$$R_f = |\tilde{r}_f|^2, T_f = \text{Re}\left(\frac{n_2^*}{n_1}\right) |\tilde{t}_f|^2 \quad (3.18)$$

where  $\tilde{r}_f$  and  $\tilde{t}_f$  can be considered as composite Fresnel coefficients for the film, which in the case, when the film thickness  $d_f$  or inhomogeneity of the film is small compared to the coherence length of the radiation (thin film) are

$$\tilde{r}_f = \frac{\tilde{r}_{1f} + \tilde{r}_{f2} \exp(2i\tilde{\delta}_f)}{1 + \tilde{r}_{1f}\tilde{r}_{f2} \exp(2i\tilde{\delta}_f)} \text{ and } \tilde{t}_f = \frac{\tilde{t}_{1f}\tilde{t}_{f2} \exp(i\tilde{\delta}_f)}{1 + \tilde{r}_{1f}\tilde{r}_{f2} \exp(2i\tilde{\delta}_f)} \quad (3.19)$$

The complex phase shift  $\tilde{\delta}_f = 2\pi\tilde{n}_f d_f / \lambda_0$ , where  $\lambda_0$  is the wavelength of the radiation in vacuum, accounts for both real phase shift and the wave attenuation in the film due to absorption. These formulae include interference effects and depend upon coherence of the radiation over the optical path across the sample. A simple expression is available if the reflection-transmission process at the front and back surface of the sample is added incoherently. For a film with thickness  $d_f$  which is large compared to the coherence length of radiation (thick film) and with complex refractive index  $n_f^* = n_f + ik_f$ , where  $k_f \ll 1$ , the power reflectance and transmittance coefficients at the film-medium (k) interface are

$$R_{kf} = R_{fk} = \frac{(n_f - n_k)^2 + (k_f - k_k)^2}{(n_f + n_k)^2 + (k_f + k_k)^2} \quad (3.20)$$

$$T_{kf} = T_{fk} = \frac{4(n_f n_k + k_f k_k)}{(n_f + n_k)^2 + (k_f + k_k)^2}$$

The overall power reflectance and transmittance of the film including multiple reflection of the beam in the film are

$$R_f = R_{af} + \frac{T_{af}^2 R_{af} \exp(-2\alpha_f)}{R_{af}^2 \exp(-2\alpha_f)} \text{ and } T_f = \frac{T_{af}^2 R_{af} \exp(-\alpha_f)}{1 - R_{af}^2 \exp(-2\alpha_f)}, \text{ where } \alpha_f = \frac{4\pi k_f d_f}{\lambda_0} \quad (3.21)$$

where  $R_{af}$  and  $T_{af}$  are reflectance and transmittance coefficients at the film-air interface.

The reflectivity and transmission spectra can be well fitted by model of sum of harmonic oscillators (3.8) or by coupling model (3.15). Using these models we can obtain TO frequencies, damping and dielectric strength for the polar modes of the films.

### 3.1.3 Advantages and disadvantages of Fourier Transform spectroscopy

FT spectrometer has the following advantages:

- The interferometer receives the information from the whole spectral range during one fast scan with a movable mirror
- It allows a large circular source without limitation of the resolution, it can work with small aperture numbers (large solid angles at the aperture and detector)

- It has a very large resolution  $\Delta\omega$  given by possible large optical path difference  $D$ ,  

$$(\Delta\omega \sim \frac{1}{D})$$
- High wavenumber accuracy.
- It covers wide spectral range from FIR to visible region
- The scanning time is fast;
- It can be measured very weak signal (high signal/noise ratio)
- It allows the direct measurement of the complex reflection or transmission coefficient when the sample is placed in one of the arms of the interferometer.

Disadvantages:

- Not high photometric accuracy
- Inclusion of errors associated with the data processing in a computer (sampling and phase error in the interferogram)
- Loss of information about the phase, so need of using Kramers-Kronig relations or approximated models for the evaluation of the complex dielectric function.

**3.1.4 Experimental setup**

In our lab the IR spectra are measured using the Fourier spectrometer Bruker IFS 113v (Fig.3.4). It is working in near normal reflection mode, but also in transmission mode. The interferometer works in the range:  $10\text{-}5000\text{ cm}^{-1}$  (wavelength  $1\text{ mm} - 2\text{ }\mu\text{m}$ , frequency  $3\times 10^{11} - 1.5\times 10^{14}$  Hz). Two set of detectors are available: pyroelectric DTGS detector used for room and higher temperature measurements and a He-cooled (1.5K) Si bolometer which is more sensitive in the very FIR range. For low temperature measurements from 300 K down to 5 K, a continuous flow helium cryostat Oxford-type equipped with polyethylene windows is used for reflection and transmission mode, where the sample is placed in He gas bath. Measurements at high temperatures (300-900 K) are obtained with a commercial high temperature cell Specac P/N 5850. To polarize the light thin metal mesh polyethylene polarizers are used in the FIR and calomel  $\text{Hg}_2\text{I}_2$  in MIR region. Two types of sources are used for different spectral range: mercury lamp for FIR range and Globar source for MID region. As beam splitter we use different

(sometimes Si coated) Mylar films in the FIR region below  $600\text{ cm}^{-1}$ , or Ge/KBr for MIR. In the Fig. 3.4 it is shown the scheme of the FTIR spectrometer from our lab.

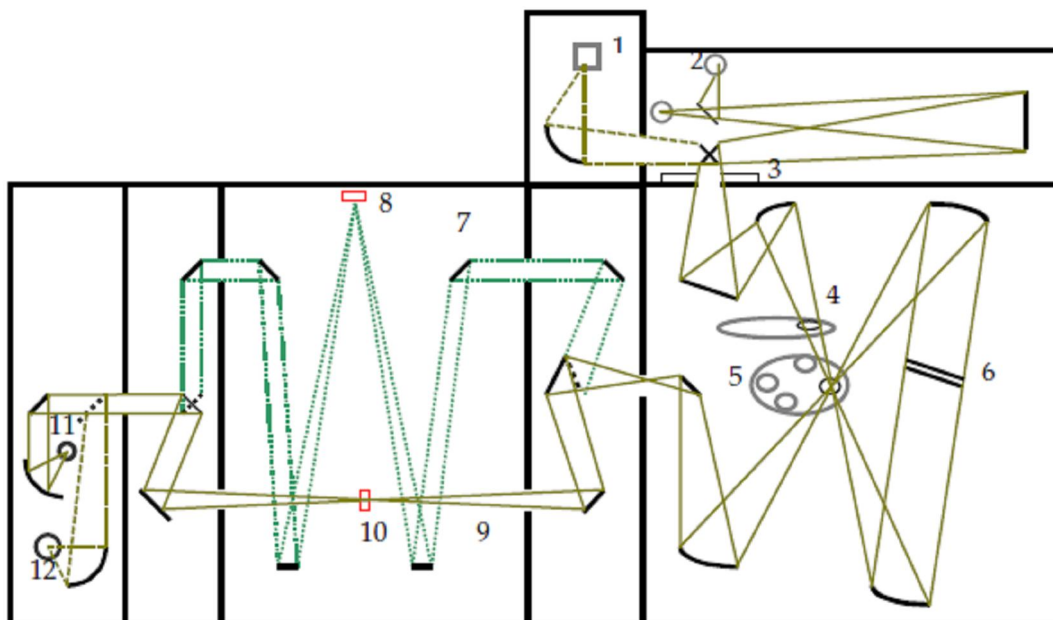


Fig.3.4. Scheme of IR spectrometer in our IR lab (Bruker IFS 113v). The numbers identify each component of the spectrometer 1) Globar source, 2) Hg source, 3) Aperture, 4) Optical filter wheel, 5) Beamsplitter wheel, 6) Scanning mirror, 7) Reflection path, 8) Sample position 1(in reflection mode), 9) Transmission path, 10) Sample position 2 (in transmission mode) , 11) DTGS detector, 12) Bolometer

## 3.2 Time domain terahertz spectroscopy

### 3.2.1 Terahertz radiation

In the past (until 1980s) the electromagnetic spectrum was divided into two broad areas. The frequencies belonging to the radio and microwave (MW) regions ( $\leq 100\text{GHz}$ ) were accessed directly with electronics while the frequencies of IR radiation and above ( $\geq 2\text{ THz}$ ) were handled by photonics by the production of photons through quantum transitions.<sup>97</sup> The frequency range between the MW and IR were hardly accessible. In this region, the electron mobility, crucial for MW techniques, is rapidly decreasing towards higher frequencies. Other cause was the lack of semiconductor materials with a wide enough band gap. Electromagnetic frequency range between the MW and IR waves which spans over frequencies from 0.1 to 10 THz (according to a commonly accepted definition) is named the THz gap, THz radiation, THz waves, submillimeter radiation, millimeter band, T-rays or simple THz.

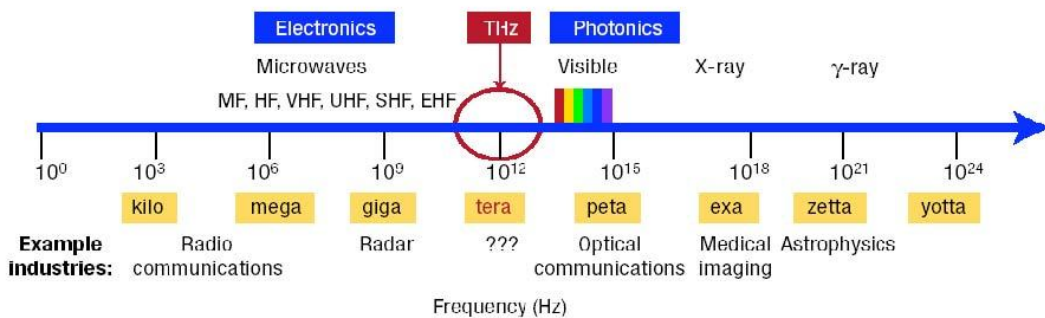


Fig.3.5. THz frequency lies between the infrared and microwave region in the electromagnetic spectrum<sup>97</sup>

The value of 1 THz frequency can be expressed by various units as follows:

$$1\text{THz} \sim 1\text{ps} \sim 300\mu\text{m} \sim 33\text{cm}^{-1} \sim 4.14\text{meV} \sim 48\text{K} \quad (3.22)$$

and they are in order written as follows: frequency, period, wavelength, wavenumber, energy and Boltzmann equivalent temperature.

Although the first record of observation of THz radiation is dated late 1800s<sup>98</sup>, due to technical troubles this range has stayed outside the main interest of researchers for long time.<sup>99</sup>

### 3.2.2 Sources of THz radiation

A source in time domain terahertz spectroscopy uses a dipole. A dipole here means an elementary doublet of a small length of conductor  $d_c \ll \lambda$  carrying an alternating current:

$$l = l_0 \exp(-i\omega t), \quad (3.23)$$

where  $\omega = 2\pi \nu$  is the angular frequency and  $l$  is a phasor.

The emission of the dipole was described by Born and Wolf<sup>100</sup>. They point out the dependence of the field emitted by the dipole vs the distance  $r$  and form its center as varying in the inverse power of  $r$ ,  $r^2$ ,  $r^3$ . The term  $r^{-1}$  is associated with a propagating field obeying the energy conservation law. Sources have their own limitations and could reach out more or less into THz gap from both sides of spectrum.

Sources can be distinguished based on their technical specifications by:

- Frequency range and frequency bandwidth: monochromatic (narrowband and with a single-frequency emission, continuous wave) and broadband, i.e. pulsed radiation;
- Tunability: none, discrete or continuous;
- Power of the emission: ranges from the weakest source of black body background around 300K to GW-peak-energy radiation from free-electron lasers (FELs)<sup>101</sup>
- Operability: turn-key systems, table-top, extra (a need of cryogenic cooling) and large facilities (running under international operations)<sup>102</sup>

As detectors, we can briefly enumerate several detectors used for THz range: detectors in broad band pulses<sup>103</sup>, detectors based on electro-optical (Pockels) effect<sup>104</sup>, photoconductive detectors<sup>105</sup>, etc.

### 3.2.3 Time domain terahertz spectroscopy

The first groups which developed the time domain terahertz spectroscopy (TDS) were Auston and Nuss<sup>104</sup> and that of Fittinger and Grischkowsky<sup>106</sup>.

The spectroscopic method consists in the measurement of a reference waveform  $E_r(T)$  with an empty diaphragm and signal waveform  $E_s(T)$  with the sample placed on the diaphragm. The complex transmission is calculated according to Ref [107]:



$$t(\omega) = \frac{E_s(\omega)}{E_r(\omega)} = \frac{4n^* \exp[i\omega(n^* - 1)\frac{d}{c}]}{(n^* + 1)^2} \sum_{k=0}^m \left[ \left( \frac{n^* - 1}{n^* + 1} \right) \exp(i\omega n^* \frac{d}{c}) \right]^{2k} \quad (3.24)$$

where  $n^*$  is the complex index of refraction of the sample,  $\omega$  is frequency,  $d$  sample thickness,  $c$  light velocity, and  $m$  is the number of reflections in the sample. This equation can be solved only numerically determining the amplitude and the phase of the transmissivity. The TDTS usually allows avoiding the problem of the periodicity of the phase. It can be determined the order of the phase for the spectral components near the central frequency by measuring time delay between the signal and the reference pulses. The limiting factors of this method are the requirement of the perfectly plane parallel samples and a precise determination of their thickness.

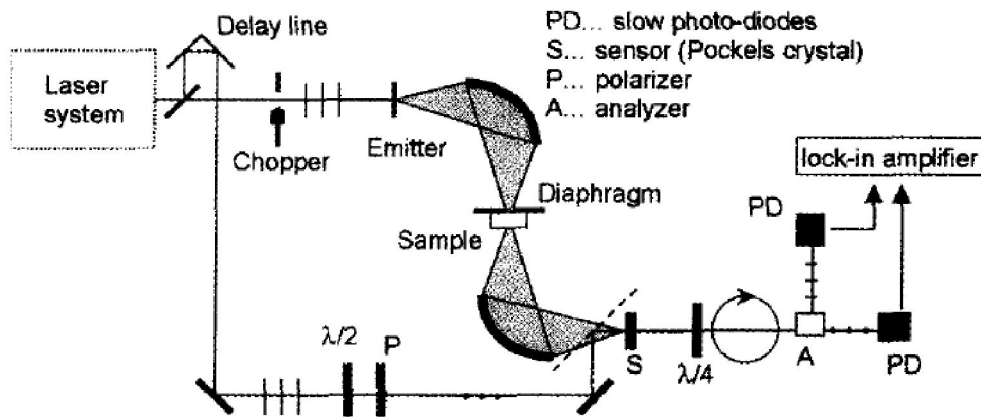


Fig.3.6. The scheme of time domain terahertz spectrometer<sup>107</sup>

The setup in our Institute uses a Ti:sapphire laser oscillator ( $\tau = 80 fs$ ,  $\lambda = 800 nm$ ) as the light source. Horizontally polarized THz radiation is generated in a biased large-aperture photoconducting antennas made of low-temperature GaAs or semi-insulating GaAs:Cr.

The electro-optic sampling technique uses a 1 mm thick ZnTe sensor crystal for the detection of the pulses. The spectral resolution depends on the length of the time runs. A typical resolution is  $0.5 cm^{-1}$ . The wavenumber range covered the range of  $3-80 cm^{-1}$  in the case of well transparent samples.

## **3.3 Techniques for magnetic measurements**

### ***3.3.1 Introduction in magnetic measurements***

The most obvious experimental approach for probing the magnetism in samples is the measurement of magnetization. This is essentially a measurement of magnetic moment which is divided by sample volume or mass which gives the magnetization. There are a lot of varieties of measurement techniques for characterization of magnetic samples. e.g. magnetic resonance methods, magnetometry, neutron scattering, local probe techniques, etc. However, the experimental techniques which measure the magnetic moment and susceptibility are much often used. I will describe further SQUID (Superconducting Quantum Interference Device) and PPMS (Physical Property Measurement System) with ACMS (AC measurement system) technique which we used in our study.

### ***3.3.2 SQUID***

MPMS XL7T (Magnetic Property Measurement System) setup from Quantum Design is specified for experimental and material characterization tasks in broad temperature range and in applied field up to 7 T. It is configured to detect magnetic moment of a sample of material, from which the magnetization and magnetic susceptibility can be determined.

The MPMS system includes several different superconducting components:

1. superconducting magnet to generate large magnetic field
2. superconducting detection coil which couples inductively to the sample;
3. SQUID connected to the detection coil
4. superconducting magnetic shield surrounding the SQUID

The most important part of this system is so called SQUID device (Fig.3.7). It consists of a closed superconducting loop including one or two Josephson junctions in the loop's current path. In the scheme below it is represented a simplified scheme of core element composed by two small Josephson junction inserted in a superconducting loop.

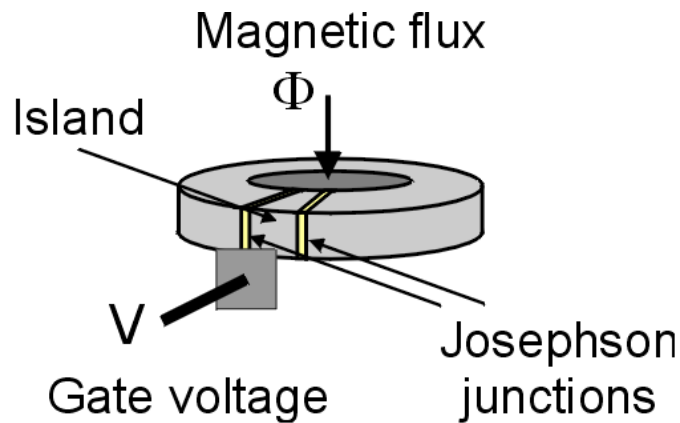


Fig.3.7 A scheme of SQUID with two Josephson junctions <sup>108</sup>

However, the SQUID does not detect directly magnetic field from the sample in MPMS instrument. The sample is passing through a system of superconducting detection coils, which are connected to the SQUID with superconducting wires. The current from detection coils is inductively coupled to the SQUID sensor. The SQUID electronics produces an output voltage which is strictly proportional to the current flowing in the SQUID input coil.

As the sample moves through the detection coils, the magnetic moment of the sample induces an electric current in the detection coils. Any change of magnetic flux in the detection coils produces a change in the current in the detection circuit because it is proportional to the change of magnetic flux. This is happening because the detection coils, the connecting wires and the SQUID input coils form a closed superconducting loop.

Since the SQUID functions as a linear current- voltage convertor the variations of the current in the detection coils produce a variation in the SQUID output voltage which is proportional to the magnetic moment. <sup>109</sup>

### 3.3.3 Measurements of AC susceptibility in PPMS

AC/DC Magnetometry System (ACMS) performs AC susceptibility as well as DC magnetization. AC susceptibility does not directly measure a sample's magnetic moment. Samples with very different magnetic moments can have the same response to a changing magnetic field if their susceptibilities are the same in the measurement regimes of interest. The AC susceptibility can be measured with ACMS technique. This option in the ACMS adds a small alternating field to the large applied field from the PPMS superconducting magnet and measures a sample's magnetic

moment response. Both the amplitude and phase of this response are reported. Alternatively, the ACMS can report the in-phase and quadrature components of the sample's response. To obtain the AC susceptibility, we must divide the amplitude of the change in moment  $dM$  by the amplitude of the alternating field  $dH$ . This gives  $\chi_{ac} = \frac{dM}{dH}$

This is only the local slope of the sample's magnetization curve  $M(H)$  and not the real susceptibility which is given by  $\chi = \frac{M}{H}$ . This difference appears when we are dealing with samples that have nonlinear magnetization curves.

During an AC measurement, an alternating magnetic field is applied to the measurement region by itself or in addition to the constant field applied by the PPMS superconducting magnet. The alternating magnetic field is produced by primary set of coils while the secondary two set of coils are connected together in the compensating arrangement.

DC magnetization measurements measure a sample's magnetic moment  $M$  in an applied magnetic field  $H$  at a specific temperature  $T$  ( $M=M(H,T)$ ). The ACMS does not use Quantum Design SQUID technology to perform DC magnetization measurements. It moves the sample through a set of copper coil and analyzes the induced signal with a digital processor (DSP) to determine the sample's magnetization.

During a DC magnetization measurement, the PPMS apply a constant magnetic field to the sample space, and finally a signal comes through the entire detection coil set in approximately 0.05 second. The detection coils register a voltage proportional to the rate of change of magnetic flux through the coils, so the voltage profile is the time derivative of the net flux through the coils. The actual sample moment is obtained by numerically integrating the voltage profile and fitting the known waveform for a dipole moving through the detection coils to the resulting data using regression algorithm.

The basic temperature range for measuring susceptibility in common ACMS system are from 2 K up to 400 K. However, we have measured also down to 0.5 K using He-3 and special home-made adaptation of ACMS system.<sup>110</sup>

## Chapter 4 Our experimental results

### 4.1 List of investigated materials and their preparation

Materials selected for this study are bulk ceramics and single crystal but also thin films. They belong to different groups of classification presented already in Chapter 1. In the table below they are classified in two different categories.

Type-I Multiferroics	A) Multiferroic perovskites: $\text{EuTiO}_3$ , $\text{Eu}_{0.5}\text{Ba}_{0.5}\text{TiO}_3$ , $\text{Eu}_{0.5}\text{Ba}_{0.25}\text{Sr}_{0.25}\text{TiO}_3$ , $\text{SrMnO}_3$ , $\text{Sr}_2\text{TiMnO}_6$
	B) Compounds with ferroelectricity induced by lone pair: $\text{Bi}_{0.85}\text{Nd}_{0.15}\text{FeO}_3$
	C) Compounds with “geometric” ferroelectricity: $\text{YMnO}_3$ , $\text{Y}_{1-x}\text{Eu}_x\text{MnO}_3$ , $x=0.1$ and $0.2$ , $\text{InMnO}_3$
Type-II Multiferroics	Multiferroics with spiral magnetic ordering: $\text{Ba}_{0.5}\text{Sr}_{1.5}\text{Zn}_2\text{Fe}_{12}\text{O}_{22}$ with Y-type hexaferrite structure

$\text{EuTiO}_3$  (ETO) ceramics were prepared in our lab at the Institute of Physics in Prague and Brno University of Technology, Czech Republic.<sup>111</sup> Another set of samples was provided from National Institute of Materials Science, Japan. Our first bulk ETO ceramics were synthesized from  $\text{Eu}_2\text{O}_3$  and  $\text{Ti}_2\text{O}_3$  powder using mechanochemical activation in the planetary micromill Fritsch Pulverisette 7. The powders were pressed into pellet in a uniaxial press at 650 MPa at room temperature and then annealed at 1500°C in  $\text{Ar}+10\%\text{H}_2$  atmosphere. The reducing atmosphere was necessary to prevent the formation of pyrochlore  $\text{Eu}_2^{3+}\text{Ti}_2^{4+}\text{O}_7$  phase. ETO single crystal was provided by Prof. Weidenkaff from Swiss National Lab for Material Research, Dübendorf, Switzerland.

$\text{SrMnO}_3$  (SMO) and  $\text{InMnO}_3$  (IMO) ceramics were provided by A. Belik from National Institute of Materials Science, Japan. IMO was obtained by a stoichiometric mixture of  $\text{In}_2\text{O}_3$  (99.9%) and  $\text{Mn}_2\text{O}_3$  placed in Au capsules. The mixture was treated at 6 GPa in a belt-type high-pressure apparatus at 1373 K for 30 min. For details see Ref.<sup>112</sup>. SMO was prepared in similar way as in Ref.<sup>113</sup>.

$\text{Sr}_2\text{TiMnO}_6$  (STMO) polycrystalline powder samples were prepared by P. Meher using conventional solid state synthesis route. The preheated powder were pressed into pellets and

sintered at 1573 and 1623 K for 24 h in the ambient atmosphere to obtain maximum density. The details of preparation can be found in Ref. <sup>114</sup>

$\text{Bi}_{0.85}\text{Nd}_{0.15}\text{FeO}_3$  (BNFO) ceramics were provided by Prof. Reaney from Department of Engineering Materials, University of Sheffield, United Kingdom. The doped composition powder was reacted at 870 °C for 3 h in lidded alumina crucibles and then milled and dried. Pellets were prepared by pressing in a 10 mm die at ~250 MPa and sintering for 3 h at 920 °C. Details of powder preparation can be found in Ref. <sup>115, 116</sup> The IR reflectivities were taken from pellets polished on one-side (thickness ~ 1 mm) whereas THz transmission spectra were obtained from both sides polished plates with thickness ~ 100  $\mu\text{m}$ .

Hexagonal  $\text{YMnO}_3$  (YMO) was studied in the form of ceramics and single crystals. Additionally, we investigated  $\text{Y}_{1-x}\text{Eu}_x\text{MnO}_3$  ceramics with  $x=0.1$  and  $0.2$ . The ceramic samples were prepared by P. Tavares from Vila Real (Portugal) using the sol-gel urea combustion method.<sup>117</sup> The hexagonal YMO single crystal was provided by R. Pisarev from Ioffe Technical Institute, St. Petersburg, Russia. The crystals were grown by the floating zone method. Two crystal plates with the  $c$  axis oriented either in-plane or out of plane along its normal were cut and polished to obtain plane parallel sample with thicknesses 1100 and 348  $\mu\text{m}$  for each orientation.<sup>118</sup>

$\text{Ba}_{0.5}\text{Sr}_{1.5}\text{Zn}_2\text{Fe}_{12}\text{O}_{22}$  (BSZFO) with Y-type hexaferrite structure was also investigated in the form of ceramics and single crystals. The single crystals were provided by Prof. T. Kimura from Osaka University, Japan. The methods of preparation of single crystal are described in details elsewhere.<sup>119</sup> Ceramics were prepared by J. Buršík from Institute of Inorganic chemistry, Řež using the Pecchini process. Final crystallization of BSZFO phase has been done by annealing at 1100 °C for 24 h in air atmosphere. For preparation of ceramics, single phase powder was pressed by means of cold isostatic pressing at 300 MPa and then sintered at 1100 °C for 72 h in the air.<sup>120</sup>

Most of investigated ETO thin films were prepared by reactive molecular beam epitaxy (MBE) in the group of Prof. D. Schlom at Cornell University, USA. Oriented single crystals of  $\text{DyScO}_3$  (DSO),  $(\text{LaAlO}_3)_{0.29}-(\text{SrAl}_{1/2}\text{Ta}_{1/2}\text{O}_3)_{0.71}$  (abbreviated as. LSAT) and  $\text{LaAlO}_3$  were used as the substrates. These samples are marked as ETO/DSO, ETO/LSAT and  $\text{EuTiO}_3/\text{LaAlO}_3$  (ETO/LAO). ETO films deposited on NGO were obtained by pulsed laser deposition (PLD) also at Cornell University, USA.

## 4.2 EuTiO<sub>3</sub>

EuTiO<sub>3</sub> (ETO) crystallizes in a cubic perovskite structure with a space group  $Pm\bar{3}m$  similarly as SrTiO<sub>3</sub> (STO) and paraelectric (PE) BaTiO<sub>3</sub>. A distinct feature of ETO from other tetravalent perovskites titanates is the existence of localized  $4f$  moments with  $S=7/2$  on the  $\text{Eu}^{2+}$  sites, which order antiferromagnetically below 5.3 K. The crystal and magnetic structure of ETO is depicted in Fig. 4.1a). The spins are indicated by arrows and they exhibit a G-type antiferromagnetic (AFM) order<sup>121,122</sup> Recently, there was observed a strong AFM resonance near 34 GHz in ETO ceramics.<sup>123</sup> The AFM resonance exhibits unusually huge Faraday rotation (560°!) at 1.6 T magnetic fields.

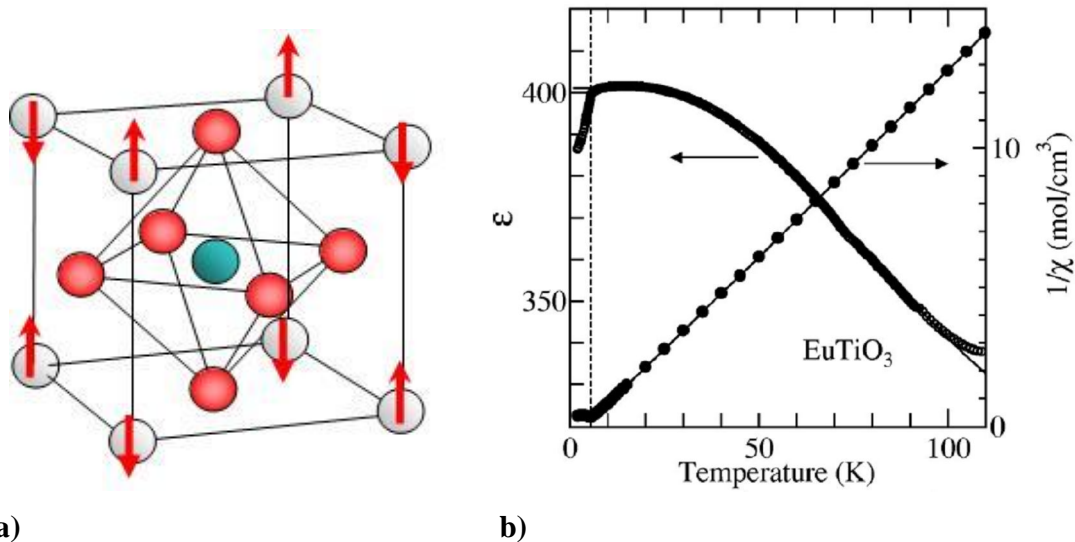


Fig.4.1.a) The structure of EuTiO<sub>3</sub> with G-type AFM arrangement of  $\text{Eu}^{2+}$  spins. Light grey circles in the corners are  $\text{Eu}^{2+}$  cations, the red arrows indicate orientations of their spins in the AFM phase. Red circles on the cubic faces are oxygens and blue circle in the centre mark Ti ions; b) Temperature dependence of dielectric constant at 100 kHz (left axis) and inverse magnetic susceptibility (right axis) of ETO (after ref.122)

As regards the dielectric and structural properties, ferroelectric (FE) order does not take place in ETO due to quantum PE behavior i.e. the quantum fluctuations prevent the freezing of polarization at low temperatures. It is demonstrated by temperature dependence of  $\epsilon'$ , which increases on cooling and saturates below 30 K (See Fig.4.1b).<sup>122</sup> Very recent heat capacity measurements revealed a structural phase transition (PT) near 280 K in ETO.<sup>124</sup> It could be an antiferrodistortive (AFD) PT (multiplication of unit cell and change of structure to tetragonal

phase), similarly as in STO, but its clear experimental evidence is still missing in literature. Below  $T_N=5.3$  K,  $\varepsilon'$  drops down, due to the spin-phonon coupling (See Fig.4.1b).<sup>122</sup> The value of permittivity increases remarkably with applied magnetic field  $B$  and at  $B>1$  T  $\varepsilon'$  acquires values higher than in the paramagnetic (PM) phase. Due to influence of AFM order on the dielectric constant, it is obviously to consider that dielectric constant is dominated by the pair correlation of the Eu spins,  $\langle S_i S_j \rangle$ , where  $i$  and  $j$  refer to Eu sites next to each other. Katsufuji et al.[122] tried to explain this behavior using mean field calculation of the spin system with  $S=7/2$  on the cubic lattice and successfully fitted the  $\varepsilon'(T)$  dependence by formula

$$\varepsilon'(T, H) = \varepsilon_0(T)(1 + \alpha \langle \vec{S}_i \vec{S}_j \rangle) \quad (4.1)$$

where  $\varepsilon_0(T)$  is the dielectric constant in the absence of spin correlation which has been estimated by fitting the experimental curve of  $\varepsilon_0(T)$  under 0 T above  $T_N$  (Fig.4.1b). The parameter  $\alpha$  is a coupling constant between the spin correlation and the dielectric constant. The pair correlation of spins  $\langle \vec{S}_i \vec{S}_j \rangle$  is simply given by the product of  $\langle \vec{S} \rangle$  on two sublattices.

In another work<sup>125</sup>, Q. Jiang et al., showed that variation of the frequency of soft-phonon mode depends on the spin correlation between the nearest-neighbors Eu spins and it substantially changes under a magnetic field.

It is well known that three optical phonons of  $F_{1u}$  symmetry are IR active in cubic  $Pm\bar{3}m$  perovskite structure.<sup>126,127</sup>  $\varepsilon'(T)$  is caused mainly by the lowest frequency (TO1) mode, which is called the soft mode (SM).<sup>128</sup> The behavior of SM can be evaluated from IR reflectivity spectra measured at different temperature up to 600 K (Fig.4.2). Increase of reflectivity on cooling can be seen due to a decreasing phonon damping as well as a shift of the edge of the first reflectivity band (corresponding to SM) to lower frequency.



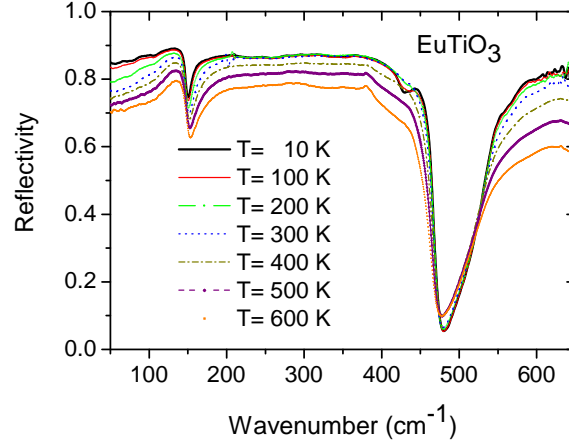


Fig.4.2. IR reflectivity spectra of ETO ceramics at selected temperatures (1 THz=33 cm<sup>-1</sup>)

For the fit of IR reflectivity, we used a generalized oscillator model with the factorized form of complex permittivity (see Eq.3.6). In Fig.4.3a) we present temperature dependence of the soft TO1 and TO2 modes obtained from IR reflectivity spectra fits. The SM frequency decreases (i.e. softens) from ~140 cm<sup>-1</sup> at 600 K down to ~85 cm<sup>-1</sup> on cooling and then it saturates below ~100 K. Dielectric contribution of the SM  $\Delta\epsilon_{SM}$  as well as a static permittivity increases due to the *Lyddane-Sachs-Teller relation* (see Eq. 2.15). The second mode in Fig.4.3a) is assigned as TO2 phonon and its frequency does not change significantly with temperature. Also highest-frequency TO4 mode exhibits insignificant temperature dependence (not shown here).

The SM frequency should obey the Cochran law (Eq.2.19) in the classical PE state<sup>129</sup>, but it saturates at low temperatures (as well as  $\epsilon'(T)$ ) and therefore the Cochran law is no more satisfied below 100 K. In this case it is more appropriate to use Barrett formula<sup>130</sup>

$$\omega_{SM}(T) = \sqrt{A\left[\left(\frac{T_1}{2}\right) \coth\left(\frac{T_1}{2T}\right) - T_0\right]} \quad (4.2)$$

Where  $T_1$  marks the temperature below which quantum fluctuations become important and  $T_0$  is a hypothetical critical temperature. In the Fig. 4.3a) are plotted the Cochran and Barrett fits of the SM. The parameters of the Barrett fit are the following:  $A = (27.45 \pm 1.3) \text{ cm}^{-2}\text{K}^{-1}$ ,  $T_1 = (154.6 \pm 9.8) \text{ K}$  and  $T_0 = (-170 \pm 29.3) \text{ K}$ .<sup>128</sup>

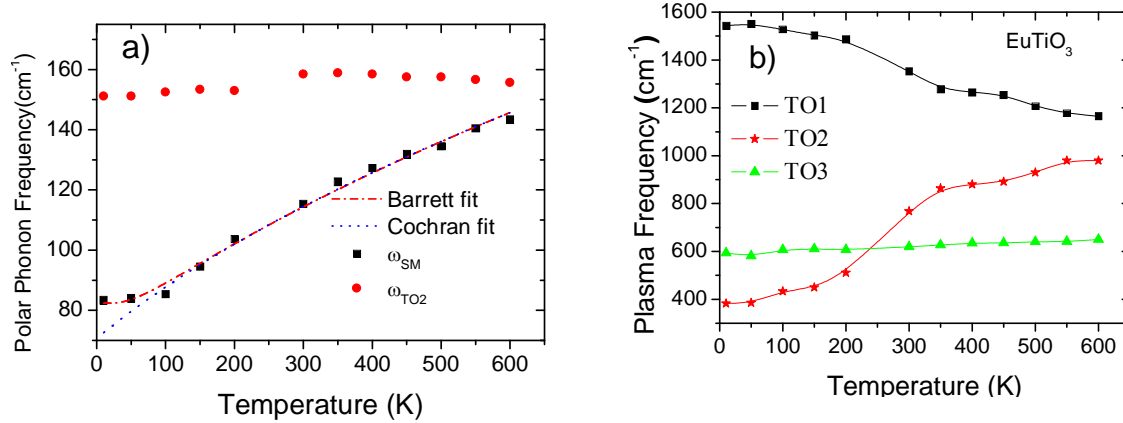


Fig.4.3. a) Temperature dependence of the SM and TO2 mode frequencies in ETO ceramics. In the figure are also presented results of the Barrett and Cochran fits; b) Temperature dependence of the mode plasma frequencies of the soft Slater-type TO1 mode (black squares), the Last TO2 modes (red stars) and the Axe TO4 mode (green triangles obtained from the IR reflectivity fits of ETO ceramics [after ref.128]

In order to establish which atom vibration takes part in each polar mode, we calculated the mode plasma frequencies

$$\Omega_{Pj} = \omega_{TOj} \sqrt{\Delta\epsilon_j}, \quad (4.3)$$

where  $\omega_{TOj}$  is transverse phonon frequency of the  $j^{\text{th}}$  phonon and  $\Delta\epsilon_j$  is the dielectric strength of the  $j^{\text{th}}$  mode for all the modes and plotted their temperature dependence in Fig.4.3b). The plasma frequencies are proportional to the mode effective charges which quantify the macroscopic electric response of a crystal to displacements of its atoms. If phonon eigenvector is temperature independent, the plasma frequency should be also temperature independent. Comparison of  $\Omega_{Pj}$  in ETO with  $\Omega_{Pj}$  observed in other similar perovskites indicates that the phonon eigenvectors in ETO are analogical to those of STO.<sup>131</sup> It is well known that the Born effective charge of B-site cation in  $ABO_3$  perovskite is the highest.<sup>132</sup> With this is related the fact that the Slater mode has the highest mode-plasma frequency. In other words, the SM in ETO as well as in STO is the Slater mode which expresses vibration of  $Ti^{4+}$  cations against the oxygen octahedra, the second (TO<sub>2</sub>) mode is called Last mode and it expresses a vibration of  $Eu^{2+}$  cations against the  $TiO_6$  octahedra. The highest frequency (TO4) mode is so called Axe mode and it represents bending of the O-octahedra.<sup>131</sup> (see all modes in Fig.4.4). TO3 mode is not shown in Fig.4.4, because it is silent in IR and Raman spectra.

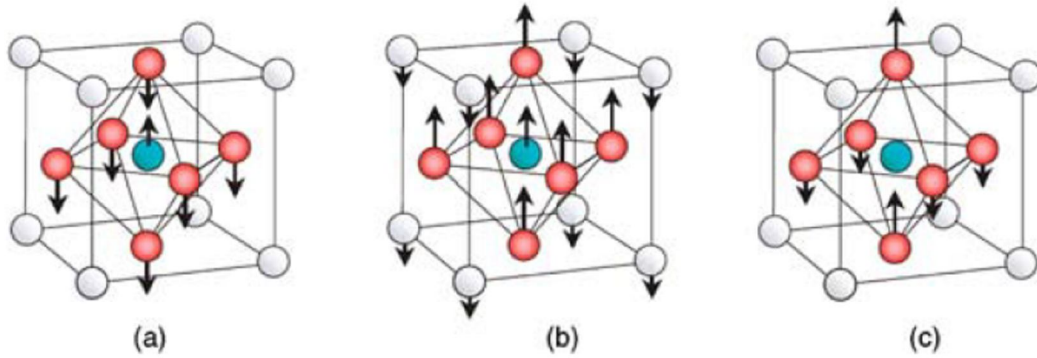


Fig.4.4. Eigen-displacements (normal coordinates) of a) Slater b) Last and c) Axe zone centre polar modes in cubic perovskites. Gray, blue and red balls mark perovskite A-site ions, B-site ions and oxygens, respectively (after Ref.[131])

However, the plasma frequency of the SM is decreasing on heating while that of the Last mode increases. It gives evidence about a coupling of both modes as well as about mixed character of both eigenvectors at high temperatures, where their frequencies approach to anti-crossing.

Our findings are in agreement with the first principle calculations of Fennie and Rabe<sup>133</sup>, showing that the spin order of Eu cations have direct influence on Slater vibrations of Ti-O<sub>6</sub>. In Ref.[128] we assumed that the Eu spin ordering in AFM phase influences the TO1 phonon frequency predominantly due to Eu-O-Eu AFM superexchange interaction. However, recent calculations using Hartree-Fock approximation show that the spin alignments of Eu<sup>2+</sup> ions has a significant impact on the dielectric constant through the Eu-Ti-Eu AFM superexchange interactions<sup>134</sup>. This interaction causes the coupling of TO1 (soft) and TO2 modes<sup>134</sup> and is microscopic origin of the large magnetodielectric effect observed in ETO.

The ab-initio calculations of lattice dynamics predict that the phonon branches of ETO have instability near Brillouin zone (BZ) boundary in M and R-point of reciprocal space (see Fig. 4.5), i.e. the PT should be connected with multiplication of unit cell and the centre of symmetry should remain, it means the PT should be antiferrodistortive (AFD)<sup>135</sup>. The same calculations suggest that the new structure should be tetragonal one with I4/mcm space group due to a<sup>0</sup>a<sup>0</sup>c<sup>-</sup> tilt (in Glazer notation).<sup>136</sup>

We tried to find the predicted PT using the investigation of temperature dependence of Young's modulus and thermal expansion. The measurement we performed in

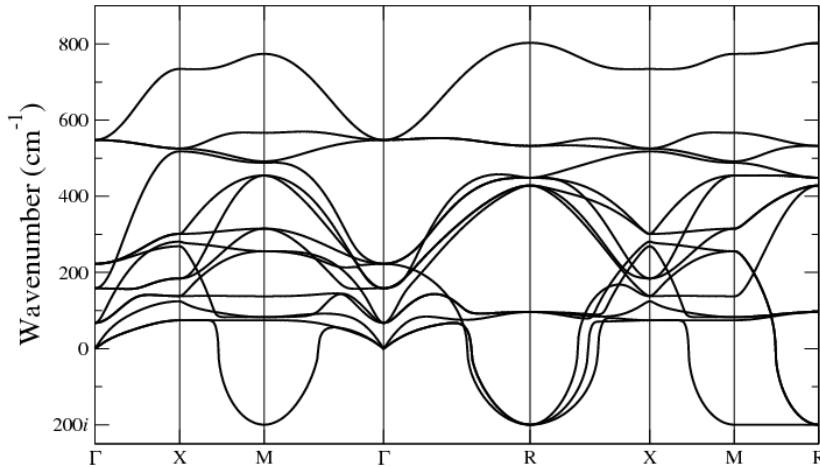


Fig. 4.5. The phonon branches of ETO in the  $k$ -space obtained by ab-initio calculations (after Ref.135). Instabilities in M and R points of BZ are expressed by imaginary eigenfrequencies.

Vienna using the instrument for Dynamical Mechanical Analysis (DMA7-Perkin Elmer). We really discovered an anomalies around 300 K in the cooling and heating curves. (see Fig.4.6) These anomalies could be a signature of structural PT.

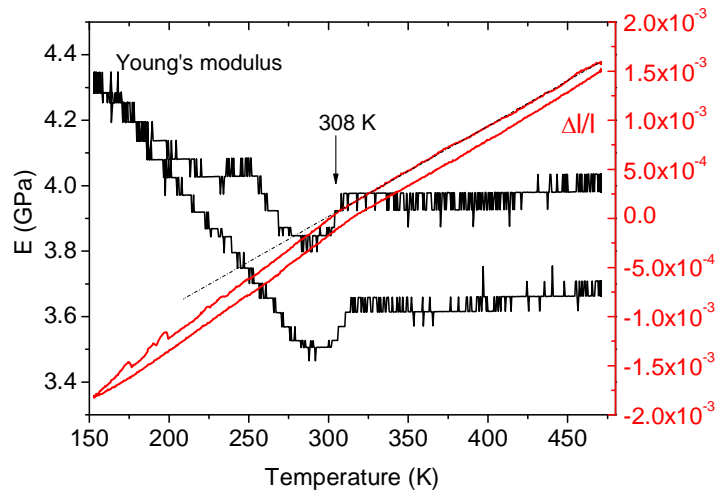


Fig.4.6. Temperature dependence of Young's modulus  $E$  and thermal expansion  $\Delta/l$  in bulk ETO ceramics

In order to clarify whether the AFD PT takes place, our colleagues O. Pacherová, J. Drahokoupil and F. Laufek from Institute of Physics performed X-ray diffraction study of ETO ceramics. Several diffraction spots really exhibit gradual splitting on cooling below room temperature (see Fig. 4.7). Rietveld refinement of diffraction patterns finally confirmed the

I4/mcm space group with  $3.5^\circ$  rotation along the c axis (measured at 193 K). The refined crystal structure (I4/mcm space group) is shown in Fig. 4.8.

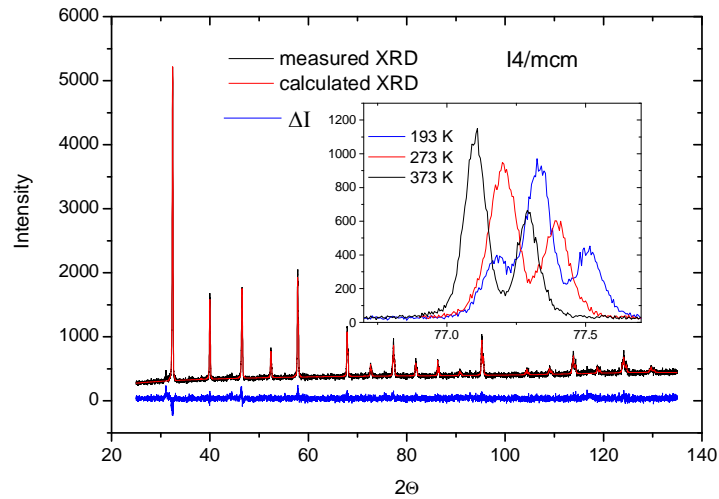


Fig.4.7. The X-ray diffraction patterns of ETO ceramics taken at 193 K. (black curve). Red curve marks theoretical curve, blue one the difference between experimental and theoretical one. Inset shows example of gradual splitting and shifts of two diffraction spots on cooling from +373 K down to 193 K.

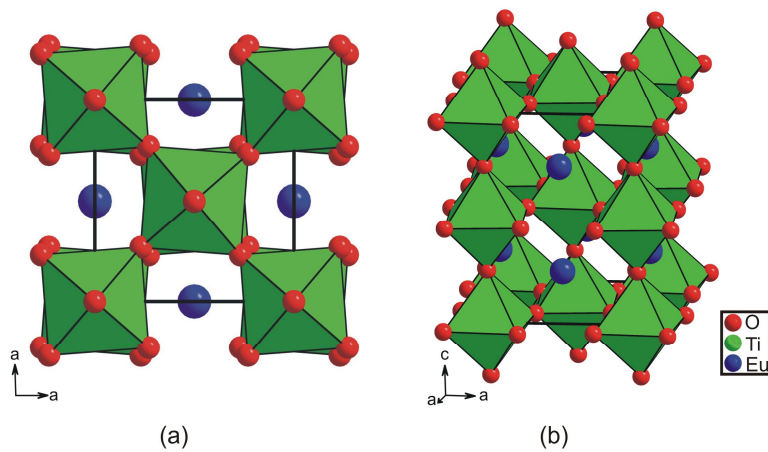


Fig.4.8. AFD structure of ETO (I4/mcm space group created by  $a^0a^0c^-$  tilt) refined from X-ray diffraction taken at 193 K (view from different crystal directions).

The AFD tetragonal phase keeps the centre of symmetry, but the unit cell is enlarged. This causes the folding of the BZ. In such conditions some modes from BZ boundary, which were silent in cubic phase, become IR active. Another important consequence of the structural PT

to tetragonal phase is that all the three polar modes originally seen in cubic phase should split below the PT temperature and moreover the silent TO3 mode could become IR active.

An important feature in bulk ETO is the strong magnetodielectric effect i.e. the change of permittivity with magnetic field  $\mathbf{B}$  below  $T_N$ .<sup>122</sup> The magnetodielectric effect  $\Delta\varepsilon(\mathbf{B})/\varepsilon(0)$  was found to be 7 % in single crystal.<sup>122</sup> We measured also magnetodielectric effect in polycrystalline ETO (i.e a crystalline grains of orders of 0.1-1 mm) in two different configurations:  $\mathbf{B}$  oriented parallel to electric field  $\mathbf{E}$  (i.e.  $\mathbf{B}$  perpendicular to the surface of the sample) and  $\mathbf{B}\perp\mathbf{E}$  (i.e.  $\mathbf{B}$  lies in the plane of the sample). We found that the magnetodielectric effect is strongly anisotropic. The magnetodielectric effect is smaller in  $\mathbf{B}\parallel\mathbf{E}$  orientation than in  $\mathbf{B}\perp\mathbf{E}$  .(see Fig.4.9)

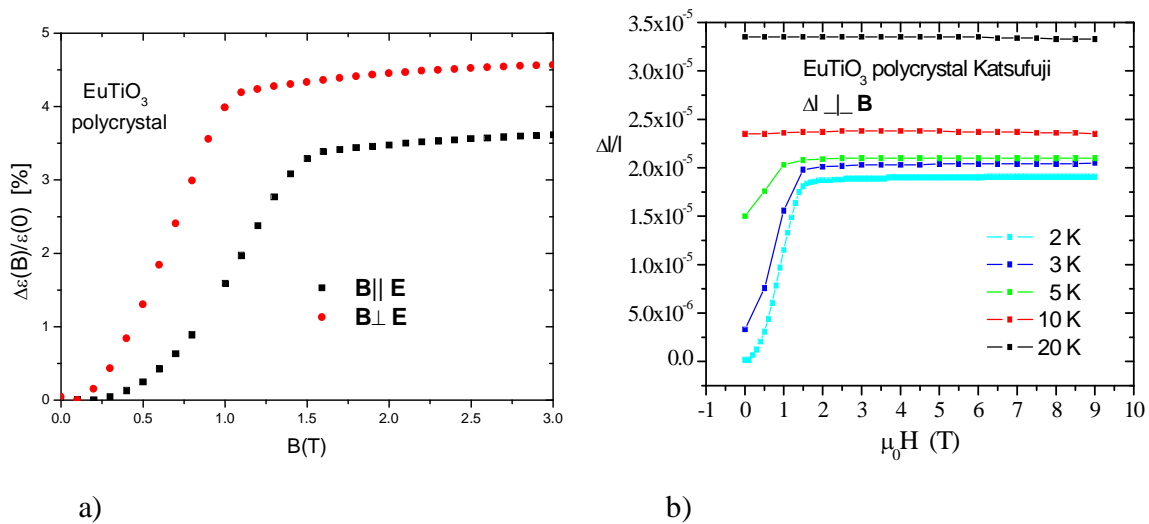


Fig.4.9 a) The magnetic field dependence of magnetodielectric effect  $\Delta\varepsilon(\mathbf{B})/\varepsilon(0)$  measured at 2 K for two different orientations of  $\mathbf{E}$  and  $\mathbf{B}$ . b) Magnetostriction at various temperatures.

In first attempt, we tested whether the anisotropic magnetodielectric effect cannot be caused by anisotropic magnetostriction. In Fig. 4.9b) we show that the magnetostriction exhibits change of dimension only of order  $10^{-5}$  while the change of permittivity is of order of  $10^{-2}$ . This huge discrepancy cannot explain the magnetodielectric effect. Finally, the most plausible explanation is that the structure is no more cubic due to AFD PT and then we have different behavior in different directions of the sample (values of magnetoelectric tensor are different).

Our new IR reflectivity measurements of high purity and dense ETO ceramics reveal three new polar modes arising below 300 K (see Fig.4.10a). Splitting of TO1 and TO4 mode is seen also in ETO single crystal (Fig. 4.10b). The new modes are indicated by the arrows. The same

weak modes were revealed already in previous IR investigations by Kamba et al.<sup>148</sup>, but they were interpreted as defect modes from pyrochlore second phase (their intensities increased with enhanced pyrochlore concentration). Our samples are pure perovskite ETO, so the new modes must be activated due to breaking of the cubic symmetry.

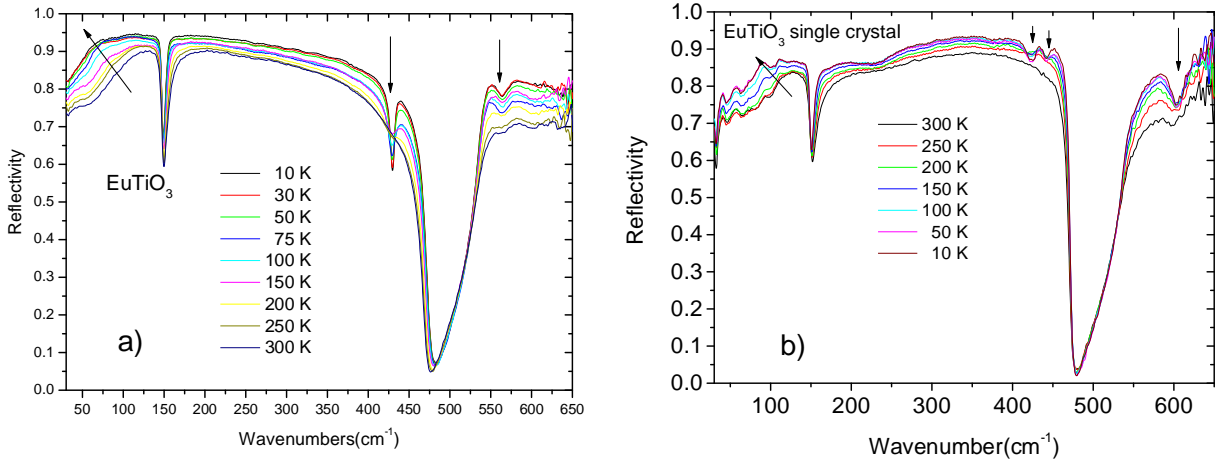


Fig.4.10. IR reflectivity spectra of a) ETO ceramics and b) ETO single crystal. The new modes activated due to AFD PT are marked by the arrows. The spectra of single crystal are less accurate below  $100 \text{ cm}^{-1}$  due to the small dimensions of the sample.

For the fit of reflectivity, we used the generalized-oscillator model with the factorized form of the complex permittivity (Eq. 3.6). The temperature dependence of phonon frequencies and complex dielectric function in ETO can be extracted from the fits of reflectivity spectra. The TO1 mode has the frequency of  $103 \text{ cm}^{-1}$  at room temperature, but below this temperature the SM splits into two components (see Fig. 4.11). At 10 K the SM components in ETO ceramics have frequencies of  $78 \text{ cm}^{-1}$  and  $63 \text{ cm}^{-1}$ . In single crystals the SM components have higher frequencies, but these modes were determined with lower accuracy due to smaller dimension of single crystal, which limits the spectra sensitivity. Striking difference is that the new and weak component of the SM (marked as TO1s in Fig. 4.11.) has lower frequency in ceramics than the original TO1 SM, while in single crystal the TO1s mode has higher frequency than the original SM, which has more-less the same frequency in both kinds of samples. TO4 mode seen near  $550 \text{ cm}^{-1}$  exhibits splitting already at room temperature, but TO2 splitting was not detected. Nevertheless, sharp new mode arises in the IR spectra of ETO ceramics around  $430 \text{ cm}^{-1}$ . This mode according to first principle calculations<sup>135</sup> corresponds to silent TO3 mode. It is interesting that a doubled was observed around the same frequency in ETO single crystal. Its origin is not

clear, but it can be caused by lower than tetragonal symmetry of the single crystal. Also the dielectric measurement in single crystal (performed by M. Savinov from our group) exhibits twice lower value of  $\epsilon'$  than the reported results in Ref. 122. This can be explained either by different symmetry or strong anisotropy of the crystal, which was not oriented in our case (c axis was tilted about  $60^\circ$  out of plane normal).

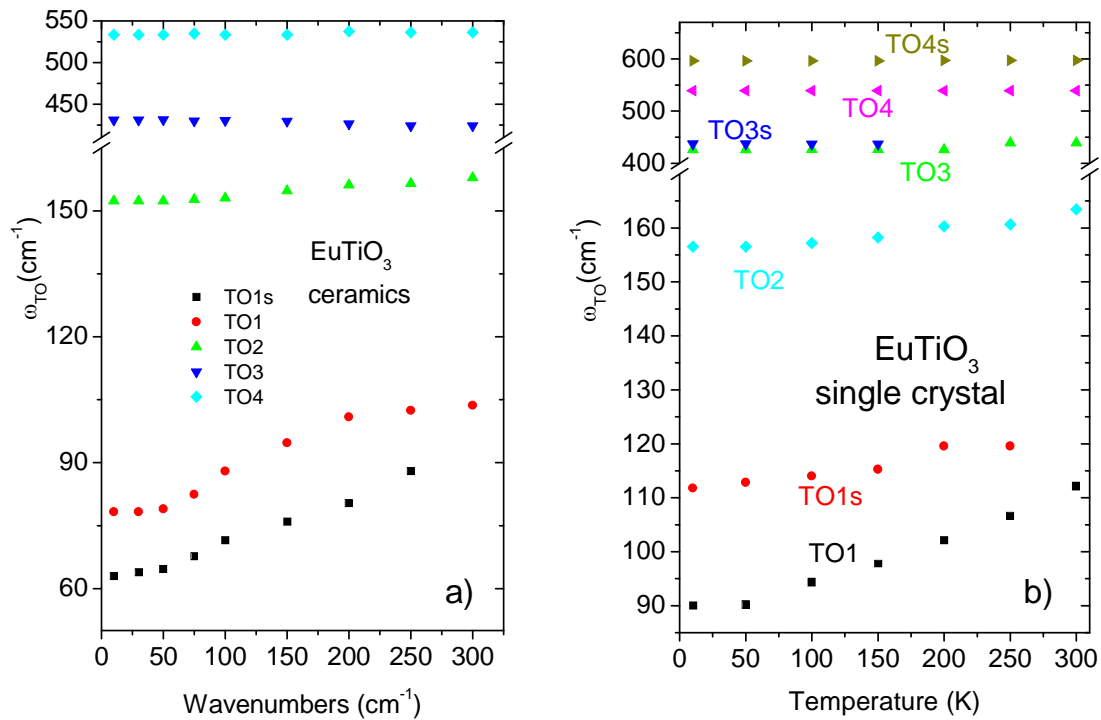


Fig.4.11. Temperature dependence of the polar mode frequencies in a) ETO ceramics b) ETO single crystal. The phonon frequencies were obtained from the fits of IR reflectivity in Fig. 4.10. The split modes are marked as TO1s and TO3s.

Finally, the complex dielectric spectra of bulk ETO ceramics obtained from the fits are depicted in Fig.4.12. The frequencies of maxima in  $\epsilon''(\omega)$  roughly correspond to  $\omega_{\text{TO}_j}$  frequencies. The softening of the SM on cooling is clearly seen. The plots of  $\epsilon''(\omega)$  is presented in logarithmic scale because the new weak mode around  $430 \text{ cm}^{-1}$  is not seen in the linear scale.



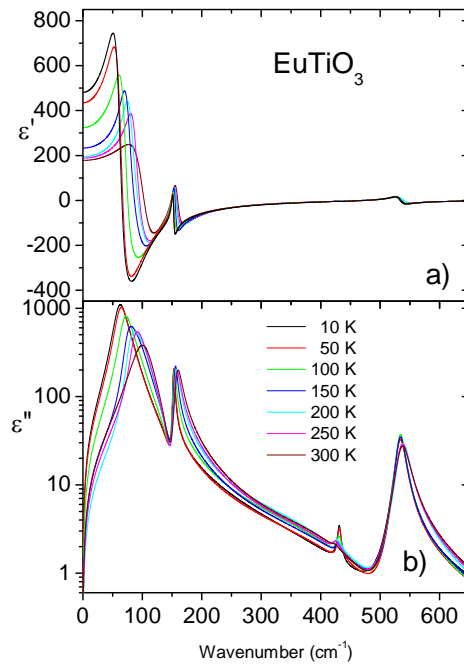


Fig.4.12. a) Real and b) imaginary part of complex permittivity of ETO ceramics obtained from the fits of IR reflectivity spectra.

### 4.3 $\text{Eu}_{0.5}\text{Ba}_{0.5}\text{TiO}_3$ (EBTO) and $\text{Eu}_{0.5}\text{Ba}_{0.25}\text{Sr}_{0.25}\text{TiO}_3$ (EBSTO) ceramics

#### 4.3.1 $\text{Eu}_{0.5}\text{Ba}_{0.5}\text{TiO}_3$ ceramics

The new multiferroics  $\text{Eu}_{0.5}\text{Ba}_{0.5}\text{TiO}_3$  (EBTO) was suggested and synthesized by our colleagues for search of permanent electric dipole moment (EDM) of the electron.<sup>137</sup> The problem of existence a non-zero tiny EDM of elementary particles is known already since 1950's.<sup>138</sup> The idea of permanent EDM of particles was further supported by the Standard model of particles, explaining among others the CP-symmetry violation (C and P denote charge and parity, respectively), experimentally discovered in the sixties.<sup>139</sup> The authors of the Standard model of particles received Nobel price in 2008.

The idea of EDM measurement rests on the fact that the magnetic moment of the electron spin and the permanent EDM are parallel (or antiparallel). Switching of external electric field applied on the sample should switch the EDM of electron as well as the spin, so that a linear change of magnetization with electric field should be detectable in sensitive magnetometer. Thus, the experimental goal is to see the intrinsic linear magnetoelectric (ME) effect associated with the electron EDM.

EBTO (solid solution of AFM  $\text{EuTiO}_3$  and FE  $\text{BaTiO}_3$ ) is a good candidate for such measurements due to the large internal electric field  $\sim 10 \text{ MVcm}^{-1}$  which acts on off-center displaced magnetic Eu cations already without any external electric field.<sup>137</sup> Moreover, the internal electric field is switchable by external electric field with amplitude three orders of magnitude smaller. The change of direction of large internal electric field should have influence on direction of EDMs and hence spins (magnetization). Another advantage is that each  $\text{Eu}^{2+}$  cations has 7 unpaired  $4f$  electrons resulting in a large magnetization<sup>140</sup>, hence its change with electric field should be measurable with sensitive SQUID magnetometers.<sup>137</sup> It is important to emphasize that EDM measurement takes places in paramagnetic phase where macroscopic linear ME effect is forbidden by symmetry.

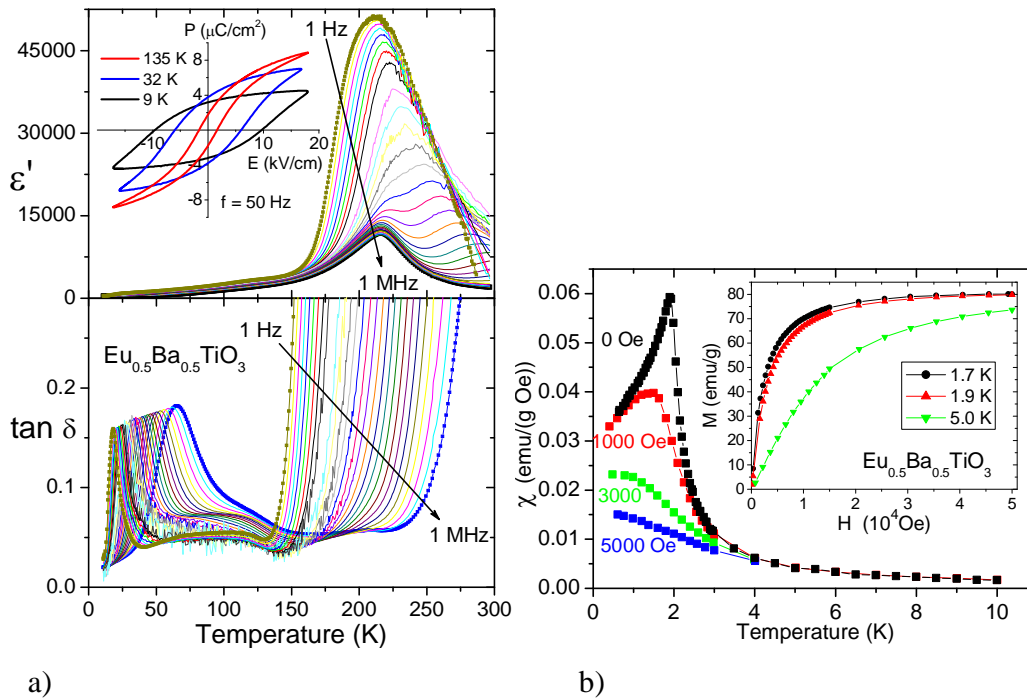


Fig.4.13. a) Temperature dependence of permittivity and dielectric loss. Inset shows ferroelectric hysteresis loops at various temperatures. b) Temperature dependence of magnetic susceptibility. Inset shows magnetization curves at various temperatures.

We found that EBTO is FE below 215 K and AFM below 1.9 K (see Fig. 4.13).<sup>137, 141</sup> These properties were proved by different types of measurements. The AFM critical temperature was obtained by measuring temperature dependence of magnetic susceptibility exhibiting maximum

at  $T_N$ . Critical FE temperature we determined from the maximum of  $\epsilon''(T)$  measured at 1 MHz ( $\epsilon'$  at this frequency is not influenced by conductivity). Observed FE hysteresis loop also supports the FE ordering. Details we published in Ref [137].

Using IR reflectivity measurements, we demonstrated that the FE PT is mainly displacive i.e. driven by the SM. The IR spectra are shown in the Fig. 4.14. No dramatic change in reflectivity spectra can be seen; only a small increase of intensity due to decrease of phonon damping was observed on cooling. At room temperature the structure is cubic perovskite  $Pm\bar{3}m$  and therefore three optical modes with  $F_{1u}$  symmetry are IR active. This corresponds to three IR reflection bands seen in the Fig. 4.14, polar frequencies are marked by TOj (j=1-4). Three additional weak modes seen near 180, 300 and 330  $\text{cm}^{-1}$  and marked by red arrows probably correspond to impurity modes. The IR reflectivity is very sensitive to small amount of impurities (<1%) even if the XRD did not reveal any impurities. These impurities correspond probably to unreacted  $\text{BaTiO}_3$  powder.

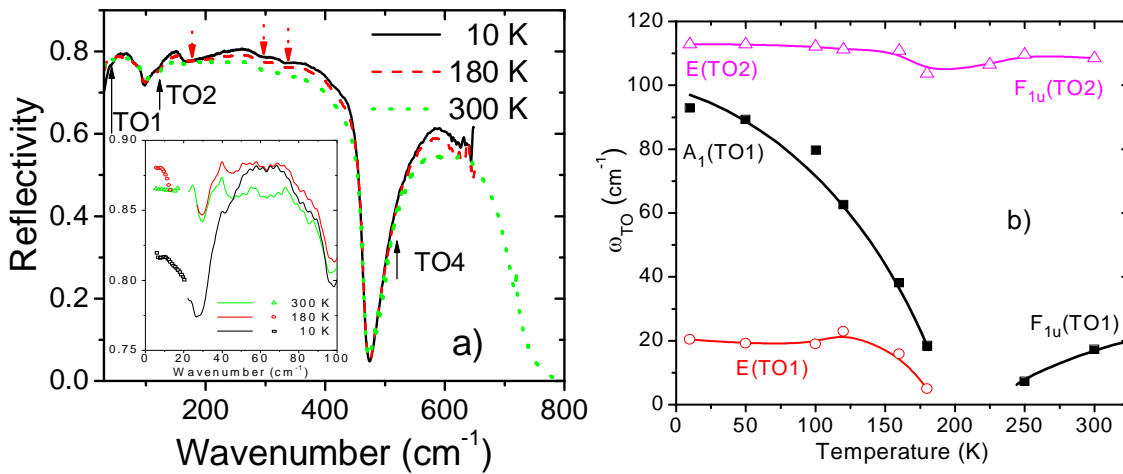


Fig.4.14. a) IR reflectivity spectra of EBTO ceramics at selected temperatures.  $F_{1u}$  modes are indicated with black arrows while the impurity modes are indicated with red arrows. Temperature dependence of low-frequency TO modes obtained from the fit of reflectivity together with THz data (see the inset in Fig.4.14a). Assignments of the mode symmetry species are appropriate to the rhombohedral structure.

According to XRD data (see Ref.141), the structure becomes orthorhombic below  $T_C$  with  $Amm2$  space group. Therefore, the spectra should be more complicated due to a change of IR selection rules. However, no dramatic changes were found in the spectra. The intensity of reflection bands increase on cooling, because of decreasing phonon damping, but no new modes are revealed in

the spectra. It means that the intensity of newly activated modes is probably very small or these modes are overlapped and screened by modes already active in the PE phase.

The behavior of the transverse optical TO1 and TO2 polar phonons are plotted in Fig. 4.14b). One can see a splitting of the TO1 mode below 200 K into two components (E and A<sub>1</sub> symmetry) which harden on cooling. It was used conventional notation for the mode symmetry species appropriate to the rhombohedral structure, because each mode should split into three components in the orthorhombic phase. However, there are seen only two components probably due to overlapping of the third components with other two.

The A<sub>1</sub> mode is well seen in IR reflectivity while the E component is resolved only in the THz spectra (see Fig. 4.14b and Fig.4.15). At 10 K the E component of TO1 mode reaches 20 cm<sup>-1</sup> and the A<sub>1</sub> component of the polar soft mode increases up to 95 cm<sup>-1</sup>. The very low frequency of the E component of TO1 mode is reminiscent of the situation of BaTiO<sub>3</sub> and gives evidence of a strong lattice anharmonicity and large dielectric anisotropy in the FE phase.<sup>142</sup> In the temperature region between 180 and 250 K, the sample becomes non transparent in the THz region, as a result of the low frequency, high damping and strong intensity of the TO1 SM near  $T_C$ . For this reason, some points are missing between 180 K and 250K in Fig.4.14. However the SM behavior is predictable in this temperature region and the SM frequency minimum can be expected at  $T_C=215$  K where the peak in  $\epsilon'(T)$  occurs. In such context, the FE PT is displacive one. The TO2 mode also shows a small anomaly near  $T_C$ . The TO4 mode with a frequency of 513 cm<sup>-1</sup> is not presented here because it remains unchanged at all temperatures.

In Fig.4.15, we show the real and imaginary parts of the complex dielectric spectra obtained from the fit of IR reflectivity at selected temperatures. Symbols are experimental THz data and lines are results of the THz and IR fits. The peaks in  $\epsilon''(T)$  correspond to eigenfrequencies of TO phonons in EBTO. Softening and splitting of TO1 mode is clearly seen.

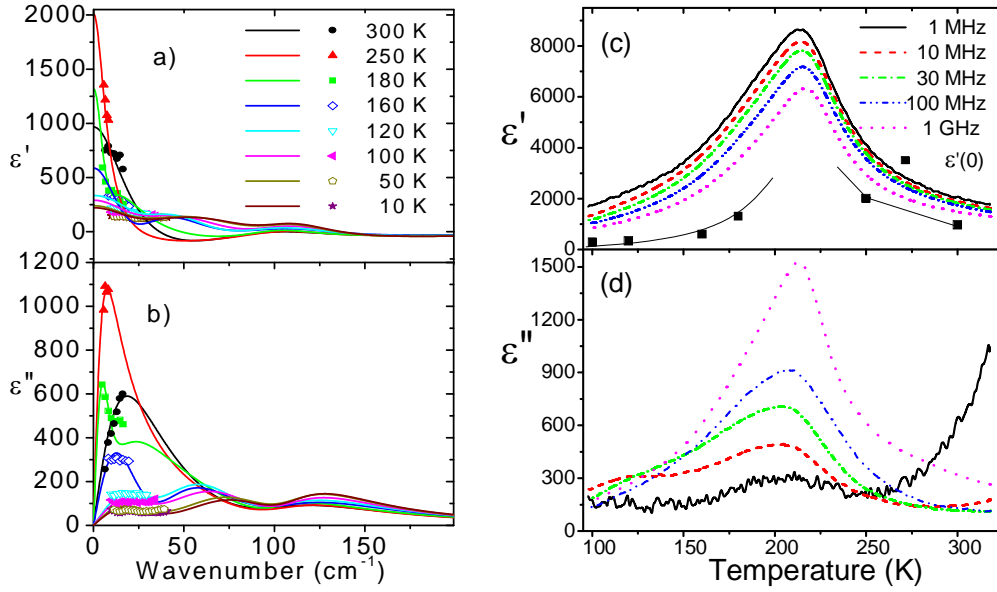


Fig.4.15. a) Real and b) imaginary parts of permittivity spectra in EBTO ceramics obtained from fits of THz and FIR spectra. Symbols are experimental THz data. Higher frequency part of the spectra is not shown, because the TO4 mode at  $513 \text{ cm}^{-1}$  does not exhibit any remarkable temperature changes. Temperature dependence of the c) real and d) imaginary part of the complex permittivity in the microwave region together with the sum of phonon and electronic contributions ( $\epsilon'(0)$ ). The missing data between 180 and 250 K are due to the lack of THz data as consequence of opacity of the sample in the THz range.

The dielectric contribution  $\Delta\epsilon_j$  of each phonon can be calculated using Eq.3.7. Static permittivity  $\epsilon'(0)$  caused by contributions of all polar phonons can be obtained from the formula

$$\epsilon'(0) = \epsilon_\infty + \sum_j \Delta\epsilon_j \quad (4.4)$$

where  $\epsilon_\infty$  is electronic contribution to the static permittivity. We have calculated temperature dependence of static  $\epsilon'(0)$  and plotted it in Fig.4.15c) together with  $\epsilon'(T)$  obtained between 1 MHz and 1 GHz. The value of  $\epsilon'(0)$  exhibits a huge change with temperature due to the change of SM frequency with temperature. The microwave (MW) data show that the peak in  $\epsilon'(T)$  does not shift with frequency, so our sample is not a relaxor FE. The magnitude of the  $\epsilon'(T)$  peak decreases from approximately 9000 at 1 MHz down to 6500 at 1 GHz. Details are published in Ref. 141.

### 4.3.2 $\text{Eu}_{0.5}\text{Ba}_{0.25}\text{Sr}_{0.25}\text{TiO}_3$ ceramics

$\text{Eu}_{0.5}\text{Ba}_{0.5}\text{TiO}_3$  has at low temperatures rather high coercive field of  $10 \text{ kV/cm}^{-1}$ , which causes heating of the sample during switching of polarization. It significantly reduces sensitivity of EDM measurement. Therefore we have proposed to use  $\text{Eu}_{0.5}\text{Ba}_{0.25}\text{Sr}_{0.25}\text{TiO}_3$  (EBSTO) for EDM measurement, because Sr should reduce both  $T_C$  and coercive field. M. Savinov performed measurements of permittivity below 1 MHz and really discovered  $T_C$  around 135 K (see Fig.4.16 a). His measurement of hysteresis loops also revealed that coercive field is three times smaller in EBSTO than in EBTO, so it is more suitable for EDM search. From magnetic point of view, temperature dependence of magnetic susceptibility measured at different magnetic fields show that the Néel temperature is  $\sim 1.8 \text{ K}$ . Thus, the presence of Sr did not affect the magnetic PT – Fig.4.16 b), because the concentration of magnetic Eu ion is the same in EBTO and EBSTO.

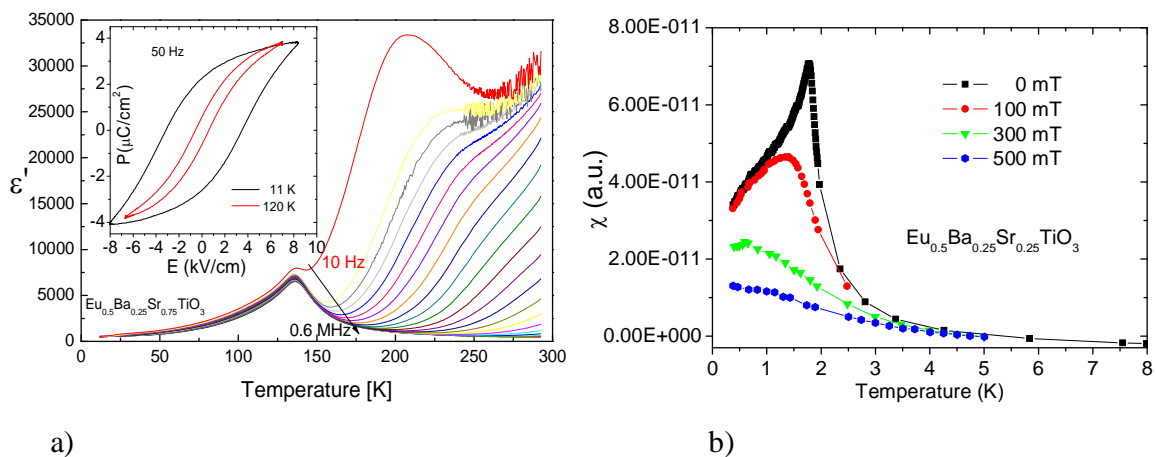


Fig. 4.16. Temperature dependence of a) dielectric permittivity and b) magnetic susceptibility.

We measured and analyzed EBSTO IR spectra in the same way as EBTO. In Fig.4.17 some selected IR reflectivity spectra taken below 300 K are shown. As in the case of EBTO, the spectra of EBSTO do not change with temperature too much, but they are different than in the case of EBTO. The XRD measurements (not shown here) reveals a cubic structure in this compound down to 200 K. Nevertheless, we do not see three reflection bands typical for simple cubic perovskite structure. A possible explanation is so called multimode behavior.<sup>143</sup> It means that due to three different types of ions (i.e. Eu, Ba, Sr) in the A perovskite sites each ion exhibits

different vibration frequency and therefore we see higher number of modes than is allowed from the group theory.

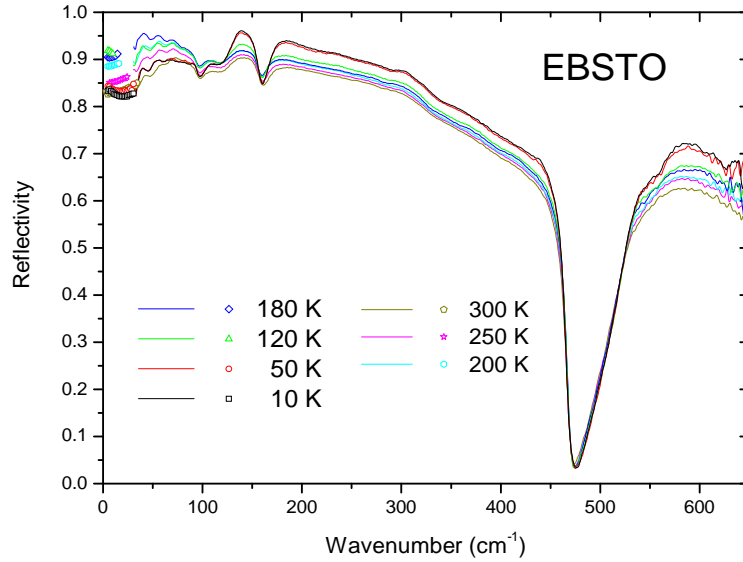


Fig.4.17. The IR reflectivity and THz spectra of EBSTO below room temperature.

The phonon behavior in EBSTO is shown in the Fig. 4.18a. The SM softens from  $57 \text{ cm}^{-1}$  at room temperature down to  $30 \text{ cm}^{-1}$  near the PT. Below  $150 \text{ K}$ , a new heavily-damped mode arises at  $6 \text{ cm}^{-1}$  and hardens up to  $12 \text{ cm}^{-1}$ . Third component of the SM arises below  $50 \text{ K}$  near  $50 \text{ cm}^{-1}$ . These two new components of the SM were resolved only due to simultaneous fit of IR and THz spectra. Note three modes near  $100 \text{ cm}^{-1}$ ,  $130 \text{ cm}^{-1}$  and  $160 \text{ cm}^{-1}$ , which are seen at all temperatures. These are probably split TO2 mode due to aforementioned multiple occupation of the A-perovskite site. The third reflectivity band seen above  $500 \text{ cm}^{-1}$  and assigned as TO4 mode exhibits no split below the room temperature and its frequency is temperature independent.

Static permittivity  $\epsilon'(0)$  obtained as the sum of dielectric contributions of all polar phonons (Eq. 4.4) is plotted in Fig.4.19. Together with  $\epsilon'(0,T)$  is plotted also experimental curve of  $\epsilon'$  obtained at  $0.641 \text{ MHz}$ . The sum of phonon contributions to  $\epsilon'(0)$  is in good agreement with experimental data in PE phase. Close below  $T_C$  the  $\epsilon'(0)$  is lower than the experimental curve at  $0.641 \text{ MHz}$  probably due to additional contributions of FE domains to  $\epsilon'$ . Due to the lack of THz data between  $120$  and  $180 \text{ K}$  (sample becomes opaque in this temperature range) we could not evaluate properly the spectra near  $T_C$ . In Fig.4.19 are shown also dielectric contributions of each component of the SM resolved below  $T_C$ .

The THz data together with complex dielectric spectra obtained from the fits of IR reflectivity are shown in the Fig.4.18b. Real and imaginary part of complex permittivity exhibits one peak below  $100\text{ cm}^{-1}$  above  $T_C$  corresponding to eigenfrequency of the SM. When the PT occurs two peaks are arising in dielectric spectra due to splitting of the SM.

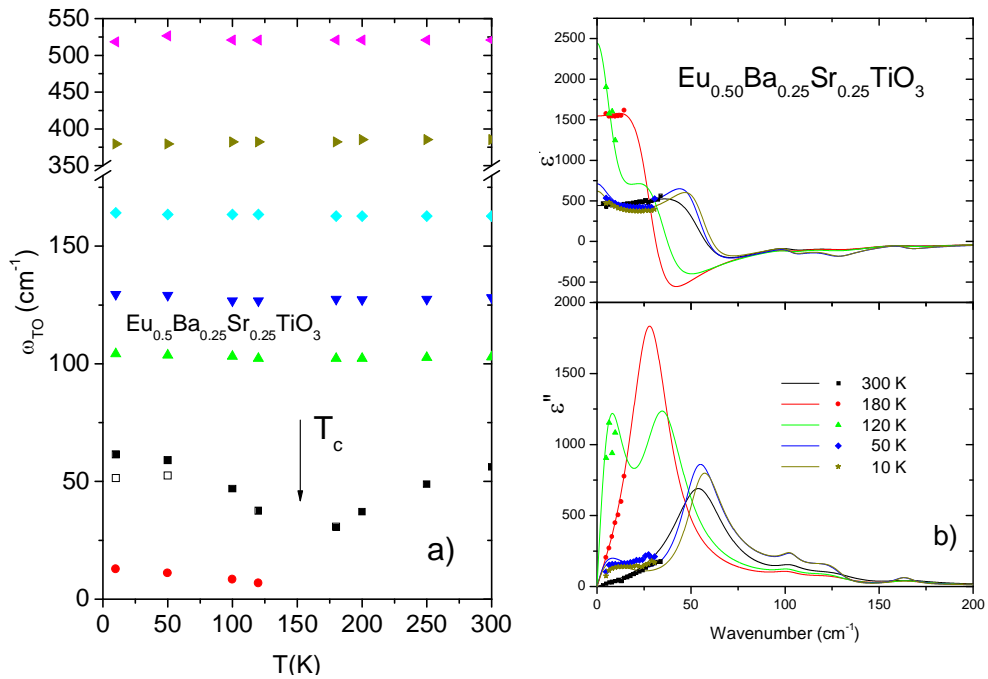


Fig.4.18.a) Temperature dependence of polar phonons in EBSTO. The SM is marked by black squares. b) Complex dielectric spectra together with THz data are plotted at selected temperatures below 300 K.

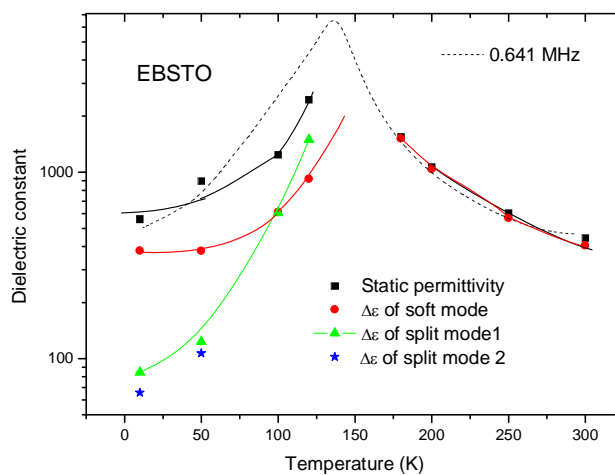


Fig.4.19 Temperature dependence of static permittivity from phonon contributions, SM dielectric strength and dielectric contributions of activated mode 1 and 2 below PT. It is plotted also the experimental curves of permittivity at 0.641 MHz.



#### 4.4 EuTiO<sub>3</sub> thin films

The interest in ETO thin films was increased when in 2006 the theoretical article<sup>133</sup> was published in which ETO system was predicted to exhibit strong ferromagnetism (spontaneous magnetization,  $\sim 7\mu_B$  per Eu) and strong ferroelectricity (spontaneous polarization,  $\sim 10 \mu\text{Ccm}^{-2}$ ) simultaneously under large biaxial strain, although the bulk ETO is AFM and quantum PE at low temperatures.<sup>122</sup> The required material characteristics are a strong spin-phonon coupling through which the AFM order changes to FM one and a low-frequency polar phonon that is strongly sensitive to epitaxial strain. The predicted competition between an AFM-PE phase and a FM-FE phase allows magnetic phase control with an applied electric field, and electric phase control with an applied magnetic field, with modest critical fields. The phase diagram of ETO thin films versus biaxial strain is depicted in Fig.4.20.

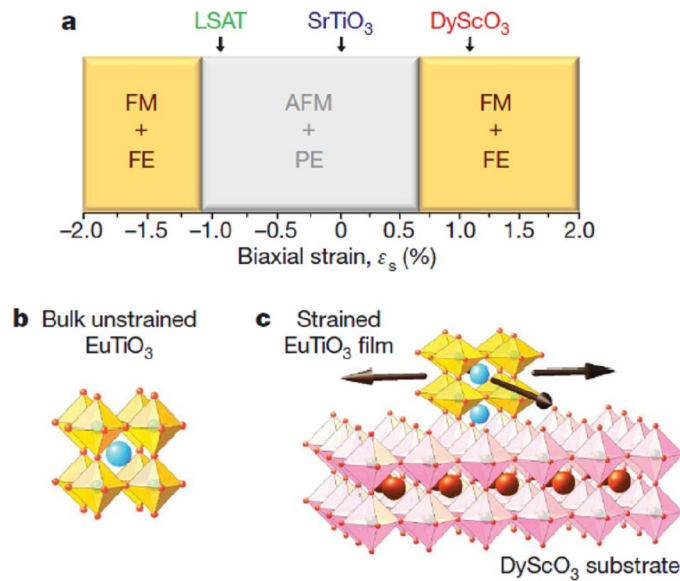


Fig.4.20. a) Phase diagram of ETO strained from - 2% (biaxial compression) to +2% (biaxial tension) obtained from *ab-initio* calculations; b) the structure of the bulk unstrained ETO and c) a sketch of the shape of strained ETO thin film on the DSO substrate. (after Ref.144)

According to theoretical calculations, we used the following substrates: a) (110) oriented DyScO<sub>3</sub> (DSO) substrate, which evokes tensile strain in ETO thin film. b) (001) oriented (LaAlO<sub>3</sub>)<sub>0.29</sub>–(SrAl<sub>1/2</sub>Ta<sub>1/2</sub>O<sub>3</sub>)<sub>0.71</sub> substrate (abbreviated as LSAT). c) (001) LaAlO<sub>3</sub> (LAO) and d) (110) NdGaO<sub>3</sub> (NGO). Substrates b), c) and d) evoke compressive strain in the thin ETO films. Real strain in the thin films was calculated using a well-known formula for misfit strain:

$\eta = \frac{a_{\text{exp}} - a}{a_{\text{exp}}}$  where  $a_{\text{exp}}$  is the experimental lattice parameter in plane of ETO thin film and  $a$  is

the bulk lattice parameter of the ETO. In the perfectly strained thin film  $a_{\text{exp}}$  is the same as lattice parameter of the substrate. In this case we have a theoretical strain. In reality, the thin films are not perfectly commensurate with the substrate, the strain frequently relaxes. Therefore, the strain in the film could be much lower than theoretical expectations.

In literature, there were several attempts to grown ETO thin films and to study their properties.<sup>145,146,147</sup> Many publications were made on unstrained ETO thin films deposited on (001) STO substrate using pulsed laser deposition (PLD).<sup>145,146</sup> It was found that the AFM order tend to convert to FM one when c-axis of ETO is increased. Also, other group reports the optical band gap in this type of thin film. They found that unstrained  $\text{EuTiO}_3$  film grown on (001) STO has a direct optical band gap of 0.93 eV.<sup>147</sup>

#### ***4.4.1 Biaxially tensile strained $\text{EuTiO}_3$ thin films***

Previous measurements of IR reflectance of ETO incipient FE ceramics have shown that low frequency  $\epsilon'$  is determined only by contributions of polar phonons i.e. no dielectric dispersion has been observed below the phonon frequencies.<sup>148</sup> Polar phonons should exhibit strong anomalies near a displacive FE PT. For that reason we investigated FIR reflectance of 22, 42, 75 and 100 nm thick ETO films (all strained in biaxial tension by +1.1%) on (110) DSO substrates.

The X-ray diffraction and cross-sectional scanning transmission electron microscopy (not shown here) reveal the films to be commensurate with the substrate, smooth and structurally perfect (see Ref.144). In this chapter we will present the results obtained only on 100 nm thick ETO film deposited on DSO, because the phonons from this thin film are best resolved in the IR spectra. IR reflectance spectra of thinner films gave qualitatively the same results.

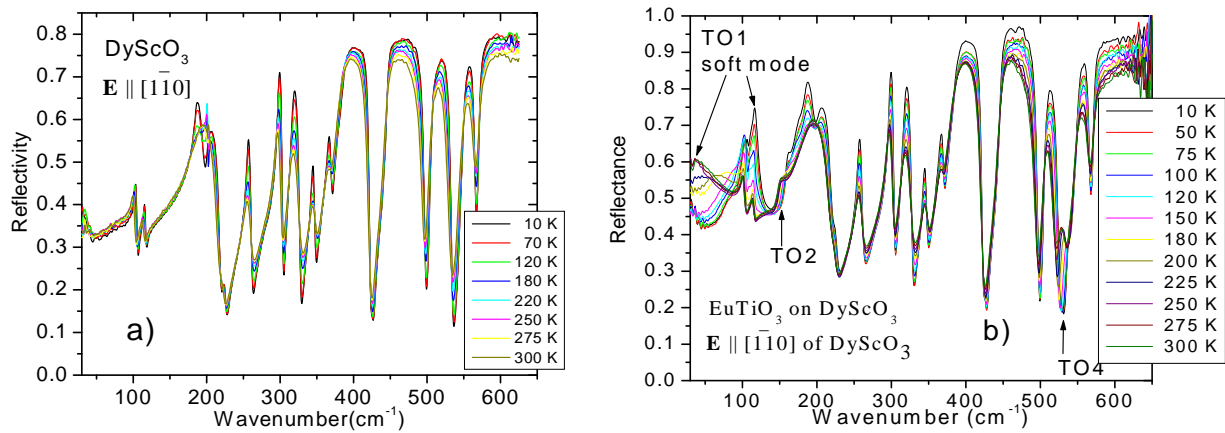


Fig.4.21. Far infrared reflectivity spectra of a) bare (110) DSO substrate; b) of a 100 nm thick ETO thin films deposited on (110) DSO. The spectra were taken for  $\mathbf{E} \parallel [110]$  polarization. The polar phonons in the thin film are marked by arrows.

FIR spectra of a bare (110) DSO substrate as well as of the 100 nm thick ETO film are shown in Fig.4.21. Reflectance bands (polar phonons) from the substrate dominate in the ETO/DSO spectra, but the polar phonons from the thin films are also clearly distinguishable (see Fig.4.21b). Considering the opacity of the substrate, its reflectivity spectra were fit with the factorized form of the dielectric function (Eq. 3.6).<sup>149</sup> The resultant parameters from the substrate were used to fit the reflectance spectra of the ETO/DSO with a sum of harmonic oscillators using software for evaluation of the dielectric function of a two-slab system.<sup>96</sup> The same behavior was observed in second polarization of the IR beam i.e  $\mathbf{E} \parallel [001]$  (orientation of DSO substrate). The same models were used for fitting of the bare substrate and ETO film measured in polarization  $\mathbf{E} \parallel [001]$  of DSO (see Fig.4.22).

At room temperature the TO1 SM occurs at a frequency nearly three times lower than in bulk ETO, which is caused by the proximity of the strain-induced FE PT temperature. Lattice instability and the FE PT are demonstrated by the minimum in the SM frequency at 250 K. The SM anomaly is responsible for the peak at 250 K in the temperature dependence of the static relative permittivity, if it is calculated from contributions of all of the phonons. The temperature dependence of static permittivity shows a maximum at 250 K in both polarizations:  $\mathbf{E} \parallel [110]$  and  $\mathbf{E} \parallel [001]$ . (Fig.4.23b)

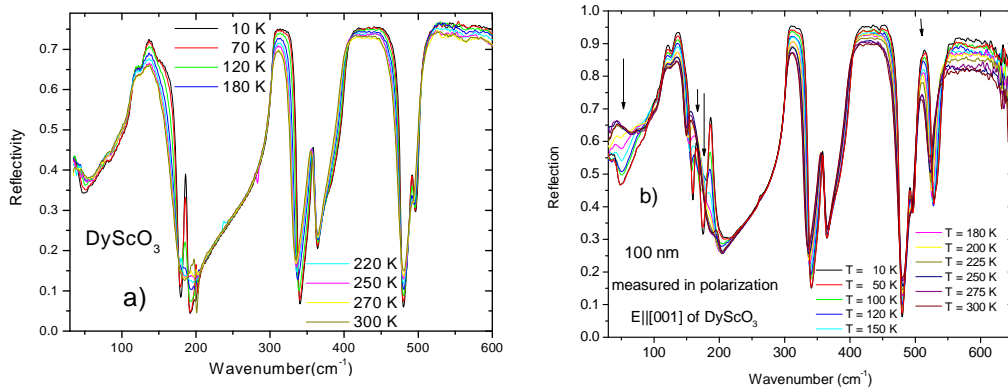


Fig. 4.22.  $E_{||[001]}$  polarized FIR reflectivity spectra of a) bare DSO substrate; b) of a 100 nm thick ETO thin films deposited on DSO substrate. The polar phonons resolved in the film are marked by arrows.

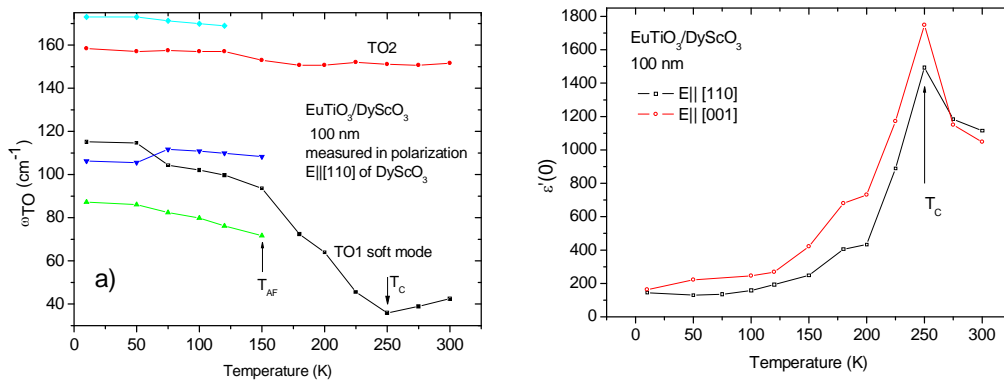


Fig.4.23. a) Temperature dependence of the polar phonon frequencies below  $200 \text{ cm}^{-1}$  obtained by fitting the reflectance spectra measured in polarization  $E_{||[110]}$ . The minimum in the SM frequency seen near 250 K as well as the appearance of new modes below 150 K provide evidence of FE ( $T_C$ ) and AFD ( $T_{AFD}$ ) PTs, respectively; b) temperature dependence of static permittivity in the thin film obtained from the phonon spectra.

The temperature dependences of resulting phonon frequencies seen in  $E_{||[110]}$  polarized spectra are plotted in the Fig. 4.23a) Below 250 K, the SM frequency hardens remarkably on cooling. Also, two new modes are activated below 150 K in the vicinity of the SM frequency. These modes should be structural SMs activated from the BZ boundary. They can be only Raman active in a non polar AFD phase<sup>150</sup>, but they also become IR active if this phase is simultaneously non centrosymmetric, which is satisfied when ETO becomes FE. Similar activation of the structural SM in the FIR spectra as well as a minimum of the SM frequency at  $T_C=270 \text{ K}$  was

also observed in strained STO films grown with the same biaxial tensile strain state (i.e. STO/DSO).<sup>151</sup>

Splitting of TO2 (near 160  $\text{cm}^{-1}$ ) and TO4 (near 525  $\text{cm}^{-1}$ ) in ETO/DSO is allowed at all temperatures below  $T_c \approx 250$  K, but it was distinguished in  $\mathbf{E}||[110]$  polarized spectra only below 180 K for TO4 and 120 K for TO2, probably due to the low intensities of these modes. These splittings were resolved in the  $\mathbf{E}||[001]$  polarized spectra, see Fig. 4.24. Nevertheless, the activation of two new modes observed near the SM in  $\mathbf{E}||[001]$  polarization was not seen due to lower sensitivity in this frequency range. This was caused by existence of a strong polar phonon in  $\mathbf{E}||[110]$  polarized spectra of the DSO substrate.

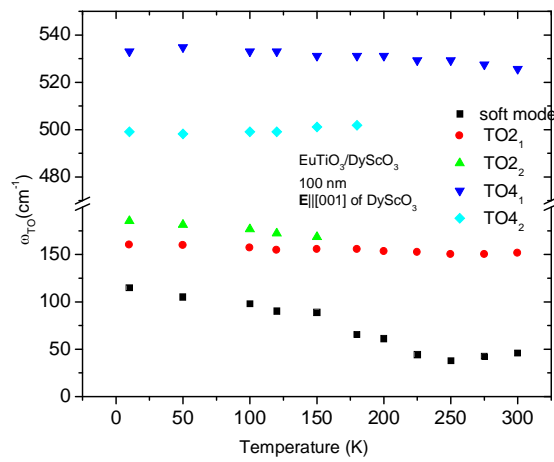


Fig.4.24. Temperature dependence of polar mode frequencies resolved in  $\mathbf{E}||[001]$  polarized spectra of ETO /DSO. In contrast to Fig. 4.23a), there is very well seen the splitting of TO2 and TO4 modes due to better sensitivity in this spectral range given by spectral shape of the substrate spectra.

It is worth noting that the fit of the FIR reflectance spectra required imaginary coupling of the TO1 and TO2 modes in the FE phase. In such case the permittivity has the form of Eq.3.15. In spite of the real coupling the imaginary coupling does not shift the “dressed” phonon frequencies, but only changes the shape of dielectric dispersion near the both coupled phonon frequencies, which has an influence on the shape of reflection bands. The complex permittivity spectra obtained from the IR fit of  $\mathbf{E}||[110]$  polarized spectra are plotted in Fig.4.25. The first maximum in  $\varepsilon''(\omega)$  spectra roughly corresponds to  $\omega_{TO1}$  i.e. the SM frequency. Aforementioned peak of  $\varepsilon'(T)$  seen near 250 K in Fig. 4.23 is good evidence for FE PT in tensile strained ETO film.

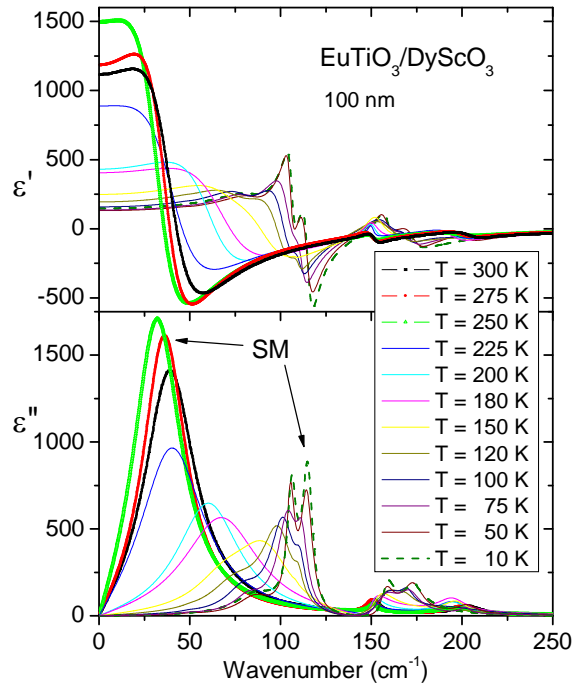


Fig.4.25. Complex dielectric spectra of ETO/DSO obtained from the fits of  $\mathbf{E}||[110]$  polarized FIR spectra.

An additional test for ferroelectricity in this film was made in our collaborating lab at Penn State University using measurements of a second harmonic generation (SHG). Materials lacking inversion symmetry must exhibit SHG and FEs really lack inversion symmetry. SHG exhibits a strong signal below 250 K (see Fig.4.26), i.e. below the temperature where the peak in  $\epsilon'(T)$  was observed. It clearly supports the FE nature of the PT. On the other hand no SHG signal was detected on compressively strained ETO film deposited on (001) LSAT substrate as well as on unstrained ETO film deposited on STO. This behavior suggests that these ETO thin films are not FE.

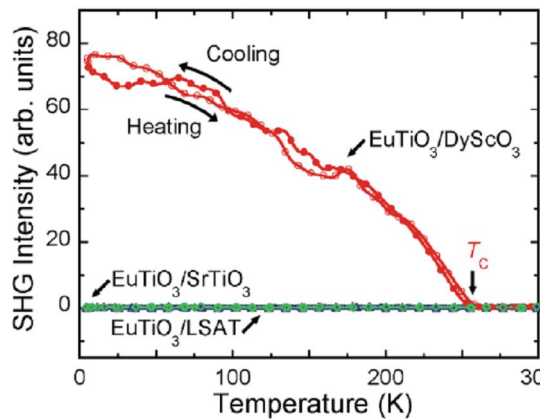


Fig.4.26. Temperature dependence of the SHG signal in ETO thin films deposited on DSO, STO on LSAT substrates.

In order to prove the theoretical prediction that the thin film becomes FM under a biaxial tensile strain, the magnetic properties were investigated in our collaborating lab at Yale University. Testing for ferromagnetism in strained ETO film on DSO is complicated due to the large PM response of the DSO substrate. If a SQUID magnetometer is used at typical magnetic field, the PM response of the thick substrate swamps the signal from the strained ETO film. In such conditions, both magneto-optic Kerr effect (MOKE) and SQUID magnetometry were investigated. For MOKE measurements the magnetic field was applied in the plane of the sample and the probe light was polarized also in-the plane of the sample. The difference in polarization angle between the incident and reflected beam is the Kerr angle. Using the MOKE measurements a quantitative evaluation of coercivity as well as the FM hysteresis loop can be revealed.

In the Fig.4.27a) are presented the MOKE responses for three ETO thin films. Only ETO on DSO exhibits a clear ferromagnetic hysteresis loop with sharp switching to full saturation. The temperature dependence of the MOKE have shown that the ferromagnetic Currie temperature of the +1.1% strained ETO thin has  $T_c = 4.24 \pm 0.02K$  which is slightly lower than the Néel temperature 5.5 K of unstrained ETO (see Fig.4.27b). The SQUID measurement will not be presented here due to the lack of space, but it revealed the same Currie temperature as the MOKE experiment. For details see electronic supplement of Ref.144.

We have proved above, that originally AFM and PE ETO can be changed in strained thin films to strong FM and FE due to strong spin-lattice coupling. It shows new route for preparation of novel multiferroic systems with a strong ME coupling, which can be used in future memories.

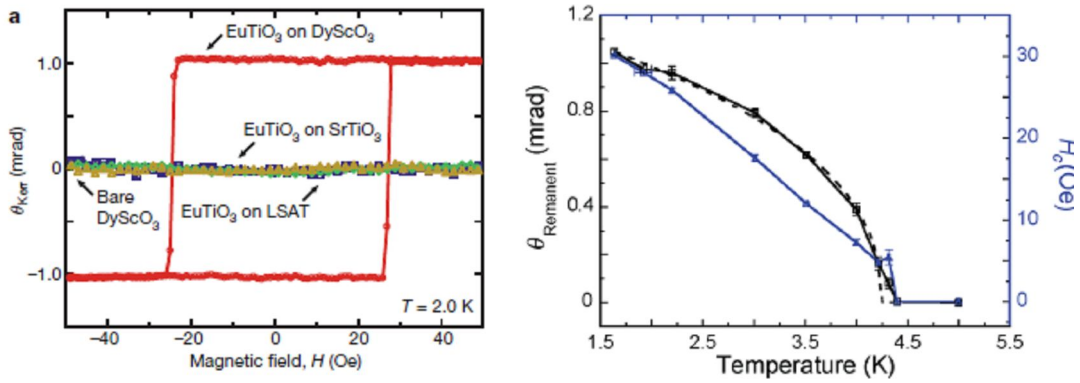


Fig.4.27.a) MOKE measurements at 2 K of ETO on DSO (red), ETO on STO (blue), ETO on LSAT (green) and bare DSO substrate (gold); b) Temperature dependence of remnant Kerr angle and coercivity in ETO/DSO-(after Ref.144)

One can ask, what is the evidence for strong ferroelectricity in strained ETO thin films? Unfortunately, we could not measure directly the FE polarization due to electric leakage of the ETO film. Nevertheless, strong FEs are proper FEs, having polarization as their order parameter, with high PE-to-FE PT temperatures  $T_C$ . Such FEs are manifested by a high peak at  $T_C$  in  $\epsilon'(T)$ , signifying that ferroelectricity is driven by the polar SM. Our measurements of strained ETO demonstrate both of these characteristics (shown in Figs 4.23). It led us to conclude that strained ETO is a strong FE. In contrast, all well-established prior single-phase FE FMs of type II are improper or pseudoproper FEs (that is, with weak ferroelectricity resulting in minuscule  $P_S$ ).<sup>152</sup> The magnitude of  $P_S$  of our strained ETO films cannot be directly determined from SHG but it can be estimated as follows. In their classic work, Abrahams, Kurtz, and Jamieson<sup>153</sup> established a correlation between  $P_S$  and  $T_C$  for displacive FEs. By studying numerous displacive FEs they found<sup>153</sup>

$$T_C = (2.0 \pm 0.09) \times 10^4 (\Delta z)^2$$

and

$$P_S = (258 \pm 9) \Delta z$$

where  $T_C$  is the PE to FE PT temperature in K,  $\Delta z$  is the atomic displacement of the homopolar metal atom in Å and  $P_S$  is the spontaneous polarization of the FE in  $\mu Ccm^{-2}$ . Combining these equations to eliminate the atomic displacements allows to estimate  $P_S$  from  $T_C$  in displacive FEs. The huge anomaly of the SM near  $T_C$  shows that strained ETO film is displacive FE, making



mentioned correlation applicable. Finally, our calculation yields that  $P_S = 29 \pm 2 \mu\text{Ccm}^{-2}$ .<sup>154</sup> This rough estimation is consistent with the Fennie's theoretical calculation giving  $P_S=21 \mu\text{Ccm}^{-2}$ . Such  $P_S$  is comparable to strong FE  $\text{BaTiO}_3$  and it is three or four orders of magnitude higher than  $P_S$  in spin-induced FEs (type-II multiferroics).

#### 4.4.2 Compressively strained $\text{EuTiO}_3$ thin films

In the case of compressively strained ETO thin films the situation is a bit complicated. First problem is that the strain induced FE polarization should be theoretically oriented out of film plane and the electric field component of IR beam testing the permittivity lies in the film. This makes impossible to study dielectric response (i.e. polar phonons) polarized in the direction of  $P_S$ . The second problem is the lack of an appropriate substrate. It is necessary a large compressive biaxial strain to evoke a strong FE and FM phase.

In order to analyze the IR properties of ETO in compressively strained thin films it was chosen to use the (001) LAO, (001) LSAT –mentioned a bit above - and (110) NGO substrates (Fig.4.28). Each thin film was measured using IR spectroscopy in order to investigate the phonon and complex permittivity behavior down to liquid He temperatures.

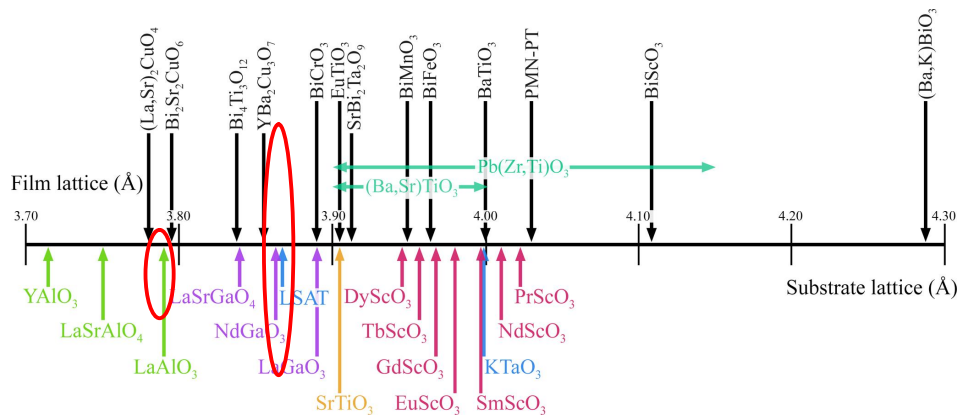


Fig.4.28. The pseudotetragonal or pseudocubic a-axis lattice constants of some perovskites of current interest (above the number line) and some of the perovskite and perovskite-related substrates that are available commercially (below the number line). Lattice constants of bulk ETO as well as our used substrates are marked by ellipse.<sup>155</sup>

#### 4.4.2.1 EuTiO<sub>3</sub>/LSAT

Films of two thicknesses 22 nm and 42 nm were studied. X-ray diffraction measurements (not presented here) showed that the film is commensurate with the substrate. The 42 nm thin film was slightly relaxed, but the 22 nm thin film was fully (-0.9%) compressively strained, i.e. its XRD exhibited the same in-plane lattice parameter (3.87 Å) as the substrate.

Compressive strain should induce in ETO films similarly to STO films a polarization oriented out of the film plane. So the permittivity  $\epsilon_c$  should exhibit maximum at  $T_C$  due to softening of the  $A_{2u}$  component of the TO1 phonon active in  $\mathbf{E}||c$  polarized IR spectra. Even if the strain in ETO/LSAT is not sufficient for inducing the FE phase, the  $\epsilon_c$  should be higher than  $\epsilon_a$  and should exhibit stronger temperature dependence than  $\epsilon_a$ . Unfortunately, IR spectra can investigate only  $\epsilon_a$  response, but anyway, if there will occur some structural or FE PT, it should be indicated in IR spectra by appearance of new polar phonons.

IR reflectance spectra of 42 nm ETO thin film plotted at various temperatures are shown in Fig.4.29. Comparison of the spectra with those of bare LSAT substrate allows distinguishing the three TO phonons of the thin film. In the picture the phonons are marked by arrows. The highest frequency phonon is marked by TO4 since the TO3 phonon is silent. TO1 and TO2 phonon frequencies exhibit softening on cooling, which is better seen in inset of Fig. 4.29.

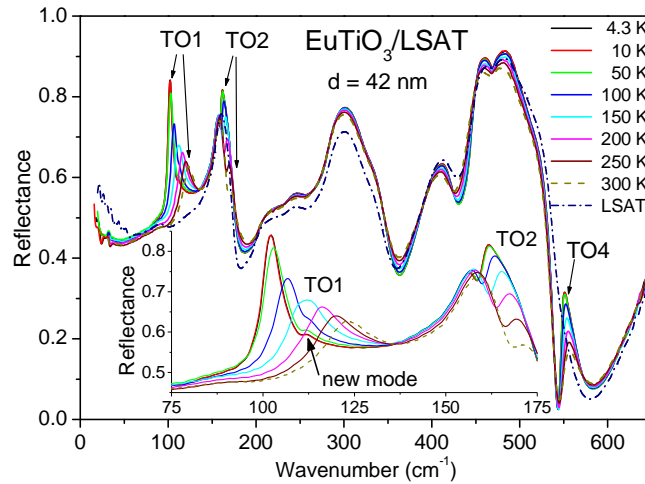


Fig.4.29. Temperature dependence of the IR reflectance of 42 nm thick ETO thin film deposited on the LSAT substrate. Room temperature reflectivity of pure LSAT substrate is also plotted for comparison (dashed-dotted line). Phonons from the thin films are marked. Inset shows the enlarged low frequency part of reflectance spectra, where the softening of TO1 and TO2 phonons are seen.

Moreover, a new weak mode appears near  $112\text{ cm}^{-1}$  below  $100\text{ K}$ . Such a splitting of the TO1 mode could be a signature of change of crystal symmetry, but it could arise also from partially relaxed strain in the  $42\text{ nm}$  film revealed by XRD analysis. Therefore we measured also  $22\text{ nm}$  fully compressively strained thin film. Due to the smaller film thickness, the intensity of the TO1 phonon is lower in IR spectra, but one can clearly see the TO1 mode splitting already below  $150\text{ K}$  (see Fig. 4.30).

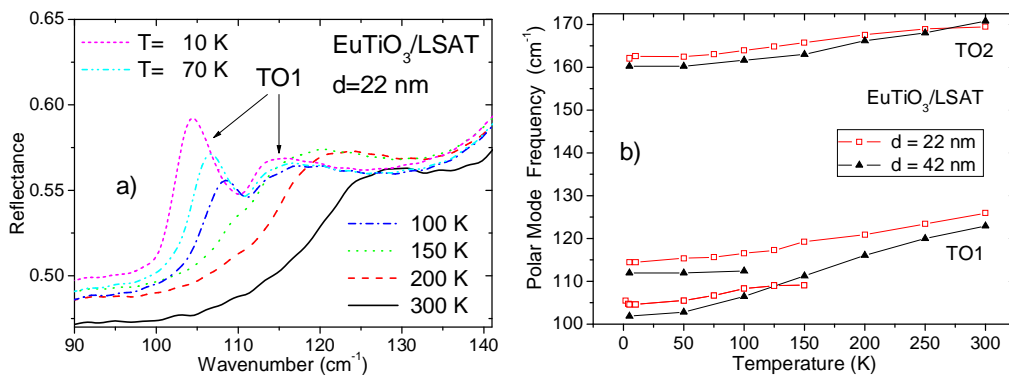


Fig.4.30 a) Temperature dependence of the low- frequency IR reflectance of fully strained  $22\text{ nm}$  thick ETO thin films deposited on a LSAT substrate. Remarkable TO1 phonon softening and its splitting below  $150\text{ K}$  is clearly seen; b) Temperature dependence of the phonon frequencies in the ETO thin films of two thicknesses  $42\text{ nm}$  and  $22\text{ nm}$  below  $170\text{ cm}^{-1}$ . Remarkable stiffening of TO1 and TO2 phonons frequencies in the more strained  $22\text{ nm}$  thin films is seen. New mode in  $22\text{ nm}$  film activates near the TO1 mode by  $50\text{ K}$  higher than in the thicker film.

Fig. 4.30 a) shows temperature dependence of the polar phonon frequencies below  $170\text{ cm}^{-1}$  obtained from the reflectance fits of both films. At  $10\text{ K}$  the  $F_{1u}$  symmetry TO phonon frequencies were  $83, 151$  and  $533\text{ cm}^{-1}$  in bulk ceramic, while  $22\text{ nm}$  film shows  $E_u$  symmetry phonons at  $115, 162, 551\text{ cm}^{-1}$  and additional new mode at  $105\text{ cm}^{-1}$ . One can see a huge phonon frequency stiffening in the films due to the compressive strain. Notice also that the phonon frequencies are higher in the  $22\text{ nm}$  film than in the  $42\text{ nm}$  film one due to the higher strain in the former case (see Fig.4.30 b).

Complex permittivity spectra evaluated from the IR reflectance spectra are shown in the Fig.4.31. Stiffening of all polar phonons is responsible for a lower static in plane permittivity ( $\epsilon'_a < 250$ ) in the films compared with the bulk samples. At  $10\text{ K}$  the static permittivity reaches

value 146 while in single crystal it is  $\epsilon_0 = 405$ . TO1 phonon is the most sensitive to the strain. It has  $F_{1u}$  symmetry in the bulk cubic ceramics. In the compressively strained tetragonal films, only the harder  $E_u$  component of the SM polarized in the film plane ( $\mathbf{E} \perp [001]$ ) is seen while the softer  $A_{2u}$  component should be IR active in  $\mathbf{E} \parallel [001]$  spectra, which are not technically accessible in the experiment. One can expect that the static out-of-plane permittivity  $\epsilon_c$  will be higher in ETO/LSAT than in the bulk ETO crystal due to the strain induced softening of the  $A_{2u}$  component of the TO1 mode.

Stiffening of the  $E_u$  component of the SM was reported also in compressively strained STO film deposited on LSAT.<sup>156</sup> The bulk STO has exactly the same lattice parameter and  $Pm\bar{3}m$  crystal structure as ETO, therefore the strain in both films deposited on LSAT is expected to be the same and the IR reflectance spectra are also similar. However, no phonon splitting on cooling was observed in STO/LSAT although the FE PT was theoretically predicted in these compressively strained films. The reason could be a larger thickness of the investigated STO films (49 and 107 nm). In this case the SM reflection band is broader than in the case of ETO/LSAT, so that the small splitting might not be resolved due to the overlapping of both reflection bands. Note that the SM splitting in ETO/LSAT is well resolved in the fully strained 22 nm thin film, but hardly in the slightly relaxed films with thickness 42 nm.

The newly activated mode near the TO1 phonon frequency can have various origins. Three possibilities are available: 1) the new mode is due to the FE PT, 2) the activation of new mode is due to short range magnetic order which breaks locally the symmetry and activates the AFD PT, and finally the last possibility is that 3) the new mode is due to the presence of polar cluster which allows the IR activation of the BZ boundary mode after an AFD PT.

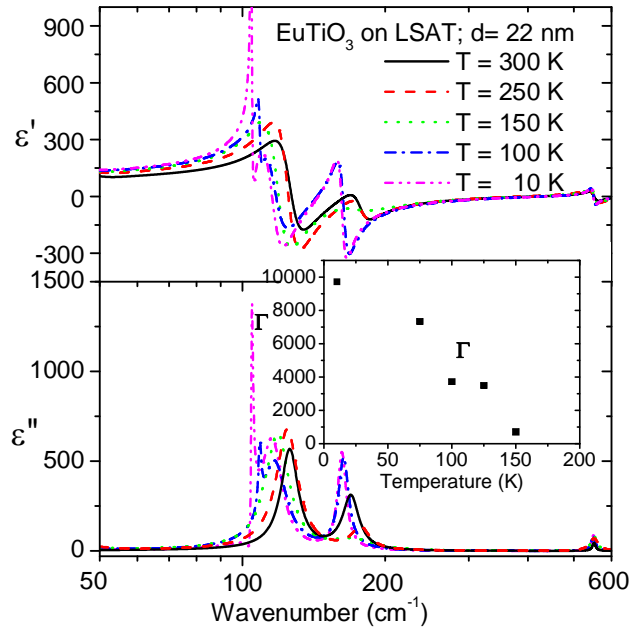


Fig.4.31. Complex dielectric function spectra of 22 nm ETO thin film calculated at various temperatures from the reflectance spectra. Inset shows the temperature dependence of imaginary coupling constant between the split components of TO1 mode

The first possibility fails because the SHG does not exhibit any signal in ETO/LSAT (see Fig.4.26) and theoretical predictions suggest that the strain should be larger than -1.1% to obtain ferroelectricity. The possibility that the new mode is due to the short range magnetic order fails also because Néel temperature is around 5.4 K and the phonon splitting occurs already at 150 K. Nevertheless, the newly activated mode could appear due to AFD PT which can occur in ETO on LSAT. An AFD PT is connected with doubling of primitive unit cell due to oxygen octahedral tilting. We have proved above that the bulk ETO undergoes the AFD PT already close to room temperature. It can happen that the AFD transition is suppressed with the compressive strain down to 150 K. Nevertheless, the IR activation of the mode from the BZ boundary requires not only AFD transition, but also a non-centrosymmetric phase. We know from SHG measurement, that ETO/LSAT is centrosymmetric down to liquid He temperatures (see Fig.4.26). Nevertheless, the IR spectroscopy is highly sensitive on local order, and it can happen that the centre of symmetry is locally broken due to presence of polar clusters. Similar effect is well known in relaxor FEs.<sup>131</sup>

ETO/LSAT is probably not relaxor FEs, but Rushchanskii and Lezaic<sup>135</sup> have proposed new mechanism of breaking of central symmetry due to presence of oxygen vacancies (see

Fig.4.32). In ideal perovskite structure without octahedra tilting local environment around the vacancy is antipolar: two neighboring Ti atoms are equally displaced in different directions. In structure which allows oxygen octahedra tilting (i.e. in AFD phase), the displacements of Ti atoms are antipolar in one direction, but with uncompensated dipoles in orthogonal directions. These dipoles lay in tetragonal plane, i.e. they can influence the  $\epsilon_a$  spectra. Apparently, this mode can be also a local vibration mode caused by oxygen vacancy, therefore the observed peak is very sharp in Fig. 4.31

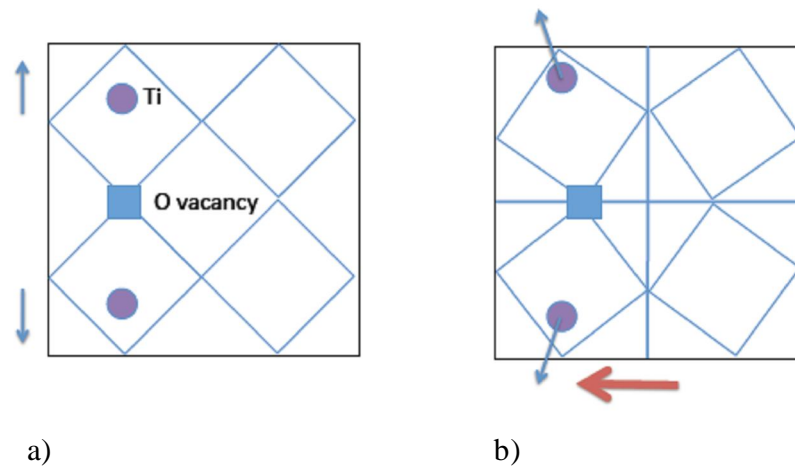


Fig.4.32. A sketch of the perovskite structure which a) does not allow the oxygen octahedral tilting and b) the structure which allows the oxygen octahedral tilting against the Ti atoms. Direction of local polarization is marked by red arrow.

According to this explanation the new mode, which activates in IR spectra around  $105\text{ cm}^{-1}$ , is a phonon originating from the BZ boundary, which is activated in IR spectra due to locally broken centre of symmetry and due to folding of BZ.

The sharp TO1 reflectance band in compressively strained ETO films appears to be more promising for investigation of its behavior with magnetic field, although the expected frequency shift is much lower ( $<3\text{ cm}^{-1}$ ) than in the bulk crystal due to the SM stiffening by strain. We really observed  $2\text{ cm}^{-1}$  shift down of the lower component of the TO1 SM frequency with magnetic field (Fig.4.33).

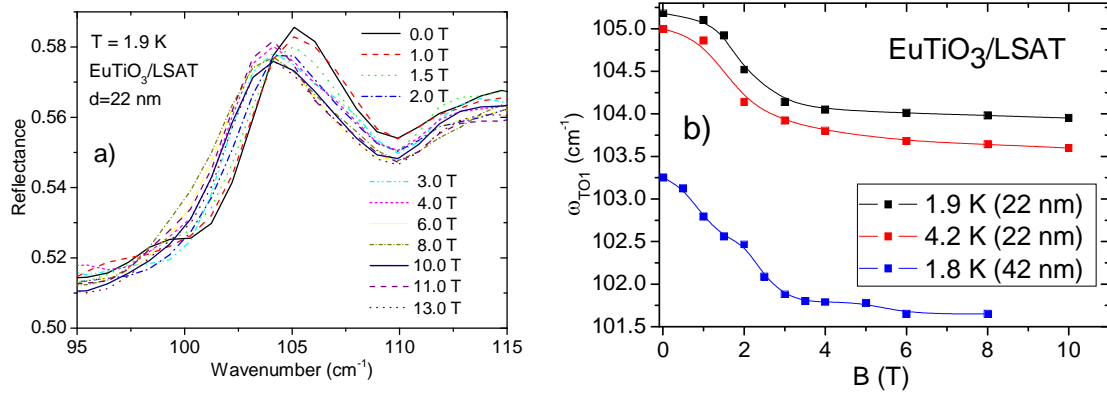


Fig.4.33. a) IR reflectance spectra of 22 nm thin film at 1.9 K taken at various magnetic fields. The shift of phonon frequency is clearly seen; b) Magnetic field dependence of the lowest-energy phonon frequency obtained from the fits of IR reflectance of both films at various temperatures below  $T_N$

The phonon frequency changes were similar and reproducible in both thin films (see Fig. 4.33b) and the TO1 frequency shifts were determined with a high accuracy of  $0.1 \text{ cm}^{-1}$  due to the sharp feature of the reflectance band. The higher frequency component of the TO1 reflectance band was weaker and broader; therefore its change with  $B$  was not determined. Magnetocapacitance effect, i.e. the relative change of the static permittivity with magnetic field  $B$  ( $\Delta\varepsilon'(B)/\varepsilon'(0)$ ) obtained from the fits of reflectance is plotted in Fig. 4.34. As expected, one can see almost three times smaller change of  $\Delta\varepsilon'(B)/\varepsilon'(0)$  in the thinner film than in the single crystal.

The change of  $\Delta\varepsilon'(B)/\varepsilon'(0)$  appears to be larger in the thicker film, but it is probably caused by relatively large uncertainty of  $\Delta\varepsilon$  determination due to limited accuracy of the absolute value of IR reflectance. On other hand, as expected and known from bulk ceramics, the magnetocapacitance effect is larger at 1.9 K than at 4.2 K, because the effect becomes stronger on cooling below Néel temperature.<sup>122</sup>

The first principle calculation predicts TO1 phonon frequency of ETO/LSAT near  $101 \text{ cm}^{-1}$  at 2 K and its softening by  $3 \text{ cm}^{-1}$  in the field of several Tesla. It corresponds rather well to our experimental data. In this way it is confirmed that the magnetocapacitance effect in ETO is due to the change of the soft phonon frequency with magnetic field. It should be stressed that our observation of tuning of polar phonon frequency with magnetic field is rather unique, we know only two such examples in the literature – see Ref.[157, 158]. On the other hand, tuning of IR-active phonons with external electric field is easier due to their polar character. (e.g. Ref.159)

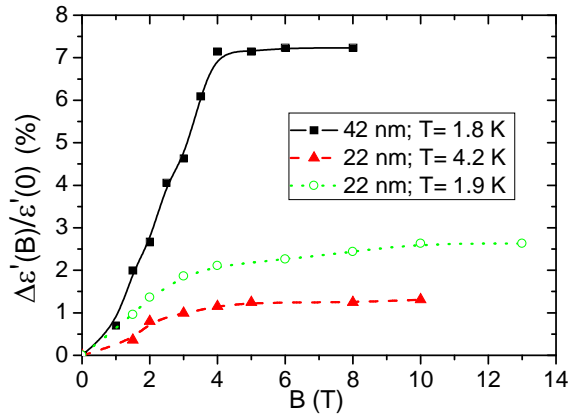


Fig.4.34. Magnetic field dependence of the relative changes of static permittivity obtained from the fits of the IR reflectance of the ETO/LSAT films of two thicknesses.

The magnetic properties of ETO film on LSAT were also investigated. Magnetization curves taken at various external magnetic fields reveal  $T_N=6.3$  K. It means that -0.9% compressive strain in the thin film enhances  $T_N$  by 1.0 K because the coupling of spins localized at  $4f$  levels of Eu cations increases with the reducing lattice parameter in the compressively strained thin films. Note that on the other hand +1.1% tensile strain in ETO/DSO reduces the ferromagnetic order below 4.2 K.<sup>144</sup>

#### 4.4.2.2 *EuTiO<sub>3</sub>/LaAlO<sub>3</sub>*

In order to see if other compressively strained ETO thin films have a similar phonon and structural behavior as ETO on LSAT, another thin film was investigated. The ETO film on (001) LAO was analyzed in the same way as ETO on LSAT. The XRD patterns were obtained in order to reveal the structural perfection and quality of the strain in the film. As Fig 4.35 shows, an  $\theta$ -2 $\theta$  scan shows phase pure, epitaxial (100)-oriented ETO film. The  $100$  reflections of the film are very well seen, but substrate  $100$  reflections have much higher intensities. The theoretical lattice mismatch between lattice parameter of bulk ETO and substrate is approximately -2.9 %, however deep analysis of XRD data shows the strain in our ETO/LAO is only around -0.95%. Since ETO film on LAO has the thickness of 100 nm, the strain of the film exhibited some relaxation. It is also demonstrated in Fig.4.35b), where the reciprocal space map shows that the peak of the film is not on the circle line (fully relaxation line). Average lattice constants of the thin film are  $a=3.868$  Å and  $c=3.921$  Å. Note that bulk ETO has  $a=3.905$  Å.



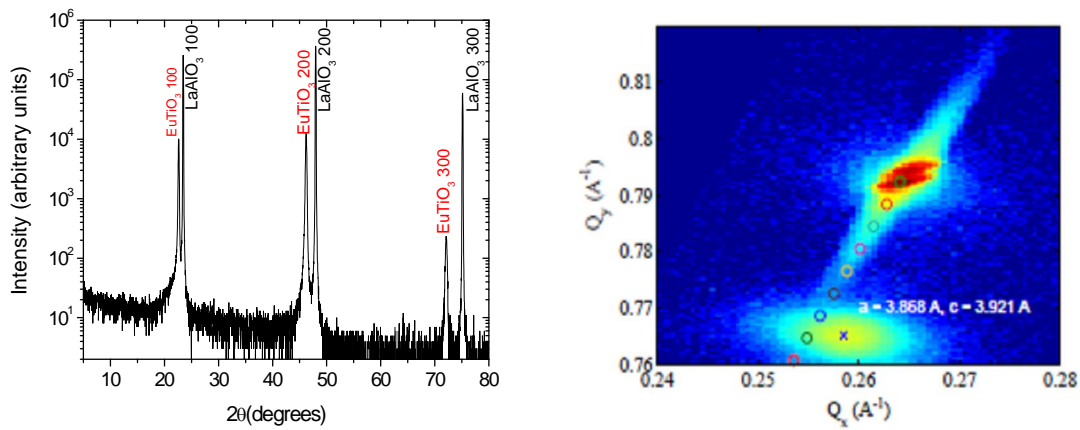


Fig.4.35. a) XRD patterns of the ETO/LAO b) Reciprocal space map of ETO/LAO. Circles denote the full relaxation line

Fig.4.36 shows the IR reflectivities of the bare LAO substrate and ETO film on LAO at two selected temperatures 10 K and 300 K. The IR spectra of the thin film are compared with the substrate to mark out the phonons from the film. The optical phonons coming from the thin ETO film are indicated by arrows.

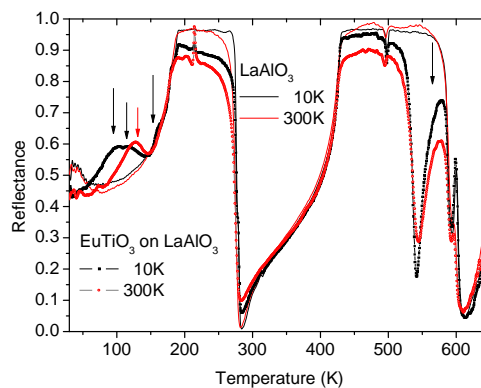


Fig.4.36. Reflectivity spectra of LAO substrate and reflectance of 100 nm thick ETO film on LAO substrate. Spectra are shown at 300 and 10 K.

In Fig. 4.37 the temperature dependence of TO phonon frequencies in ETO/LAO is shown. At room temperature, the IR reflectance spectra exhibit four modes: single component of the TO1 mode, two components of the TO2 mode and one component of the TO4 mode. In Fig. 4.37 also the temperature dependence of TO1 phonon frequency in ETO ceramics is plotted. The presence

of compressive strain stiffens the eigenfrequency of the TO1 mode. Similar effect was observed in ETO/LSAT.

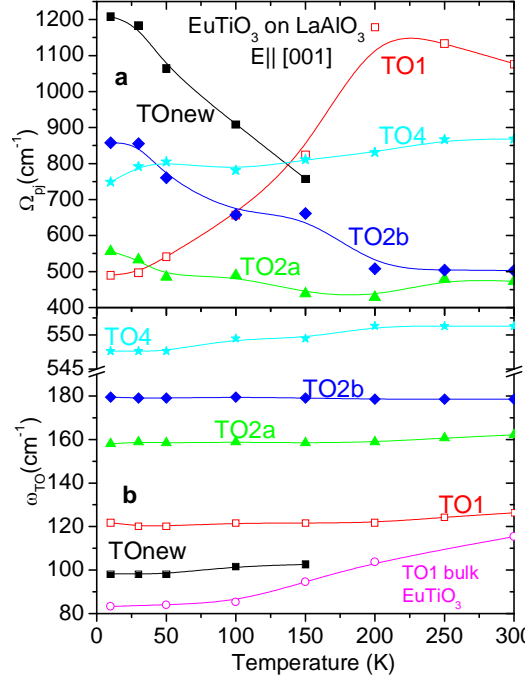


FIG. 4.37. Temperature dependence of a) plasma frequencies  $\Omega_{pi}$  and b) polar phonon frequencies in ETO film deposited on LAO substrate.

The TO1 phonon exhibits a splitting into two components below 150 K with a new component seen near  $100 \text{ cm}^{-1}$  (Fig. 4.37(b)). However, TO2 mode is already split at room temperature due to the fact that ETO/LAO is partially relaxed. Nevertheless, the phonon behavior of TO1 mode has similar behavior as in fully -0.9% compressively strained ETO/LSAT. Only the eigenfrequency of the newly activated mode (marked as TOnew) seen below 150 K is slightly ( $\sim 5 \text{ cm}^{-1}$ ) lower than eigenfrequency of the new mode in ETO/LSAT. The reason could be that the strain in ETO/LAO is partially relaxed.

In such conditions, we proceed further with analyzing the strength of oscillators calculating the plasma frequency (Eq.4.3). All these parameters were obtained by fitting the IR spectra. One can see that plasma frequency of TO1 component decreases on cooling due to splitting of it. The newly activated mode (marked as TO1new) appears at 150 K and its plasma frequency increases on cooling. Plasma frequencies  $\Omega_{pi}$  of other modes slightly increase on cooling, but sum of  $\Omega_{pi}^2$  is almost temperature independent within accuracy of our experiment,

which satisfies the sum rule i.e.  $\sum_j \omega_{TOj}^2 \Delta \epsilon_j = const.$  The origin of the newly activated mode could be similar as in the case of ETO on LSAT so that these two thin films deposited on different substrates have similar behavior. In both films probably occurs AFD PT near 150 K.

We tried to measure also the change of phonon frequencies with magnetic field in ETO on LAO. Unfortunately no shift with magnetic field was observed. The problem was that the sensitivity of such experiment was much lower than in the case of ETO on LSAT, because the TO1 reflection band is much broader in the case of ETO/LAO than in ETO/LSAT.

#### 4.4.2.3 *EuTiO<sub>3</sub>/NdGaO<sub>3</sub>*

The IR reflectivity spectra of 200 nm thick ETO film on NGO were measured in polarized IR radiation because the bare NGO substrate is anisotropic. From that reason two types of IR spectra were obtained with polarization  $\mathbf{E}||[001]$  and  $\mathbf{E}||[110]$  with regards to orientation of orthorhombic NGO substrate.

In order to characterize the phonon behavior, we again measured polarized IR reflectance spectra at various temperatures down to 10 K (see. Fig.4.38a). The NGO substrate response in the IR range was reported in details elsewhere.<sup>160</sup> The IR spectra are complicated by the  $4f$  electron absorption from Nd, which appears in substrate below 100 K as a sharp resonance near  $100 \text{ cm}^{-1}$  (see Fig.4.38a). The analysis of IR spectra was performed in similar way as in previous thin films.

Figs. 4.38c) d) reveal the temperature dependence of TO phonon frequencies in ETO/NGO. As it can be seen the film (see Fig.4.38 a) and b) shows 5 IR active modes at 300 K in both polarizations ( $\mathbf{E}||[110]$  and  $\mathbf{E}||[001]$ ). The TO4 mode is temperature independent, therefore it is not plotted in the Figs.4.38 c) and d). However, in bulk ETO, there are only three IR active phonons allowed. In bulk ETO, TO1 mode softens from  $115 \text{ cm}^{-1}$  at 300 K down to  $83 \text{ cm}^{-1}$  at 10 K.<sup>128</sup> But in case of ETO/NGO, the TO1 mode is split already at room temperature into two components (seen in both polarized spectra). This behavior supports the idea that we have two different values of strain i.e. two values of the  $c$  (and  $a$ ) lattice constants. In  $\mathbf{E}||[110]$  polarized spectra, the two TO1 modes are seen around  $113 \text{ cm}^{-1}$  (marked as TO1b) and  $95 \text{ cm}^{-1}$  (TO1a). Both modes soften on cooling by  $5\text{-}10 \text{ cm}^{-1}$ . It seems that the TO1a component corresponds to the relaxed part of the thin film on the surface of the film (if has similar frequency as in the bulk), while the second TO1b component (with higher frequency) corresponds to the TO1 with

compressive strain. The dielectric strength  $\Delta\epsilon$  of the TO1a mode is higher than dielectric strength of TO1b, which demonstrates that larger part of the ETO film deposited on NGO substrate is relaxed.

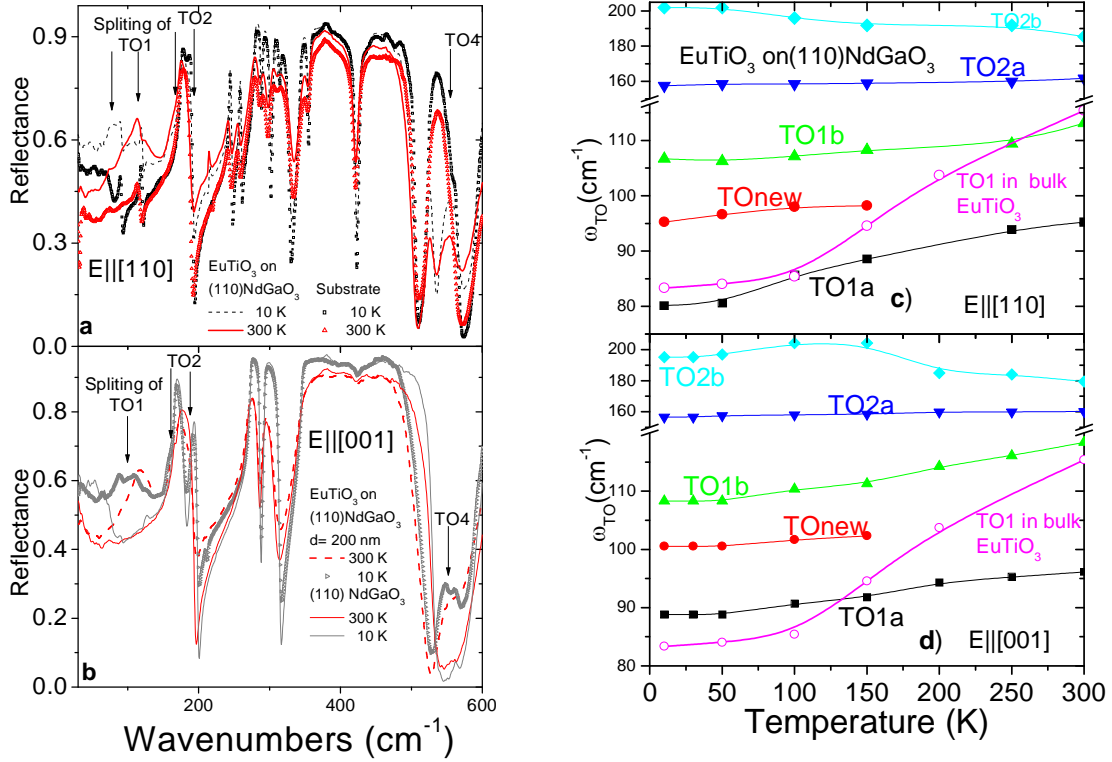


Fig.4.38. Polarized IR reflectance spectra of NGO and ETO/NGO measured at 300 K and 10 K with polarization a)  $\mathbf{E}||[110]$  and b)  $\mathbf{E}||[001]$ ; Temperature dependence of polar phonon frequencies in ETO on NGO observed in polarizations c)  $\mathbf{E}||[110]$  and d)  $\mathbf{E}||[001]$ . In both pictures the temperature dependence of polar SM in bulk ETO is added.

Moreover, a new mode appears between TO1a and TO1b frequency below 150 K. The same behavior was observed in  $\mathbf{E}||[001]$  polarized spectra. As regards the higher-frequency modes, only TO2 is split already at room temperature in two components (Fig.4.38c d)). The TO4 mode (near  $\sim 550 \text{ cm}^{-1}$ ) was barely seen in the spectra due to small damping and low dielectric contribution. It is important to note that the newly activated mode has similar frequency  $\sim 100 \text{ cm}^{-1}$  as the TOnew mode seen in ETO/LAO and ETO/LSAT. This means that the sample probably again exhibits an AFD PT and the mode is activated from BZ boundary due to polar defects in the lattice.

The XRD patterns revealed -0.3% compressive in-plane strain with  $a= 3.893 \text{ \AA}$  and  $c=3.909 \text{ \AA}$ . Detailed analysis of XRD patterns measured and evaluated by O. Pacheroová and X. Martí revealed second  $c$ -parameter with value of  $3.896 \text{ \AA}$ . Its XRD spot is very weak; it means that only 2% volume of the film has such  $c$  parameter which is even smaller than lattice parameter in ETO bulk. This is probable surface layer of the film and its  $c$ -parameter is smaller due to vacancies near surface. On other hand it means that the  $a$ -lattice parameter near the surface of the film must be larger than in the bulk (tensile strain!). However, this situation is not yet clear, because very recent new and more sensitive synchrotron measurements (X. Martí) revealed only one lattice constant in the  $c$  direction. The sample thickness is 200 nm and therefore the strain relaxation is higher than in the previous samples although the theoretical possible strain could be -1.0 %. From that reason the real compressive strain is only -0.3%.

The static permittivity  $\epsilon'(0)$  obtained from fit for two compressively strained thin films e.g. ETO/LAO and ETO/NGO are compared with the bulk sample in Fig.4.39. The highest permittivity is shown by bulk. The films have very low values of in-plane static permittivity due the presence of compressive strain and corresponding stiffening of the SM, which mainly contributes to  $\epsilon'(0)$ . Smallest value of  $\epsilon'(0)$  is shown by ETO/NGO probably due to the highest concentration of defect.

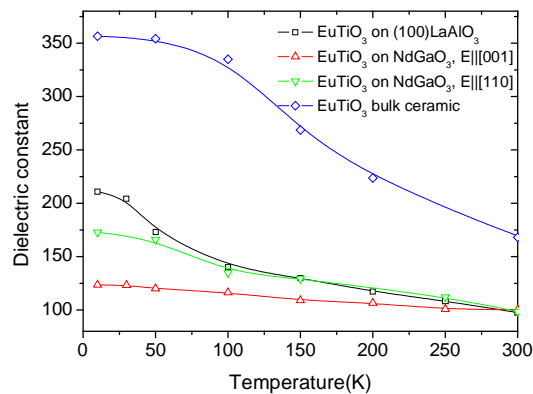


Fig.4.39. Temperature dependence of static dielectric constant in bulk ETO ceramics and ETO thin films deposited on LAO and NGO substrates.

## 4.5 Hexagonal manganites

These compounds are multiferroics with FE PT at high temperatures and Néel temperature below 100 K. The most representative material in this category is  $\text{YMnO}_3$  (YMO), but there are also other  $\text{RMnO}_3$  compounds (R is rare earth) studied in the literature. In this part we will focus on YMO single crystal and ceramics and  $\text{InMnO}_3$  (IMO) ceramics. We will mention also some results obtained on hexagonal  $\text{Y}_{1-x}\text{Eu}_x\text{MnO}_3$  ceramics,  $x=0-0.2$ .

The aim of the study of YMO and Eu doped-YMO is to find the magnons and electromagnons. It is well known that spin waves in magnetically ordered materials can be excited by the magnetic component of electromagnetic radiation, giving rise to a resonant dispersion of *magnetic* permeability in the MW and THz frequency region. Electromagnons are coupled spin-lattice excitations in multiferroics where the magnetic order coexists with FE one.<sup>161, 162</sup> Electromagnons are excited by the electric component of the electromagnetic radiation, therefore they can be detected in the THz *dielectric* permittivity spectra. They were predicted already in 1970<sup>163</sup> but the first experimental confirmation appeared as late as in 2006.<sup>161</sup> These excitations were mainly investigated in rare earth perovskite manganites<sup>164,165</sup> with orthorhombic structure and in hexaferrites.<sup>166</sup> Generally, the electromagnons were observed mainly in type-II multiferroics materials, where the FE phase is induced by a special kind of incommensurate spiral magnetic ordering. These materials exhibit no linear magnetoelectric (ME) effect, only higher order ME coupling. The magnon dispersion branches exhibit a minimum at the wave vector  $\mathbf{q}_m$  corresponding to the modulation vector of the ordered spins. In contrast with the magnons, which are rather sharp in THz spectra and their frequency corresponds to  $q = 0$  magnons, electromagnons exhibit very broad spectral lines and their frequencies correspond to  $q = \mathbf{q}_m$  and  $q$  from BZ boundary, i.e. the wave vectors, where the highest magnon density of states occurs.<sup>167,168</sup> As the probing THz radiation has a long wavelength (i.e. the wave vector  $q \approx 0$ ), the electromagnons cannot be excited by a resonant single-photon absorption due to wave vector conservation law. Therefore, the polar phonons should be involved in the absorption processes. Some researchers claim that the low frequency electromagnon is activated by the inverse Dzyaloshinskii Moriya mechanism, while the high frequency one by Heisenberg exchange coupling.<sup>169,170</sup> Others authors believed that both electromagnons can be explained by Heisenberg exchange coupling.<sup>171</sup> Up to now the electromagnons were observed mainly in type II multiferroics. Nevertheless, very recently electromagnons were reported also in  $\text{BiFeO}_3$ <sup>172,173,174</sup>,

which is type-I multiferroics with rather weak ME coupling. The question arises, if the electromagnons can exist in hexagonal manganites which belong also to type I multiferroics? It was the main motivation of our study.

#### 4.5.1 $Y_{1-x}Eu_xMnO_3$ ceramics, $x=0-0.2$

YMO is a high temperature FE below  $\sim 1250$  K<sup>175</sup> and it becomes AFM below 70 K.<sup>176,177</sup> It crystallizes in the space group  $P6_3/mmc = D_{6h}^4$ , ( $Z = 2$ ) in the high-temperature PE phase<sup>178</sup> and it transforms to polar space group  $P6_3cm$ , =  $C_{6v}^3$ , ( $Z = 6$ ) in the FE phase.<sup>179</sup> The absence of large Born effective charges and the polarization obtained by a buckling of layered  $MnO_5$  bipyramids accompanied by off-centered displacements of Y and in-plane O ions, have been referred to as geometrical ferroelectricity.<sup>37</sup> The polarization was found to be rather high, around  $5 \mu C/cm^2$ .<sup>180</sup> The magnetic order is given by a frustrated triangular basal plane spin structure.<sup>166</sup> Below  $T_N$  the magnetic symmetry is  $P\bar{6}_3cm$ <sup>181</sup> and therefore the linear ME coupling is forbidden. Nevertheless, higher order ME coupling is allowed in YMO. For example a coupling of AFM and FE domain walls was observed by means of optical SHG microscopy.<sup>182,183</sup> However, a large spin-phonon coupling manifests itself by a decrease of the low-frequency permittivity near  $T_N$ .<sup>38</sup> This decrease is probably caused by anomalous hardening of several IR active phonons.<sup>184</sup> Nénert et al. revealed a new intermediate phase between 1125 and 1350 K in a single crystal of  $YMnO_3$  using dilatometry and differential thermal analysis.<sup>185</sup> The existence of the intermediate phase is still under debate, but on the other hand there is a relative large spread of published  $T_C$  values in literature from 913 to 1270 K.<sup>179</sup>

First principle calculations<sup>186</sup> show that the intermediate phase is less favorable than a single improper FE PT. According to them, the FE PT is caused by a softening of optical phonon at the Brillouin zone boundary with  $q=(1/3,1/3,0)$  and spontaneous polarization arises from the coupling of this phonon to a zone center mode. If this is true no pronounce dielectric anomaly is expected near  $T_C$ . Recently, the high-resolution powder neutron diffraction investigations proved that no intermediate phase was found in YMO single crystal.<sup>175</sup> They found that transition is driven mainly by the AFD  $K_3$  mode i.e. the FE PT is an improper one. Inelastic neutron scattering (INS) revealed three magnon branches. Two of them are degenerated near the BZ center and have frequency near  $40 \text{ cm}^{-1}$ .<sup>177,187</sup> Moreover, recent polarized INS studies revealed that the excitation seen at 1.5 K near  $40 \text{ cm}^{-1}$  has a hybrid character of magnetic spin waves and a lattice vibration,

i.e. it should contribute to both *magnetic* and *dielectric* susceptibilities (like electromagnon). This fact motivated us for studies of IR and THz spectra of YMO and Eu doped-YMO up to 900 K.<sup>188</sup>

The IR reflectivity spectra of YMO ceramics are plotted up to 900 K in Fig.4.40a). The spectra of  $Y_{1-x}Eu_xMnO_3$ ,  $x=0.1$  and  $0.2$  are similar and I will not show here. A gradual decrease of reflection band intensities with increasing temperature is seen. This is caused by an increase of phonon dampings with temperature. Parameters of the observed phonons were obtained from fits. Generally, the reflectivity spectra are related to the complex index of refraction

$$n^*(\omega) = \sqrt{\varepsilon^*(\omega)\mu^*(\omega)} .$$

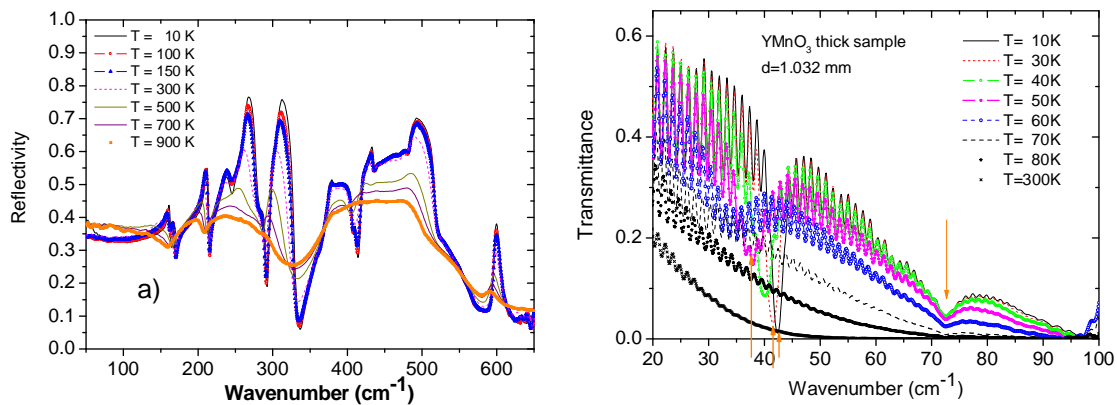


Fig.4.40a) Temperature dependence of IR reflectivity spectra of YMO ceramics; b) FIR transmission spectra at selected temperatures. Two absorptions are seen near 40 and 73  $cm^{-1}$ . The lower one shifts with temperature.

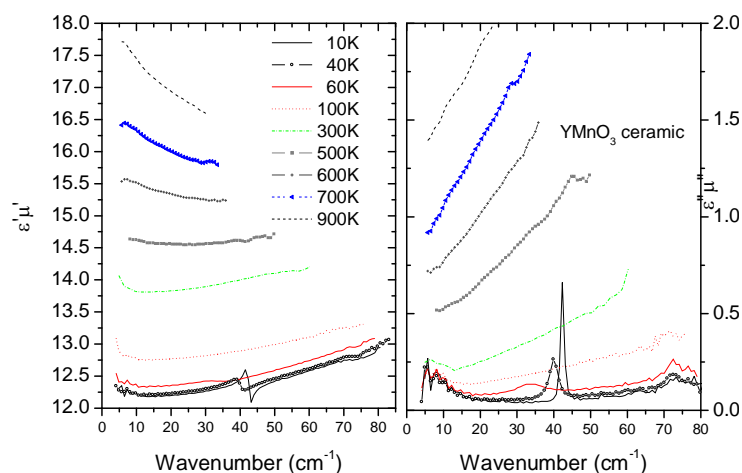


Fig.4.41. Temperature dependence of real and imaginary parts of experimental THz spectra of the product  $\varepsilon^* \mu^*$  in a broad temperature range. The spin wave near 40  $cm^{-1}$  is clearly seen; a weaker excitation near 73  $cm^{-1}$  is also apparent – see also FIR transmission spectra in Fig. 4.40.



The low frequency part (below  $100 \text{ cm}^{-1}$ ) of FIR spectra of YMO ceramics was actually investigated by means of three independent techniques: FIR reflectivity (Fig.4.40a), FIR transmission (Fig.4.40b) and time-domain THz transmission spectroscopy (Fig.4.41)

The last one gives directly the real and imaginary parts of the product  $\varepsilon^*(\omega)\mu^*(\omega)$ . Note that  $\varepsilon^*(\omega)$  and  $\mu^*(\omega)$  cannot be unambiguously separated in magnetic materials, if we do not have any additional information, which excitation is magnetic and which polar. All these spectra were fitted simultaneously and the obtained complex spectra are shown in the Fig. 4.42. A sharp resonant peak is seen near  $40 \text{ cm}^{-1}$  in Fig. 4.41. This is an AFM resonance which was briefly described in Ref.[189]. The AFM resonance causes dispersion only in  $\mu^*(\omega)$  spectra and its frequency decreases on heating towards  $T_N$ . Similar AFM resonances with slightly lower frequencies were observed also in  $\text{Y}_{1-x}\text{Eu}_x\text{MnO}_3$  ceramics,  $x=0.1$  and  $0.2$ .

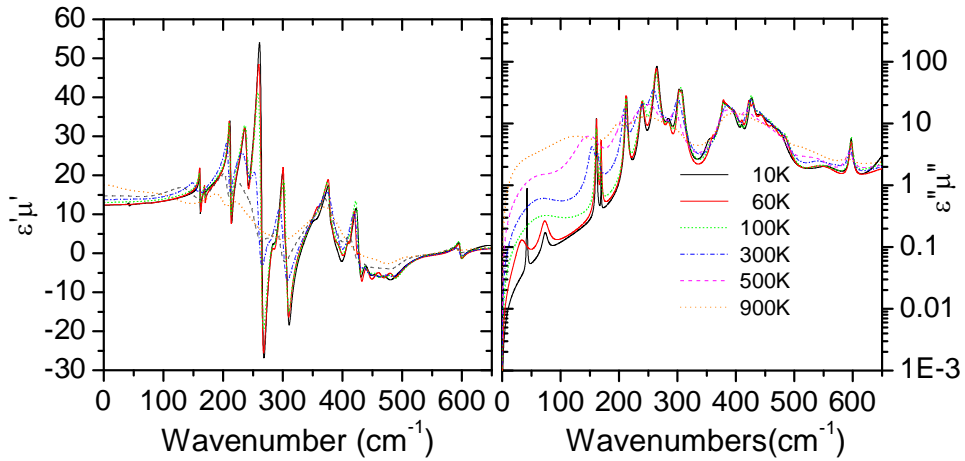


Fig.4.42. Real and imaginary part of the product  $\varepsilon^*(\omega)\mu^*(\omega)$  in YMO ceramics at selected temperatures obtained from simultaneous fit of THz and FIR spectra

Polarized IR reflectivity spectra of YMO single crystal were already published.<sup>184</sup> 9  $A_1$  and 14  $E_1$ -symmetry polar modes are allowed from the factor group analysis<sup>190</sup> for the  $\mathbf{E}\parallel\mathbf{c}$  and  $\mathbf{E}\perp\mathbf{c}$  polarized spectra, respectively. Zaghrioui et al.<sup>184</sup> observed 7  $A_1$  modes and 8  $E_1$  modes. The spectra of ceramics are unpolarized, therefore we see a mixture of both polarized spectra. Especially above  $350 \text{ cm}^{-1}$ , the modes are highly overlapped and it is very difficult to distinguish all the modes in the reflectivity spectra. In spite of this, we used 24 oscillators for the fits of the spectra at 10 K (including one magnon), which exactly corresponds to the number of polar

phonons expected from the factor group analysis. 10 polar mode frequencies are similar to the frequencies observed in the single crystal. The rest of the phonons have slightly different frequencies because the fit of ceramics describe a mixture of  $A_1$  and  $E_1$  spectra and the effective mode frequencies in ceramics can be shifted from the  $A_1$  and  $E_1$  modes frequencies. Fig. 4.44 shows the frequencies of phonons which exhibits some relatively stronger temperature dependences. Other modes, which are not plotted in the Fig.4.43 have the following frequencies (in  $\text{cm}^{-1}$ ) at 10 K: 73.8, 239.5, 284.8, 302.2, 354.4, 378.2, 382.8, 394.7, 410.3, 426.7, 442.3, 458.0, 472.5, 477.1, 555.0, 597.1 and 666.7. The small decrease of phonon frequencies in the Fig.4.45 is mainly due to the thermal expansion with increasing temperature.

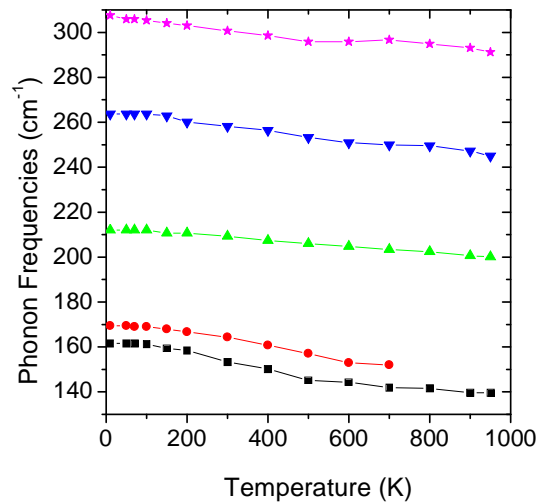


Fig.4.43. Temperature dependence of the selected phonon frequencies in the YMO ceramics.

The THz spectra in Fig. 4.41 taken above  $T_N$  are just  $\epsilon^*(\omega)$  spectra, because the AFM resonances contributing to  $\mu^*(\omega)$  is seen only below  $T_N$ . One can see that  $\epsilon'$  increases on heating, so that the static permittivity  $\epsilon'(0)$  increases from 12.5 (at 10 K) to 17.8 (at 900 K). Such a change is rather small and is caused by the small polar phonon softening on heating. In the case of proper FE PT  $\epsilon'(0)$  should increase on heating towards  $T_C$  according to Curie-Weiss law (Eq. 2.18). The observation of only small  $\epsilon'(0)$  increase on heating supports the improper character of the FE PT originally suggested by Fennie and Rabe.<sup>186</sup> In this case the FE PT is driven by a SM from BZ boundary with  $q=(1/3, 1/3, 0)$  which does not contribute to  $\epsilon'(0)$  above  $T_C$ . It can contribute to  $\epsilon'(0)$  only in the FE phase, but the dielectric strength of this newly IR-

activated mode is usually very small; so the change of  $\varepsilon'(0)$  with temperature is also very weak. A small change of THz  $\varepsilon'$  near  $T_C$  can be expected also in the case of an order–disorder phase transition, but in this case some larger structural disorder should be seen in XRD of PE phase, which was never reported.<sup>178,179</sup>

FIR transmission and THz spectra reveal sharp resonant absorptions near  $40 \text{ cm}^{-1}$  in the AFM phase of YMO. This is the AFM resonance briefly reported in Ref.[189] and its frequency corresponds to the zone center magnon seen in INS spectra.<sup>191,177,187</sup> The same AFM resonance was revealed also in the THz spectra of  $\text{Y}_{1-x}\text{Eu}_x\text{MnO}_3$ , with  $x=0.1$  and  $x=0.2$ ; its frequency is slightly lower than that for YMO. Another sharp absorption is seen in FIR transmission spectra near  $73 \text{ cm}^{-1}$ . A hint of this is seen also in THz spectra. Unfortunately, it can be revealed only at low temperature below 60 K; i.e. in the AFM phase, because the sample is not transparent at higher temperatures. It is not clear whether this excitation is a magnon or it has phonon origin, but it is not seen in IR reflectivity spectra, because its dielectric strength is very small ( $\Delta\varepsilon \approx 0.1$ ). However, this mode does not disappear even at higher temperatures. It becomes heavily damped up to 900 K (broad loss maximum below  $100 \text{ cm}^{-1}$  in Fig. 4.42). Oscillator strength of this mode increases on heating. Possible origin of this mode will be discussed in the part about YMO single crystal because it is seen also there.

#### 4.5.2 *YMnO<sub>3</sub> single crystal*

Polarized FIR and THz spectra we measured in hexagonal YMO single crystal. The crystal plates were probed using the THz and FIR beams in all possible geometries:  $\mathbf{E} \perp \mathbf{c}$ ,  $\mathbf{H} \perp \mathbf{c}$ ;  $\mathbf{E} \perp \mathbf{c}$ ,  $\mathbf{H} \parallel \mathbf{c}$  and  $\mathbf{E} \parallel \mathbf{c}$ ,  $\mathbf{H} \perp \mathbf{c}$ . It enables to access the complex spectra of products  $\varepsilon_a \times \mu_a$ ,  $\varepsilon_c \times \mu_a$  and  $\varepsilon_a \times \mu_c$  as shown in the Fig. 4.44.

The peak at  $40 \text{ cm}^{-1}$  already seen in YMO ceramics appears in single crystal at low temperatures in the spectra of  $\varepsilon_a \times \mu_a$ ,  $\varepsilon_c \times \mu_a$ , but not in  $\varepsilon_a \times \mu_c$  spectra is definitely the AFM resonance as it contributes only to the magnetic permeability  $\mu_a$ . The AFM resonance vanishes above  $T_N \sim 70 \text{ K}$ . The data shown in Fig.4.45 allows to assume that  $\mu_c=1$  in the THz range. This is in agreement with the magnetic order of YMO in the AFM phase: the spins are ordered in separated layers in the hexagonal plane such that the magnetic resonances are not expected to be excited with  $\mathbf{H} \parallel \mathbf{c}$ . Based on this assumption; the complex values of the permeability  $\mu_a$  and permittivity  $\varepsilon_c$  are retrieved (see Fig.4.45).

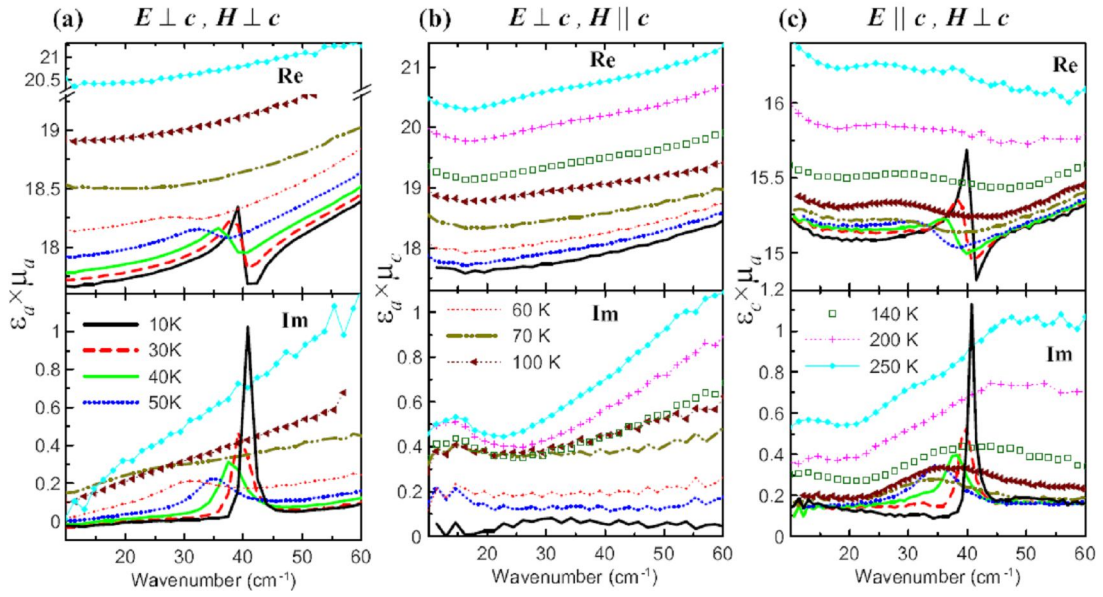


Fig.4.44. Complex THz spectra of YMO single crystal taken at selected temperatures. The polarization of THz beam is indicated above the figures. The AFM resonance near  $\sim 40 \text{ cm}^{-1}$  contributes to the *magnetic* permeability  $\mu_a$  spectra

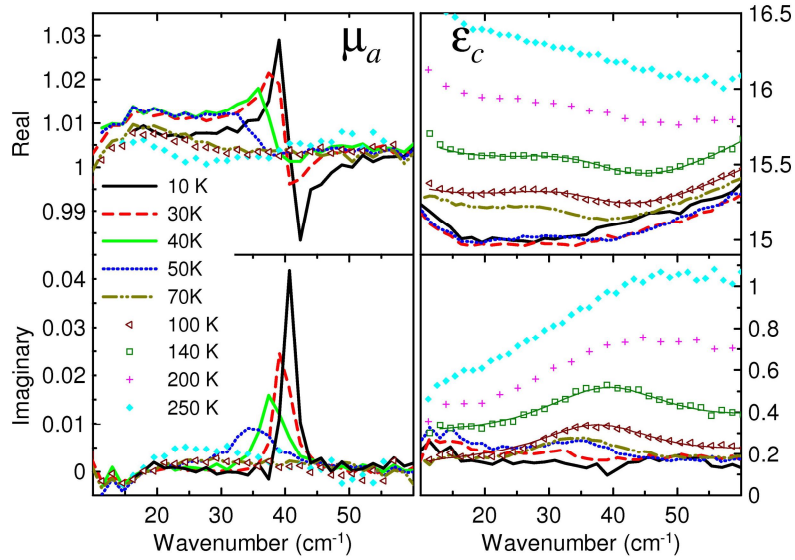


Fig.4.45. Temperature dependence of the complex permittivity  $\epsilon_c$  and permeability  $\mu_a$  spectra from data plotted in Fig. 4.44. The solid  $\epsilon_c$  curves at 100 and 140 K result from the oscillator fit.

The spectra of  $\mu_a$  were fitted by a damped harmonic oscillator and the resulting AFM resonance frequency  $\omega_{\text{mag}}$  is plotted in Fig.4.46. A strong softening of  $\omega_{\text{mag}}$  is seen upon heating towards  $T_N$ .

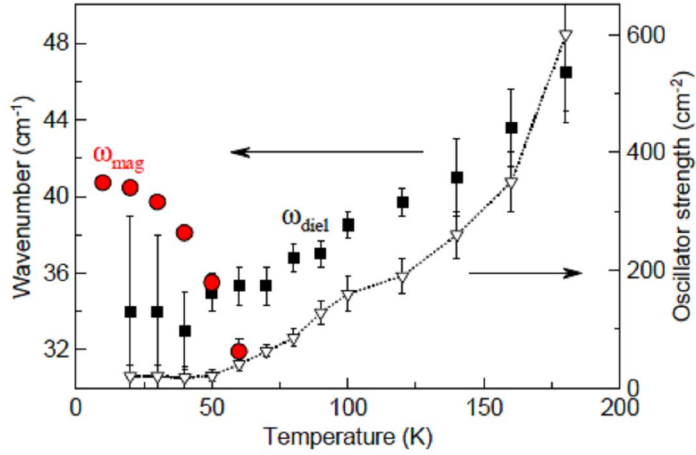


Fig.4.46. Temperature dependence of magnon (closed red circles) and dielectric absorption peak frequency (closed black squares). In the same figure is plotted also the temperature dependence of oscillator strength (open triangles) of the dielectric absorption.

Besides the sharp AFM resonance in the low-temperature  $\mu_a$  spectra one can see a broad dielectric absorption around  $40 \text{ cm}^{-1}$  in the  $\epsilon_c$  spectra. This feature is detected even above  $T_N$ , where its strength remarkably increases with rising temperature. The presence of such resonance in  $\epsilon_c$  is qualitatively expected from a simple comparison of the raw data in Fig.4.44 a) and c). The accessible spectral range of the THz measurements for our sample is limited to  $\sim 60 \text{ cm}^{-1}$ , therefore we have performed also FIR transmission (up to  $100 \text{ cm}^{-1}$ ) and reflectivity (up to  $650 \text{ cm}^{-1}$ ) measurements for all polarizations.

Example of FIR experimental transmittance spectrum obtained at 120 K and its various fits are shown in the Fig.4.47. Oscillations observed in the spectrum are the Fabry-Perot interferences in the plane-parallel sample.

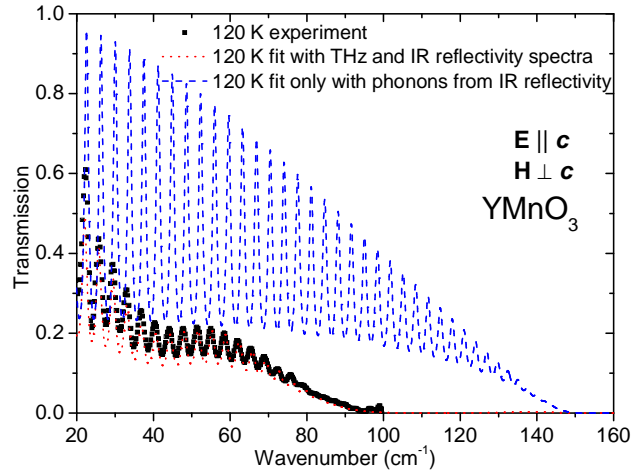


Fig.4.47. FIR transmission spectrum of 348  $\mu\text{m}$  thick YMO crystal with polarization  $\mathbf{E} \parallel \mathbf{c}$  obtained at 120 K. Dashed blue lines: Theoretical transmission spectrum obtained from the fit of FIR reflectivity spectra (i.e. fitting using only polar phonons above  $150 \text{ cm}^{-1}$  without considering modes observed by THz and FIR transmission spectra below  $100 \text{ cm}^{-1}$ ). Dotted red line: Simultaneous fit of FIR reflectivity, FIR transmission and THz spectra.

A weak minimum observed near  $40 \text{ cm}^{-1}$  corresponds to the broad absorption peak detected in the THz dielectric spectra. According to FIR reflectivity (not shown here), the lowest frequency polar phonons lie above  $150 \text{ cm}^{-1}$  in both polarized  $\mathbf{E} \parallel \mathbf{c}$  and  $\mathbf{E} \perp \mathbf{c}$  spectra. Nevertheless, simultaneous fits of the THz complex permittivity and FIR transmittance and reflectivity reveal several additional modes below these phonon frequencies. In Fig.4.48A are plotted the spectra. Below  $T_N=70 \text{ K}$ , the spectra correspond to imaginary part of  $\epsilon^* \mu^*$ . Above  $T_N$ , the spectra correspond to  $\epsilon''(\omega)$ . Besides the sharp magnon at  $40 \text{ cm}^{-1}$ , three other modes at roughly 10, 40 and  $100 \text{ cm}^{-1}$  were assumed in the fitting procedure in order to account for the measured shape of the  $\mathbf{E} \parallel \mathbf{c}$  spectra at 10 K (Fig.4.48Aa). The additional modes remain in the spectra up to room temperature and their strength increases on heating. Also in  $\mathbf{E} \perp \mathbf{c}$  polarized spectra, two broad modes observed near 10 and  $90 \text{ cm}^{-1}$  were used for the fits above 50 K. The features observed near  $10 \text{ cm}^{-1}$  in both polarized spectra could be related to low frequency magnons experimentally observed in INS spectra<sup>187</sup>. Their dispersions in the BZ are plotted in Fig.4.49. However, the sensitivity and accuracy of our THz spectra below  $20 \text{ cm}^{-1}$  is limited; therefore we cannot exclude that it is only an artifact. For this reason we will not speculate about the origin of this excitation. All the other modes appearing below  $150 \text{ cm}^{-1}$  are clearly observed in the THz and/or FIR

transmission spectra while the FIR reflectivity measurements are not sensitive enough to detect and resolve these weak and broad spectral features. Their origin will be discussed below.

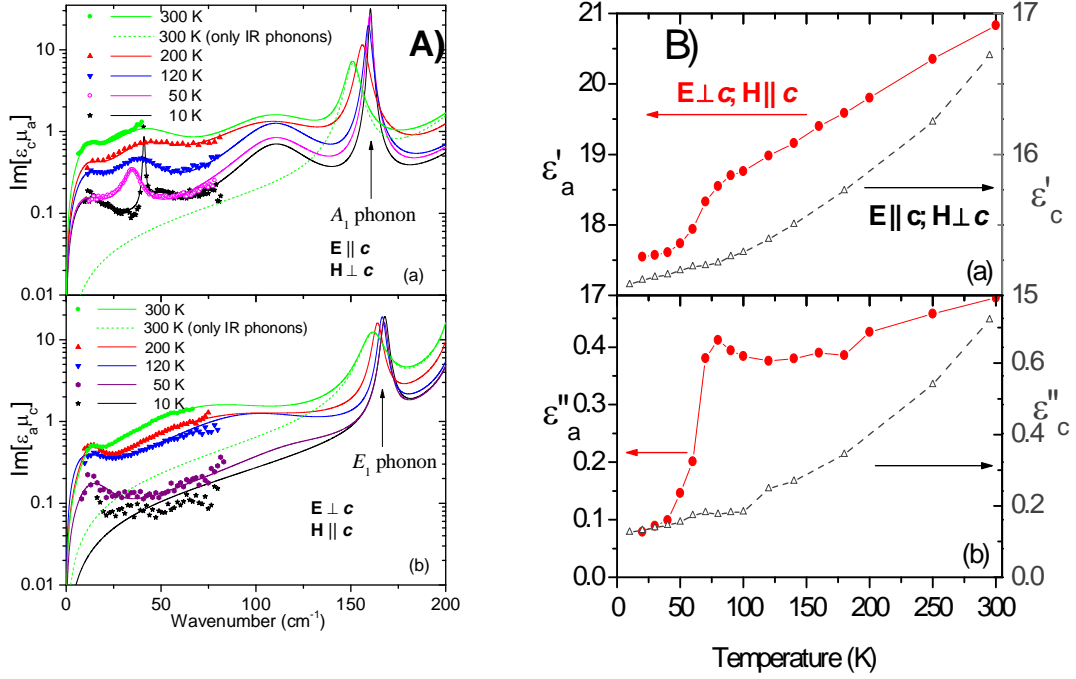


Fig.4.48. **A**) The measured THz loss spectra of YMO (symbols) and those obtained from the fits of FIR transmission and reflectivity spectra; **B**) Temperature dependence of the (a) permittivity and (b) dielectric loss measured at 20 cm<sup>-1</sup> with polarizations  $\mathbf{E} \perp \mathbf{c}$  and  $\mathbf{E} \parallel \mathbf{c}$ .

The temperature dependence of the sub-THz complex dielectric permittivity  $\epsilon_a$  plotted in Fig.4.48B) for 20 cm<sup>-1</sup> exhibits a pronounced drop below  $T_N$ . Such anomaly is a typical feature of large spin phonon coupling which occurs only in hexagonal planes of YMO where the spins are ordered. For that reason the anomaly is not observed in  $\epsilon_c(T)$ .

The AFM PT is accompanied by unusually large atomic displacements which were detected by neutron diffraction<sup>192</sup>; for this reason the phonon frequencies changes below  $T_N$ . The decrease in  $\epsilon'_a$  and  $\epsilon''_a$  is mainly caused by hardening of the  $E_1$  symmetry polar mode seen near 250 cm<sup>-1</sup> in IR reflectivity spectra with polarization  $\mathbf{E} \perp \mathbf{c}$ .<sup>184</sup> Similar temperature dependence of  $\epsilon'_a$  was observed also in the radiofrequency region<sup>38</sup> providing evidence of the absence of dielectric dispersion below 100 GHz. Gradual decrease of  $\epsilon'_a$  and  $\epsilon'_c$  on cooling from 300 to 100

K is an usual behavior caused by a small phonon stiffening as a consequence of thermal contraction.

The problem is the origin of the absorption bands appearing below phonon resonances in Fig.4.48.A. They are much weaker and significantly broader than those of polar phonons and their strength increases when the temperature is increased in the PM phase. Their frequency lying in the range of 40-100  $\text{cm}^{-1}$  coincides with those of the magnon branch observed by INS at 7 K over the BZ (see Fig. 4.49).<sup>193</sup>

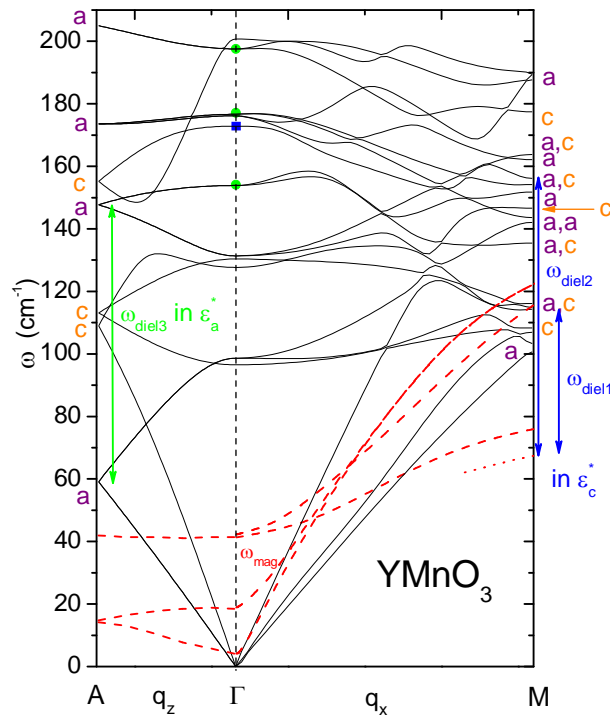


Fig.4.49. Dispersion branches of phonons calculated from first-principle calculations (black solid lines). In the same graph are plotted the magnon dispersion branches obtained experimentally by INS at 7 K (red dashed lines).<sup>193</sup> The red-dotted line indicates the presumed dispersion of the paramagnon near the M-point. The symbols shown at the BZ-edges indicate the polarization of the phonons at BZ boundary: *a* means phonons polarized within the hexagonal plane and *c* means phonons polarized in the perpendicular direction.  $E_1$  and  $A_1$ -phonons observed experimentally are marked by green and blue points at the  $\Gamma$ -point.  $\omega_{diel1}$  and  $\omega_{diel2}$  indicate phonon-paramagnon excitations observed in the dielectric loss spectra of  $\epsilon_c''$ . Green arrow marked as  $\omega_{diel3}$  indicates a broad multiphonon absorption observed in the  $\epsilon_a''$  loss spectra (see Fig. 4.48A).

It is well established that Mn spins exhibit a strong short-range correlation in hexagonal YMO far above  $T_N$ . This was proved by an anomalous behavior of the thermal conductivity,<sup>194</sup> elastic moduli,<sup>195</sup> as well as by neutron scattering experiments.<sup>196,197,198</sup> One can expect the



existence of only short-wavelength paramagnons due to short range correlations of the spins in the hexagonal plane of YMO i.e. magnons with the large wavevector  $\mathbf{q}_x$  near the M-point of the BZ. The paramagnon branch is schematically plotted together with experimentally determined<sup>193</sup> magnon branches in the Fig. 4.49. Note that paramagnon frequency is lower than that of the magnon one measured at 7 K as the magnon frequency decreases by almost  $10 \text{ cm}^{-1}$  on heating towards  $T_N$ .

The possibility of existence of electromagnons in hexagonal YMO is excluded because the dielectric excitations are presented in our spectra up to room temperature and their strength increases on heating while intensity of electromagnons should exhibits an opposite temperature behavior. Moreover, electromagnons usually disappear from the spectra at  $T_N$  or close above  $T_N$ .<sup>164,166,165</sup>

Nevertheless, that broad absorption observed in the dielectric spectra reflects an excitation which must be somehow coupled with phonons. The calculated phonon dispersion branches are plotted together with magnon branches in the Fig. 4.49. The phonon spectra were calculated using first principle calculations<sup>199</sup> by Rushchanskii and Ležaič (from Forschungszentrum Jülich, Germany).

As we pointed out above, the absorption strength significantly increases on heating. This is typical for two excitation difference frequency absorption. Such process includes the annihilation of one thermally excited quasi-particle (phonon or magnon) with frequency  $\omega_1$  and the creation of another quasi-particle with higher frequency  $\omega_2$ . The dielectric resonance then occurs at frequency  $\omega_{diel} = \omega_2 - \omega_1$ . This process can involve excitations from the whole BZ provided that total wave vector is conserved, but the most probably take part of the branch from BZ boundary, where the density of states is the highest. The process is strongly temperature dependent, as it is related to the population of excitations with frequency  $\omega_1$ , which follows the Bose-Einstein statistics. At low temperatures the populations of the levels are close to zero and the differential absorption then practically vanishes. It becomes more probable when the energy level is thermally populated at higher temperatures.

This is in qualitative agreement with our observation. The difference transitions at the BZ boundary are possible only between the phonons with the same symmetry and if the total wave vector is conserved (i.e. the transition must be vertical in the wave vector space). The broad

absorption near  $90 \text{ cm}^{-1}$  seen in  $\varepsilon_a$  spectra can be explained by such difference two-phonon absorption. Phonons near  $60$  and  $150 \text{ cm}^{-1}$  at the A-point of BZ are polarized in the hexagonal plane (marked as  $\mathbf{a}$  in Fig.4.49) and their difference gives the frequency  $\omega_{diel3} = 90 \text{ cm}^{-1}$ , as observed.

However, it is impossible to explain the two peaks seen in  $\varepsilon_c$  spectra around  $\omega_{diel1} = 40$  and  $\omega_{diel2} = 100 \text{ cm}^{-1}$  by multiphonon absorption. The frequency of the  $\mathbf{c}$ -polarized phonons at the BZ edge is higher than  $100 \text{ cm}^{-1}$ . It means that the population of such phonons should be much lower than that of  $\mathbf{a}$ -polarized phonons at  $60 \text{ cm}^{-1}$ . For this reason the strength of the difference (multiphonon) absorption in  $\varepsilon_c^*$  spectra should be weaker than in  $\varepsilon_a^*$  spectra. Moreover, within such a hypothesis, a continuous absorption band would be expected in the spectra due to the large number of  $\mathbf{c}$ -polarized phonons at the M-point (see Fig. 4.49). This is in contradiction with the experimental results presented in Fig. 4.49. In such circumstances, we are assuming the existence of paramagnons near the M-point and in this case differential paramagnon-phonon absorption with several maxima can be obtained. Moreover, because of the similar Bose-Einstein factor for the paramagnon and phonon near  $60 \text{ cm}^{-1}$  at the A-point, the absorptions observed in both  $\varepsilon_a^*$  and  $\varepsilon_c^*$  have a comparable strengths. This fits well with our experiments. The frequency  $\omega_{diel1}$  increases on heating presumably due to the softening of paramagnon branch with increasing temperature.

### 4.5.3 *InMnO<sub>3</sub> ceramics*

In this paragraph we will briefly report several results we have obtained on  $\text{InMnO}_3$  (IMO) ceramics. There are only few papers dedicated to this materials.<sup>200,201,202,203</sup> Magnetic and dielectric properties of hexagonal IMO are still not clarified and remain controversial compared with other hexagonal  $\text{RMnO}_3$  ( $\text{R}=\text{Sc}$ ,  $\text{Y}$ , and  $\text{Ho-Lu}$ ). Very weak anomalies were observed in the magnetic susceptibility near  $15$ ,  $40$ , and  $120 \text{ K}$ .<sup>201,202</sup> The FE PT occurs according to low-frequency dielectric data published in Ref [203] near  $500 \text{ K}$ , but these data can be strongly influenced by conductivity at such high temperature. Or that reason we have performed high-frequency experiments in the THz and IR range at temperatures up to  $900 \text{ K}$  to clarify the nature of the FE phase transition. Our IR and THz data, which are not influenced by conductivity, as

well as M. Savinov's investigation of the FE hysteresis loop have finally shown that IMO is not FE.<sup>112</sup>

Our colleague A. Belik from Japan prepared IMO ceramics using a high-pressure and high-temperature sintering and measured the magnetic properties. They confirmed an AFM PT with  $T_N$  around 118 K.<sup>112</sup>

From dielectric point of view, we have found no anomaly in the complex dielectric permittivity measured at 1 THz between 300 K and 900 K (see inset of Fig. 4.50).  $\epsilon'(T)$  increases gradually from 16.6 at 300 K to 18.6 at 900 K while a peak in THz  $\epsilon'(T)$  should be seen in the case of a displacive FE PT. Such permittivity values of InMnO<sub>3</sub> are in agreement with those of other hexagonal manganites RMnO<sub>3</sub> (R=Sc, Y and Lu) i.e.  $\epsilon'$  lies between 15 and 22 at 150 K.<sup>204</sup>, but does not confirm huge permittivity ( $10^3$ ) observed in Ref. 203. It gives evidence, that the previously published<sup>203</sup> in  $\epsilon'(T)$  is caused by conductivity and related Maxwell-Wagner polarization.

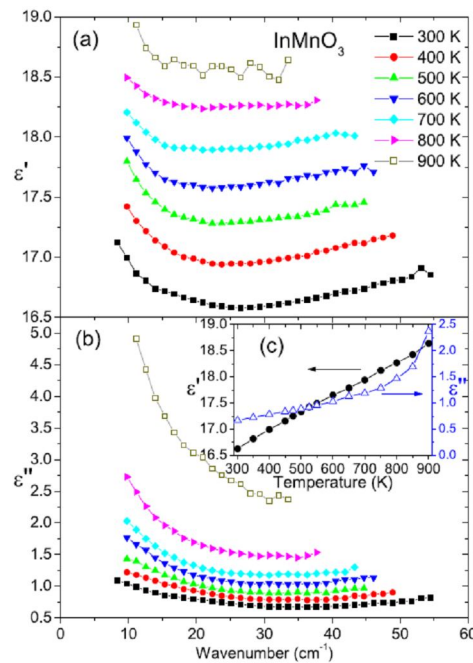


Fig.4.50. Frequency dependence of a) real and b) imaginary parts of complex permittivity in a THz range at different temperatures. c) Temperature dependence of  $\epsilon'$  and  $\epsilon''$  measured at 1 THz on heating is plotted in inset.

The small increase of  $\epsilon'$  with rising temperature is caused by a slight shift of several phonon frequencies to lower values (i.e. phonon softening) observed in the IR reflectivity spectra

(see Fig. 4. 51) Mainly the phonon near  $155\text{ cm}^{-1}$  exhibits a  $10\text{ cm}^{-1}$  shift down. Thanks to conservation of oscillator strengths  $f_j = \Delta\varepsilon_j\omega_j^2 = \text{const.}$  of the j-th polar phonon, the decrease of phonon frequency  $\omega_j$  is connected with the increase of dielectric strength  $\Delta\varepsilon_j$

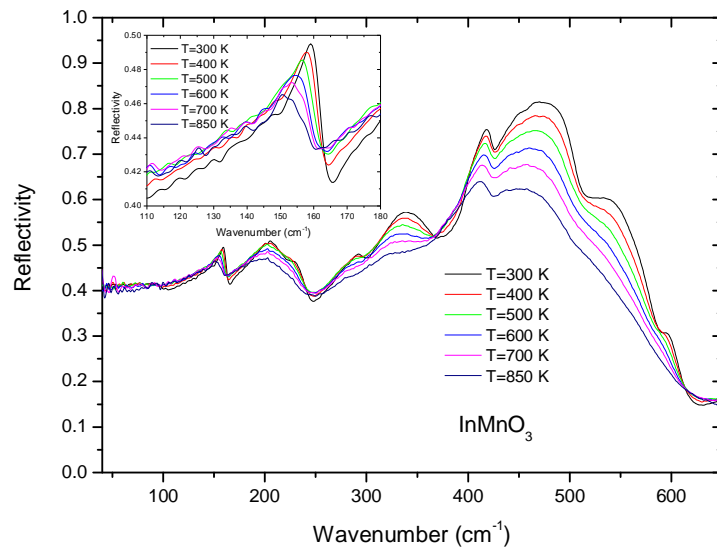


Fig.4.51. IR reflectivity spectra of IMO taken at selected temperatures

THz spectra show not only the phonon contribution, but also increasing absorption below  $20\text{ cm}^{-1}$  which can be caused by some MW dielectric relaxation or conductivity. The later possibility is more probable because the conductivity and related Maxwell Wagner polarization strongly influence the low-frequency dielectric data.<sup>205</sup> Moreover, no phonons disappear from the IR spectra at high temperatures giving evidence that the structure does not change at least up to 850 K. Additional measurements made by our colleagues show no ferroelectric hysteresis loop at low temperatures,<sup>112</sup> so we can conclude, that IMO is not multiferroic, because it is PE at all temperatures.

## 4.6 SrMnO<sub>3</sub> ceramics

SrMnO<sub>3</sub> (SMO) can crystallize in two forms with cubic and hexagonal structure. While the former structure is built from corner-sharing MnO<sub>6</sub> octahedra only, the later (and more stable) forms a four layer hexagonal structure with both face - sharing and corner – sharing octahedra corresponding to hexagonal and cubic stacking, respectively.<sup>113</sup>

In this work we will focus only on investigation of the cubic SMO. It can be obtained by quenching of the originally hexagonal SMO from high temperatures and maintained it as a metastable compound at low temperatures. Cubic SMO adopts a G-type<sup>206</sup> AFM structure at low temperatures and the magnetic moment at the Mn site is found to be  $2.6 \pm 0.2 \mu_B$  at liquid nitrogen temperature.<sup>207</sup> The Néel temperature is reported to be 260 K by Takeda and Ohara<sup>207</sup> while more recent results Kikuchi et al.<sup>208</sup>, and Chmaissem et al.<sup>209</sup> give 250 and 233 K, respectively. These values are caused probably by differences in the oxygen stoichiometry of the sample.

Main motivation for our studies was first principles calculations, which predicted a large spin-phonon coupling in SMO.<sup>210</sup> Lee and Rabe suggested to use it for an induction of strong FE FM using a strain in the thin SMO films.<sup>210</sup> The spin-phonon coupling should be manifested by change of phonon frequencies near  $T_N$ . From that reason we have focused on THz and FIR studies of the bulk cubic SMO ceramics down to low temperatures in order to reveal a possible coupling between the magnetic order and phonons.

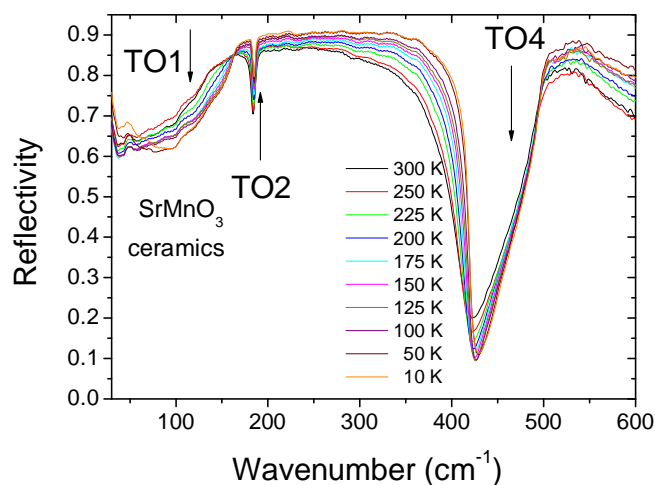


Fig.4.52. IR reflectivity spectra of SMO ceramics below room temperature. Frequencies of polar phonons are marked by arrows.

The IR reflectivity spectra of bulk SMO ceramics obtained between 300 K and 10 K are shown in the Fig.4.52. The IR spectra reveal three reflection bands, which correspond to cubic  $Pm\bar{3}m$  perovskite structure. The structure does not change during the cooling down to 10 K because no significant changes (appearance of new modes) are seen in the spectra. However, below  $T_N \approx 250$  K a remarkable hardening of TO1 mode is seen on cooling (see Fig. 4.54). The phonon frequency changes from 140 to 163  $\text{cm}^{-1}$ . According to our knowledge, such dramatic 17% stiffening of phonon frequency has been never observed in nonferroelectric materials and it gives evidence about huge spin-phonon coupling in SMO. Thanks to this also a large decrease of static permittivity from 140 to 108 is seen. Our experimental results completely correspond to predicted theoretical results from first-principle calculations and therefore the study of SMO strained thin films, where the strain induced FE and FM ordering with critical temperatures around 150 K is expected, is highly promising. We have already obtained tensile strained thin films from Prof. Schlom's group. They are deposited on DSO and  $\text{TbScO}_3$  substrates (tensile strain in the SMO film is 3.8 and 4.2%) and their MW, THz and FIR investigations are in progress.

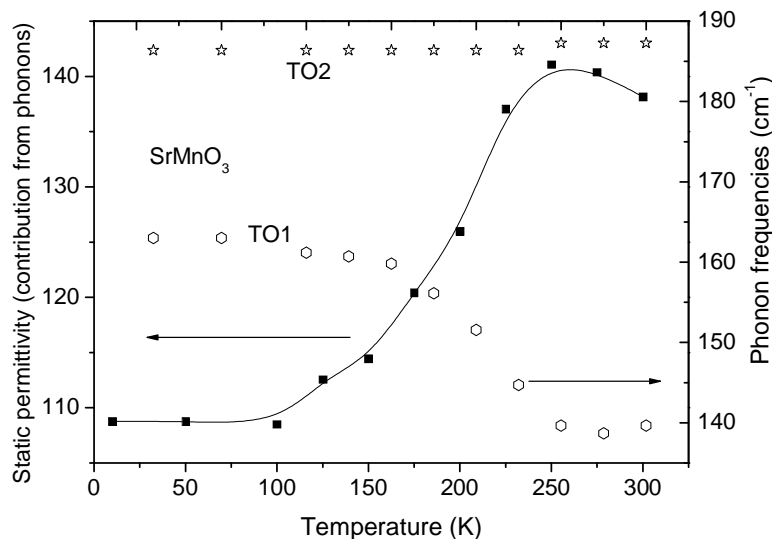


Fig.4.53. Temperature dependence of TO1 and TO2 mode frequencies (right scale) and temperature dependence of static permittivity calculated from phonon contributions (left scale).

## 4.7 Sr<sub>2</sub>TiMnO<sub>6</sub> ceramics

Sr<sub>2</sub>TiMnO<sub>6</sub> (STMO) is a double perovskite associated with high degree of B-site cation disorder. The structure and magnetic characteristics of STMO ceramics was first reported by Roa-Rojas et al.<sup>211</sup>. According to this report, the structure of STMO was tetragonal with lattice parameters  $a=5.4702 \text{ \AA}$  and  $c=7.7361 \text{ \AA}$  and a magnetic phase transition from FM to PM phase occurs at 44.8 K. The high  $\epsilon'$  values seen in STMO ceramics above 180 K were attributed to the Maxwell–Wagner type polarization due to conductivity.<sup>212</sup> There were reported also some dielectric properties above room temperature (up to 700 K), where the conductivity is significantly high giving rise to more extrinsic effects.<sup>213</sup>

It is well known that STO is a quantum PE and already small amount of doping changes its properties to relaxor FEs. Shvartsman et al.<sup>214</sup> recently reported that already 2% of Mn in STO can induce even multiglass behavior, i.e. both FE relaxor and spin glass behavior was observed simultaneously. So the question arises, cannot 50% of Mn in Ti sites of STO induce a FE PT? It was the main motivation of our FIR studies, because revealing the FE PT in STMO would mean discovery of a new multiferroic.

Our IR reflectivity<sup>114</sup> spectra seen in Fig.4.54 consist of six polar modes, whose frequencies at 117, 141, 165, 189, 467, and 539 cm<sup>-1</sup> are marked with arrows. Number of observed phonons does not change on cooling to 10 K, so no change of structure can be expected.

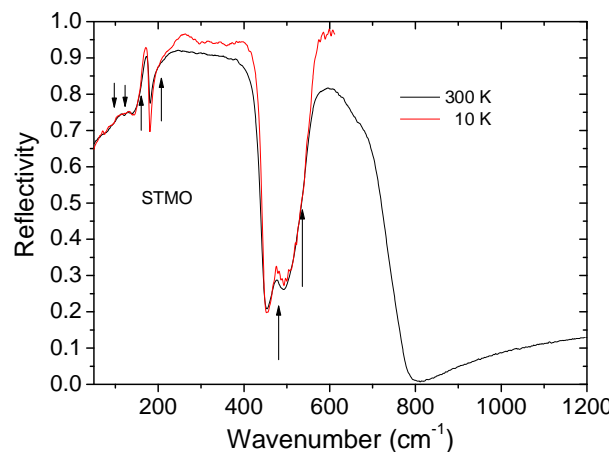


Fig.4.54. IR reflectivity spectra of STMO ceramics at 10 and 300 K. Frequencies of polar modes are marked with arrows. The low temperature IR spectrum was taken only below 600 cm<sup>-1</sup> due to opacity of polyethylene windows in cryostat. (after Ref.114)

A disordered double perovskite with  $Pm\bar{3}m$  structure allows theoretically only 3  $F_{1u}$  IR modes and none are Raman active.<sup>131,215</sup> Four IR active modes (of symmetry  $F_{1u}$ ) are allowed in a completely ordered double perovskite system possessing  $Fm\bar{3}m$  crystal structure.. One can see that the number of observed polar modes in both spectra is much higher than the predicted. It gives evidence that the local crystal symmetry of STMO is not cubic but tetragonal, as it was reported in Ref. 211. Raman spectra<sup>114</sup> (not shown here) exhibit different phonon frequencies than IR spectra. It indicates that the structure is centrosymmetric and STMO cannot be FE at least down to 10 K.

#### 4.8 Nd substituted BiFeO<sub>3</sub> (Bi<sub>0.85</sub>Nd<sub>0.15</sub>FeO<sub>3</sub>)

BiFeO<sub>3</sub> (BFO) belongs to a class of multiferroics exhibiting simultaneously FE and AFM ordering above room temperature.<sup>216</sup> However, BFO has a limited usage due to high leakage current at room temperature and due to the spiral magnetic order which inhibit linear ME coupling.<sup>31</sup>

The scientist try to overcome the above mentioned problems by A-site substitution, especially by the rare-earth ions like La, Nd, Sm, Gd and Dy.<sup>217,115,116,218,219,220,221</sup> As dopant concentrations increase, the initial FE rhombohedral  $R3c$  structure transforms into an antiferroelectric (AFE) PbZrO<sub>3</sub>-type orthorhombic structure with  $Pbam$ <sup>221</sup> space group and then finally to a PE orthorhombic phase ( $Pbnm$ ). For details see the phase diagram of Bi<sub>1-x</sub>Nd<sub>x</sub>FeO<sub>3</sub> (BNFO) shown in Fig. 4.55. The exact symmetry of the AFE phase is still under debate. Nevertheless, it is known that all rare-earth substituted BFO samples exhibit generally similar phase diagrams with AFE morphotropic phase boundary (MPB) between FE and PE phase, where the critical concentrations depend on average ionic A-site radius.<sup>218,219</sup>

Dielectric properties (polarization, piezoelectric coefficients and complex permittivities  $\epsilon^*$ ) of rare- earth substituted BFO were investigated mainly at room temperature.<sup>218,220</sup> Only  $\epsilon^*(T)$  of BNFO ceramics ( $x=0-0.2$ ) was investigated at high-temperatures up to 400 °C.<sup>217</sup>  $\epsilon^*(T)$  measured at 100 kHz exhibits anomalies in the vicinity of structural PT, but the values of  $\epsilon^*$  are influenced by conductivity due to Maxwell-Wagner polarization. Hence, these data are considered unreliable for finding of  $T_C$ . The influence of conductivity, however, dramatically decreases with frequency and therefore high-frequency/high-temperature dielectric studies are desirable.



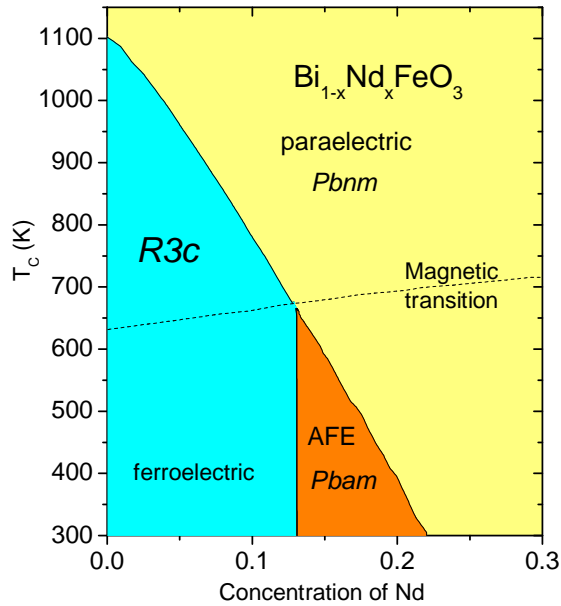


Fig.4.55. Schematic structural and magnetic phase diagram of BNFO (after Ref.221). FE  $R3c$  phase has  $Z=2$ , PE  $Pbnm$  phase  $Z=4$  and AFE  $Pbam$  phase  $Z=8$ . Electron diffraction revealed even  $Z=16$  and  $Pbnm$  structure in AFE phase. Néel temperature of G-type AFM phase increases with Nd concentration (dashed line).

Fig. 4.56 shows our experimental IR and THz reflectivity spectra of BNFO ceramics in the range of phonons, i.e. below  $650\text{ cm}^{-1}$ . The spectra at higher frequencies (up to  $3000\text{ cm}^{-1}$ ) were measured only at room temperatures, because they exhibit a frequency and temperature independent value determined by the high-frequency permittivity  $\epsilon_{\infty} = 7.3$  stemming from the electron absorption processes in the visible-UV range.

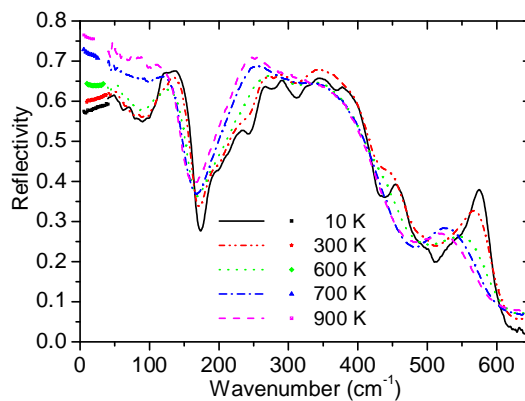


Fig.4.56. IR reflectivity spectra of BNFO at selected temperatures. Low-frequency spectra plotted below  $50\text{ cm}^{-1}$  were calculated from THz dielectric spectra using the Eq. 3.5.

For the spectra fits a generalized-oscillator model with the factorized form of the complex permittivity was used (see Eq.3.6). Experimental IR reflectivity spectra are less accurate below  $50 \text{ cm}^{-1}$ ; therefore the IR reflectivity spectra were fitted simultaneously with more reliable THz  $\varepsilon^*(\omega)$  spectra. Complex IR  $\varepsilon^*(\omega)$  spectra and  $\omega_{TOj}$  phonon frequencies obtained from the fits are shown in Figs. 4.57.

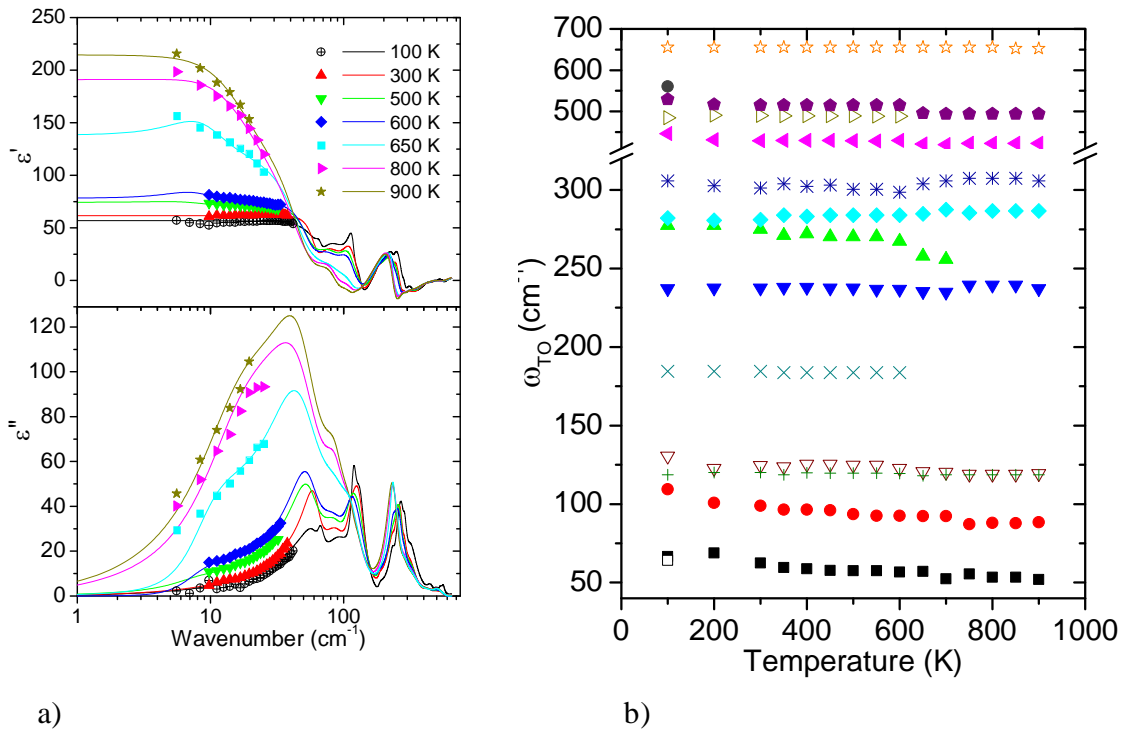


Fig.4.57. a) Complex dielectric permittivity of BNFO obtained from the fits of IR reflectivities and THz  $\varepsilon^*(\omega)$  spectra taken at selected temperatures. Symbols at low frequencies are experimental THz data; b) Temperature dependence of TO phonon frequencies obtained from the fits of THz and IR spectra. Appearance of several new phonons due to lowering of crystal symmetry below 600 K is seen.

Static permittivity can be calculated using the sum of phonon and electronic contributions (Eq. 4.4) and its temperature dependence is plotted in Fig. 4.58. Above 450 K, a heavily damped excitation appears in the spectra with relaxation frequency  $\omega_R = 8 \text{ cm}^{-1}$  and negligible dielectric strength  $\Delta\varepsilon_R=3$ . Above  $T_C \approx 600 \text{ K}$  the same excitation becomes overdamped and dielectric contribution  $\Delta\varepsilon_R$  of the relaxation dramatically increases on heating and reaches value about 90 at

900 K (see Fig. 4.58.). For the fitting of the spectra we did not use the Debye model for the relaxation

$$\varepsilon^* = \varepsilon_\infty + \frac{\Delta\varepsilon_R}{1 + i\frac{\omega}{\omega_R}} \quad (4.5)$$

because this model does not satisfy the  $f$  sum rule<sup>222</sup>

$$\int_0^\infty \omega \varepsilon''(\omega) d\omega = \text{const} \quad (4.6)$$

The Debye relaxation model gives non-zero dielectric losses at all frequencies above  $\omega_R$  and therefore  $\int_0^\infty \omega \varepsilon''(\omega) d\omega = \infty$ . Accordingly, the Debye relaxation has the influence on the fitted

theoretical IR reflectivity spectra far above  $\omega_R$ . Moreover, it is not possible to combine this model with generalized oscillator model, which is in product form (Eq. 3.6) (additionally a model of sum of oscillators (Eq. 3.8) was attempted instead of generalized-oscillator model, but the fit of reflectivity was less accurate). For the fits only generalized oscillator model was utilized and the relaxation was modeled by an oscillator with much higher damping than the eigenfrequencies.

If  $\gamma_{TO} = \gamma_{LO} > 2\omega_{TO}$  (overdamped oscillator), the relaxation frequency  $\omega_R = \frac{\omega_{TO}^2}{\gamma_{TO}}$  corresponds to the frequency of maximum of dielectric loss. In our case  $\gamma_{LO} > \gamma_{TO}$  and  $\gamma_{TO} < 2\omega_{TO}$  so that

$\omega_R \neq \frac{\omega_{TO}^2}{\gamma_{TO}}$ . Therefore, we determined  $\omega_R$  from the frequency of maxima of dielectric loss

$\varepsilon''(\omega)$  spectra, which makes better physical sense. The dielectric relaxation has a strong influence on the shape of the IR reflectivity above  $T_C$ . It dramatically enhances the value of reflectivity at low frequencies, causing the disappearance of the reflectivity minimum near  $90 \text{ cm}^{-1}$  (see Fig. 4.56) and remarkably enhances the THz permittivity and losses above  $T_C$  (see Fig. 4.57a). Temperature dependence of the relaxation frequency is plotted in the inset of Fig. 4.58.

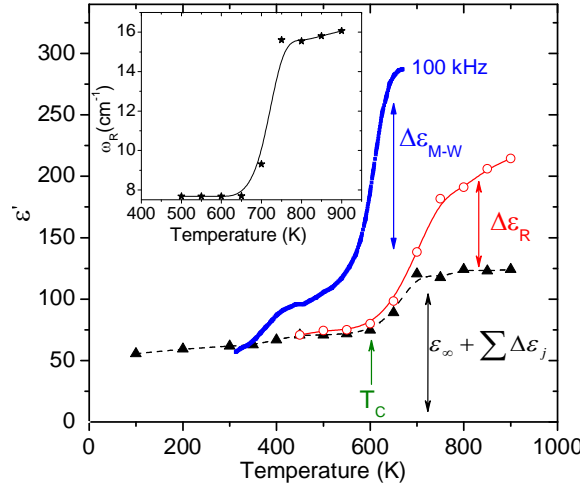


Fig.4.58 Temperature dependence of static permittivity calculated from the fits of THz and IR spectra of BNFO compared with published<sup>217</sup> 100 kHz  $\epsilon'$  data. Sum of electronic and phonon contributions ( $\epsilon_\infty + \sum \Delta\epsilon_j$ ) exhibits plateau between 700 and 900 K and drops down near  $T_C$ . Contribution  $\Delta\epsilon_R$  of the dielectric relaxation diminishes on cooling and fully disappears from the spectra below 450 K. Experimental permittivity obtained at 100 kHz<sup>217</sup> exhibits the highest value due to contribution of Maxwell-Wagner polarization. Inset shows temperature dependence of relaxation frequency  $\omega_R$  of the central (relaxational) mode.

Displacive FE PT's are driven by a polar optical SM with frequency  $\omega_{SM}$ , which softens (i.e. reduces frequency) on cooling towards  $T_C$  according to the Cochran law  $\omega_{SM}^2 = A(T - T_C)$  and hardens on further cooling below  $T_C$ .<sup>129</sup> Due to temperature conservation of the oscillator strength  $f_{SM}$  ( $f_{SM} = \Delta\epsilon_{SM}\omega_{SM}^2 = const$ ) in the case of uncoupled phonons, static permittivity exhibits the Curie-Weiss maximum at  $T_C$ . The most frequent FE PT is the order-disorder one, in which the SM is not an optical phonon but a dielectric relaxation.<sup>94,223</sup> In these cases some ions in the paraelectric phase are dynamically disordered among equivalent positions (as exemplified by Ti and Nb disorder in BaTiO<sub>3</sub> and KNbO<sub>3</sub>, respectively)<sup>224</sup> and the relaxation is a manifestation of the hopping among equivalent positions. Usually, the relaxation frequency  $\omega_R$  linearly decreases on cooling towards  $T_C$  according to a modified Cochran law  $\omega_R = A(T - T_C)$ . The strength of the dielectric relaxation defined as  $f_R = \Delta\epsilon_R\omega_R$  is usually also temperature independent above  $T_C$  and therefore  $\epsilon'$  increases on cooling towards  $T_C$ .

A common case is so called crossover between displacive and order-disorder PT.<sup>225</sup> The PT is driven by a SM which softens far above  $T_C$ , but close to  $T_C$  the SM frequency saturates and

a soft dielectric relaxation (i.e. the central mode (CM)) appears, which gains an oscillator strength from the coupling with the soft polar phonon and finally drives the FE PT. Below  $T_C$  the ions are usually ordered, i.e. the hopping of ions disappears and therefore the strength  $f_R$  dramatically decreases on cooling (actually,  $f_R$  transfers to phonons due to the  $f$  sum rule) and finally the relaxation expressing dynamical disorder of ions disappears from the spectra. Simultaneously, another dielectric relaxation related to dynamics of FE domain walls frequently appears below  $T_C$ .

AFE as well as improper-FE PT's are driven by lattice instability at the BZ boundary, which causes multiplication of unit cell below the PT.<sup>226</sup> IR and Raman spectroscopic techniques can study only phonons from the BZ centre due to conservation of  $q$  wavevectors of phonons and photons. Therefore, in the case of AFE PT the SM cannot be IR or Raman active above  $T_C$  and it may become IR and Raman active only below  $T_C$  due to folding of the BZ in the low-temperature phase. As the consequence of multiplication of unit cell below AFE or improper-FE PT, IR and Raman selection rules change and many new modes arise in the spectra below  $T_C$ .

In the case of BNFO, rather small change of number of polar phonons with temperature is observed (see Fig. 4.57b). Only five new polar modes appear below  $T_C$  due to multiplication of the unit cell (see Table I with the phonon parameters obtained from the IR spectra fits at 100 and 900 K).

Mainly the new mode (No. 8 in Table I), which appears at 700 K near  $250 \text{ cm}^{-1}$ , exhibits a remarkable hardening to  $277 \text{ cm}^{-1}$  on cooling to 100 K. Also the modes No. 1, 3, 11 and 13 exhibit significant hardening from 52, 88, 422 and  $490 \text{ cm}^{-1}$  (at 900 K) to 64, 109, 446 and  $530 \text{ cm}^{-1}$  (100 K), respectively (see Table I and Fig. 4.57b). The hardening of the all phonons is responsible for decrease of their dielectric strengths  $\Delta\epsilon_j$  and therefore also the sum of phonon contributions to  $\epsilon'(0)$  decreases below  $T_C$  in Fig. 4.58. The most remarkable influence on the shape of IR and THz spectra has the relaxation mode, which weakens on cooling and finally disappears from the spectra below  $\sim 450 \text{ K}$ . Its relaxation strength transfers to the phonons, but in spite of it the phonon contribution to  $\epsilon^*$  drops down below  $T_C$  because of phonon hardening.

Sum of phonon contributions to  $\epsilon'(0)$  is temperature independent in PE phase and it suddenly jumps down at  $T_C$ . Even stronger decrease of  $\epsilon'$  appears due to contribution of dielectric relaxation, but its dielectric strength  $\Delta\epsilon_R$  does not exhibit any saturation or peak above  $T_C$ , its

value continuously increases on heating above  $T_C$ . This unusual behavior will be discussed below.

In the case  $\text{PbZrO}_3$ , the dielectric anomaly is caused mainly by a dielectric relaxation (CM) below the phonon frequencies, but  $\varepsilon'(T)$  exhibits a peak of  $\sim 3500$  near  $T_C$  in  $\text{PbZrO}_3$  ceramics and single crystal.<sup>227,228</sup> The contribution of central mode  $\Delta\varepsilon_R$  in  $\text{PbZrO}_3$  can be drastically reduced if the ceramics exhibit cracks in such situation the peak in  $\varepsilon'(T)$  disappears, permittivity is four-times smaller and only a sharp step down occurs in  $\varepsilon'(T)$  at  $T_C$ .<sup>228</sup> The small peak in  $\varepsilon'(T)$  and a sharp drop down due to the first-order PT was observed also in hydrogen-bonded AFEs like  $\text{NH}_4\text{H}_2\text{PO}_4$  and  $\text{CsH}_2\text{AsO}_4$ .<sup>229,230</sup> Our observed continuous increase of static  $\varepsilon'(0)$  above  $T_C$  is similar to the dielectric behavior of the proton-bonded  $\text{KD}_2(\text{SeO}_3)_2$ <sup>231</sup> and  $\text{TiH}_2\text{PO}_4$ ,<sup>232</sup> but the absolute values of  $\varepsilon'$  are much smaller in these materials than in BNFO. It is worth noting that the shape of our temperature dependence of static  $\varepsilon'$  calculated from THz and IR spectra qualitatively corresponds to 100 kHz data published by Karimi et al. (see Fig. 4.58), but the latter values are higher due to contribution of Maxwell-Wagner polarization stemming from non-zero conductivity of the sample.

In Table II the factor group analysis is presented for all possible crystal structures of BNFO (Fig. 4.56) using the tables from Ref. 233. One can see that only 13 polar modes are expected in the FE  $R3c$  structure of pure BFO, while 45 or even 109 IR active modes are allowed for AFE  $Pbam$  or possible  $Pbnm$  phase with  $Z=8$  or  $Z=16$ . We have observed only 15 polar phonons in our low-temperature IR spectra (Fig. 4.58b). The probable reason is that the newly activated phonons are weak and they have frequencies close to the modes of the FE  $R3c$  structure, so that the modes become overlapped and cannot be resolved from the IR spectra.

The high-temperature IR reflectivity of BNFO differs from that of BFO mainly at low frequencies below  $150\text{ cm}^{-1}$  due to the presence of the THz dielectric relaxation. This causes disappearance of the reflectivity minimum near  $90\text{ cm}^{-1}$  in BNFO above 700 K, while in BFO the minimum is present up to the highest investigated temperature of 950 K.<sup>234</sup> Static permittivity of BFO slightly and linearly increases on heating due to small phonon softening with rising temperature, which is typical for improper-FE PT in BFO.<sup>234</sup> In BNFO the phonon  $\varepsilon'$  exhibits jump up at  $T_C$  and plateau above it. Nevertheless, contribution of dielectric relaxation grows on heating above  $T_C$  and therefore the static permittivity from the fit of THz and IR spectra also continuously increases.

Only 10 polar phonons were used for the fits of reflectivity spectra in the PE phase, although 25 IR active modes are allowed (see Table II). Again, discrepancy between the number of predicted and observed polar phonons is caused mainly by overlapping of the phonons due to the high phonon dampings at high temperatures. As a result it is impossible to distinguish all the allowed IR active phonons in the spectra.

Temperature dependence of the dielectric relaxation in PE phase is not typical for order-disorder PTs. Relaxation frequency  $\omega_R$  does not follow the modified Cochran law, i.e. it does not soften linearly on cooling towards  $T_C$  (see inset Fig. 4.58). Relaxation strength  $f_R$  is not temperature independent, but strongly decreases on cooling. This causes absence of the peak in  $\epsilon'(T)$  at  $T_C$ . The PT also does not look like the first order one, because the decrease of  $\epsilon'$  on cooling is not step-wise at  $T_C$ , but rather smooth. Broadening of the PT can be caused by an inhomogeneous concentration of Nd in BNFO ceramics.

In the PE phase the A-site cations are displaced in an antiparallel direction and coupled to the  $a^-a^+c^+$  tilting (Glazer notation<sup>136</sup>).  $T_C$  steeply decreases with Nd concentration in BNFO (Fig. 4.56) and the intermediate AFE phase ( $a^-b^-c^-/a^-b^-c^+$ ) appears in a narrow concentration range probably due to frustration between the FE and PE phase.<sup>235</sup> In other words, the driving force for polar Bi displacements becomes weaker, which results in an antipolar order. THz dielectric relaxation influences strongly the IR spectra and static  $\epsilon'$ . There are several possible explanations of the relaxation: 1) The relaxation expresses highly anharmonic (i.e. damped) rotations and tilting of oxygen octahedra in PE phase. Below  $T_C$  the relaxation disappears because the structure orders. 2) The relaxational mode is vibrations of Bi cations, which may become highly anharmonic due to a partial substitution by Nd cations. This causes dynamical disorder of A-site cations in the PE phase. Hopping of Bi and Nd cations among equivalent positions in PE phase may cause the THz relaxation. Below  $T_C$  the A-site cations order and therefore the relaxation disappears from the spectra and  $\epsilon'$  saturates at a lower value determined by the sum of phonon contributions (Fig.4.58). 3) The THz relaxation expresses hopping conductivity of oxygen vacancies and increase of its strength just at  $T_C$  is only accidental. The final decision which of the above three mechanism is correct needs additional experiments on non-conducting samples.

TABLE I. Mode parameters obtained of BNFO from the reflectivity fits at 100 and 900 K. CM means central mode.

No	100K					900K				
	$\omega_{\text{TO}}$ ( $\text{cm}^{-1}$ )	$\gamma_{\text{TO}}$ ( $\text{cm}^{-1}$ )	$\omega_{\text{LO}}$ ( $\text{cm}^{-1}$ )	$\gamma_{\text{LO}}$ ( $\text{cm}^{-1}$ )	$\Delta\epsilon$	$\omega_{\text{TO}}$ ( $\text{cm}^{-1}$ )	$\gamma_{\text{TO}}$ ( $\text{cm}^{-1}$ )	$\omega_{\text{LO}}$ ( $\text{cm}^{-1}$ )	$\gamma_{\text{LO}}$ ( $\text{cm}^{-1}$ )	$\Delta\epsilon$
C						16	27	20.1	37.1	90.2
M										
1	64	23.5	68.2	12.5	1.1	52	51.1	71.2	51.4	69
2	66.6	9.7	64.3	15.5	2.8					
3	109.4	88.6	109.6	36.8	0.6	88.3	34.2	94.6	39.5	7.8
4	118.6	14.8	166.6	17.6	13.3	119.5	79.2	119	16.4	10.3
5	130.5	26.4	123.6	17.6	13.1	118.6	17.1	156.1	32.7	9.5
6	184.5	18.0	185.0	21.9	0.08					
7	237.1	20.3	281.1	15.1	0.4	237.2	61.0	273	49.1	14.4
8	277.5	77.4	238.1	17.2	12.6					
9	282.0	17.0	304.0	34.	3.0	286.6	62.2	304.0	62.9	3.8
10	305.8	56.6	424.0	50.8	0.9	305.8	105.5	403.8	94.3	0.6
11	446.0	68.2	476.2	32.3	0.6	422.2	131.9	458.8	70.0	0.5
12	484.4	53.7	522.0	34.4	0.2					
13	529.3	25.7	544	46.7	0.06	493.6	125.0	580.6	37.4	0.8
14	560.4	31.5	599	33.3	0.2					
15	655.7	122.0	690.5	131.4	0.2	652.0	122.0	690.5	147.0	0.2



TABLE II. Factor group analysis of all vibrational modes (including acoustic) in various crystal phases of  $\text{Bi}_{1-x}\text{Nd}_x\text{FeO}_3$  shown in the phase diagram in Fig. 4.56. Activities of the modes in various kinds of spectra are shown in brackets.  $x, y, z$  mean IR active modes active in polarized  $\mathbf{E}||x$ ,  $\mathbf{E}||y$  and  $\mathbf{E}||z$  spectra, respectively. (-) means silent modes, the remaining marks mean Raman active modes.

FE: $R3c$ ( $C_{3v}^6$ )	PE: $Pbnm$ ( $D_{2h}^{16}$ )	AFE: $Pbam$ ( $D_{2h}^9$ )	AFE: $Pbnm$ ( $D_{2h}^{16}$ )
$\sqrt{2}a_c \times \sqrt{2}a_c \times a_c$	$\sqrt{2}a_c \times \sqrt{2}a_c \times 2a_c$	$\sqrt{2}a_c \times 2\sqrt{2}a_c \times 2a_c$	$\sqrt{2}a_c \times 2\sqrt{2}a_c \times 4a_c$
Z=2	Z=4	Z=8	Z=16
5 $A_1(z, x^2+y^2, z^2)$	10 $B_{1u}(z)$	12 $B_{1u}(z)$	40 $B_{1u}(z)$
	7 $A_g(x^2, y^2, z^2)$	16 $A_g(x^2, y^2, z^2)$	28 $A_g(x^2, y^2, z^2)$
10 $E(x, y, x^2-y^2, xy, xz, yz)$	8 $B_{2u}(y)$	18 $B_{2u}(y)$	32 $B_{2u}(y)$
	10 $B_{3u}(x)$	18 $B_{3u}(x)$	40 $B_{3u}(x)$
	5 $B_{1g}(xy)$	16 $B_{1g}(xy)$	20 $B_{1g}(xy)$
	7 $B_{2g}(xz)$	14 $B_{2g}(xz)$	28 $B_{2g}(xz)$
	5 $B_{3g}(yz)$	14 $B_{3g}(yz)$	20 $B_{3g}(yz)$
5 $A_2(-)$	8 $A_u(-)$	12 $A_u(-)$	32 $A_u(-)$

#### 4.9 Ba<sub>0.5</sub>Sr<sub>1.5</sub>Zn<sub>2</sub>Fe<sub>12</sub>O<sub>22</sub> with Y-type hexaferrite structure

Ba<sub>0.5</sub>Sr<sub>1.5</sub>Zn<sub>2</sub>Fe<sub>12</sub>O<sub>22</sub> (BSZFO) is a spiral ME in which spontaneous polarization was observed up to 110 K, but magnetocapacitive measurements showed that the ferroelectricity can exist up to 300 K in this material.<sup>51</sup> BSZFO exhibits distorted helimagnetic structure<sup>51,236,237</sup> below 320 K and the ferroelectricity is induced by a critical magnetic field of  $B_C=0.3-0.8$  T ( $B_C$  depends on temperature).<sup>51</sup> Chun et al.<sup>238</sup>, partially substituted Fe with Al in BSZFO and succeeded to induce FE phase already at 1 mT. From the symmetry point of view, the ferroelectricity could be  $B$ -induced already below 320 K in BSZFO, but the direct FE polarization measurement is impossible at such temperature due to a non-negligible conductivity. The aim of our studies was to investigate the magnetic and lattice dynamic properties of BSZFO ceramics and to compare them with properties of single crystal. Our results were published in Ref. 120

The Fig. 4.59 shows temperature dependence of the magnetic susceptibility (measured at 1 Hz and 100 Oe) in BSZFO ceramics. It exhibits a maximum at the magnetic PT  $T_C=312$  K. This value is very close to the critical temperature 320 K observed in single crystal.<sup>51</sup>

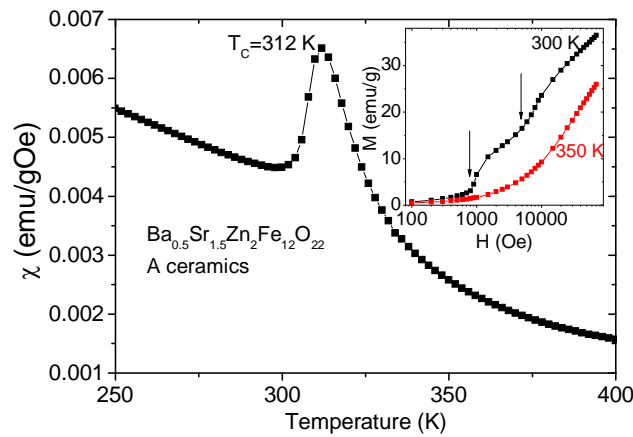


Fig4.59. Temperature dependence of magnetic susceptibility in BSZFO ceramics quickly cooled down to 300 K after sintering in air at 1373 K. Inset shows the magnetization curves at 300 and 350 K.

Curie-Weiss fit of the magnetic susceptibility  $\chi = \chi_{\infty} + \frac{C}{T - T_{\theta}}$  gives  $C=0.128$  emu K/(g

Oe)  $T_{\theta} = 291.4$  K and  $\chi_{\infty} = 3.8 \times 10^{-4}$  emu/(gOe). In the case of ideal PM phase  $\chi_{\infty}$  is zero. The positive  $\chi_{\infty}$  gives a signature of some magnetic impurities with critical temperature much above 400 K. The XRD did not detect such impurities with higher critical temperature to give this

background. Nevertheless, XRD revealed 1-2 % of  $\text{SrFeO}_{3-x}$  secondary phase, but its  $T_C$  is deeply below 300 K.<sup>239</sup> The SQUID is highly sensitive to impurities less than 1% which are not detectable in XRD so that  $\chi_\infty \neq 0$  can be caused e.g. by M-hexaferrite  $\text{Ba}_{0.5}\text{Sr}_{0.5}\text{Fe}_{12}\text{O}_{19}$  with  $T_C=670$  K.<sup>240</sup> Helicoidal magnetic structure of BSZFO exhibits several field-induce PTs with increasing  $H$ .<sup>236,51</sup> Two of them are seen in the magnetization curve of ceramics taken at 300 K (see inset of Fig. 4.59).

Three kinds of samples were analyzed: single crystals and two kinds of ceramics, which were quickly (ceramics A) and slowly (ceramics A') cooled after the sintering.

Fig.4.60 shows temperature dependence of the real and imaginary parts of index of refraction  $n^* = n + ik$  measured at 5.8 GHz for both A and A' ceramics (thickness 0.6 mm) by resonance technique. The same ceramics before polishing (i.e. thickness 1.25 mm) yield dielectric resonance at 14.2 GHz and the temperature dependences of  $n$  and  $k$  were the same in both 1.25 and 0.6 mm thick ceramics within accuracy of the measurements.

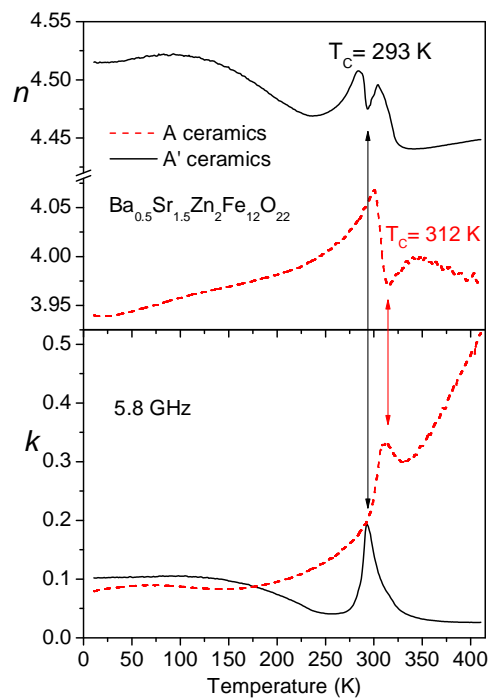


Fig.4.60. Temperature dependence of the complex refractive index components measured at 5.8 GHz in quenched A and slowly cooled A' ceramics. The magnetic PT temperatures are marked by arrows.

Temperature dependence of complex  $\varepsilon^*$  and  $\mu^*$  show usually maxima at FE and magnetic PT temperatures. In our case (Fig. 4.60) minimum in  $n(T)$  corresponds to the maximum of  $k$ .

The anomalies in  $n$  and  $k$  seen in Fig.4.60 near magnetic PT are probably caused by the frequency dispersion in  $\mu^*(T)$  because  $n^* = n + ik = \sqrt{\varepsilon^* \mu^*}$ . Drop in  $n^*(T)$  is seen about 10 K below and above  $T_C$ , so the magnon relaxation frequency lies below 5.8 GHz in the temperature interval ( $T_C - 10$ ,  $T_C + 10$ ) and above 5.8 GHz at lower or higher temperatures.  $T_C = 312$  K observed in ceramics A (Fig.4.60) exactly corresponds to  $T_C$  obtained from independent magnetic susceptibility in Fig. 4.59. Ceramics A' shows  $T_C$  by 19 K lower than ceramics A. This is most likely caused by SrFeO<sub>3-x</sub> secondary phase identified in XRD.

Kimura et al.<sup>51</sup> revealed a FE phase in BSFZO crystal induced by magnetic field  $B_{C1}$  which disappears above  $B_{C2}$ . They determined the FE phase diagram from the magnetocapacitive measurements of  $\Delta\varepsilon(B)/\varepsilon(0)$ , where  $\Delta\varepsilon(B)$  and  $\varepsilon(0)$  mark change in permittivity with the magnetic field and permittivity in zero magnetic field, respectively. Kimura et al.<sup>51</sup> also determined the magnetic field dependence of the FE polarization, which was smaller than  $150 \mu\text{C}/\text{m}^2$ . A similar investigation was done in our institute with a new single crystal, which was characterized before and after annealing in oxygen at 1100 °C. The phase diagram in Fig. 4.61 shows that the range of magnetic field, where the FE phase exists, broadens with crystal annealing. It means that  $B_{C1}$  and  $B_{C2}$  shift to lower and higher fields, respectively. Moreover, the annealed crystal can be investigated up to higher temperatures, due to lower conductivity in this sample. The same magnetocapacitive experiment was performed also on highly resistive A' ceramics, and the FE PT was also discovered. Fig.4.61 shows that the FE phase in ceramics exists in a narrower range of magnetic field (especially above 100 K) than in the crystal.  $B_{C2}$  anomaly was not revealed in ceramics above 150 K probably due to combination of high conductivity and smaller magnetocapacitance anomaly in ceramics.

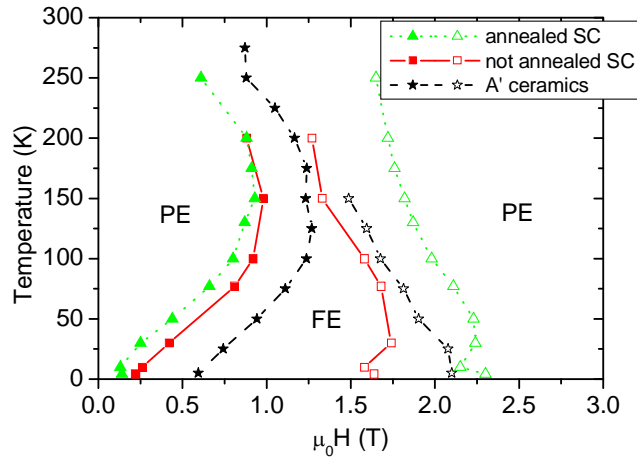


Fig.4.61. Comparison of the phase diagram in A' ceramics with the phase diagrams in single crystal (SC) before and after annealing. PE and FE mark paraelectric and ferroelectric phases, respectively.

The relatively high conductivity of the samples prevented us to see any magnetocapacitance anomaly (i.e. the FE PT) at room temperature. Therefore we used the spectroscopic methods which are highly sensitive to the change of the crystal symmetry. In the FE phase, the optical phonons should be both Raman and IR active, while in the PE phase the Raman active modes are not IR active. In Fig. 4.62, IR reflectivity spectra of single crystal and ceramics taken at 300 K and 10 K are shown. The crystal had small dimensions in the  $c$  direction, therefore the  $\mathbf{E}||c$  spectrum was taken only at room temperature. The intensity of reflection bands increases on cooling due to the usual decrease in phonon damping, but no phonons disappear from the spectra on cooling. Disappearance would be expected in the case of re-entrant PT from FE to PE phase. The number of polar phonons remains the same at all temperatures, in both crystal and ceramics, so we do not see any evidence for a structural PT on cooling down to 10 K (at  $B=0$  T). In other words, the samples seem to remain PE at all temperatures, if  $B=0$  T.

At room temperature we tried to reveal the magnetic field induced FE PT in the IR reflectivity spectra. A static magnetic field of 1 T along  $c$  crystal axis or 0.3 T parallel to  $a$  axis was applied. No qualitative differences were observed in IR spectra of both ceramics and crystal with and without magnetic field. Magnetic field higher than 0.3 T with  $\mathbf{B}\perp c$  is probably necessary for invoking the FE order at 300 K. Note that the strength of new IR active modes in the FE phase should be proportional to the square of order parameter<sup>94</sup> and because the spontaneous polarization is several orders of magnitude lower in BSZFO than in the classical FEs and the

relative change in lattice constant<sup>241</sup> is only  $10^{-5}$ , the intensity of the newly activated modes could be much lower than in other FEs.

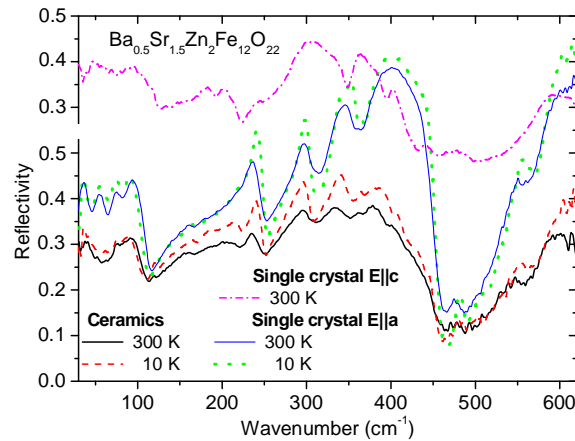


Fig.4.62 IR reflectivity of single crystal and ceramics at 300 K and 10 K. A change in scale for  $E||c$  polarized spectrum was used. Spurious oscillations below  $80\text{ cm}^{-1}$  in the  $E||a$  spectra of single crystal are caused by a diffraction of the IR beam on the small sample.

In order to see some change in crystal symmetry, Raman spectra were measured in our Institute as well. Again like in the IR spectra, no phonons disappear on cooling, only phonon damping reduces, which results in sharper lines at low temperatures. It gives no evidence for structural PT in BSZFO ceramics and single crystal measured on cooling in  $B=0\text{ T}$ . The samples remain in the PE phase at all temperatures at  $B=0\text{ T}$ . Additionally, our factor group analysis confirms that the number of phonons observed in IR and Raman spectra corresponds to PE hexagonal phase. It can be concluded that no evidence for ferroelectricity was observed in the Raman and IR spectra either on cooling (at  $B=0$ ) or after application of external magnetic field at 300 K. We found the FE phase only in external magnetic field using the magnetocapacitive measurements (see the phase diagram in Fig. 4.61).

Another interesting effect in this kind of material is the possibility of existence of electromagnons. Recently, an electromagnon was observed in Y-type hexaferrite  $\text{Ba}_2\text{Mg}_2\text{Fe}_{12}\text{O}_{22}$  with longitudinal spin conical-spin structure.<sup>166</sup> This electromagnon was observed already in PE phase below  $\sim 100\text{ K}$  and its intensity just increased with external magnetic field inducing the FE phase.<sup>166</sup> Under such circumstances, one can expect that the electromagnon can be activated also in BSZFO. From that reason THz spectra of these compounds were investigated in our Institute.

Fig. 4.63 shows experimental spectra of refractive index in THz frequency range together with damped oscillator fit of both THz and IR spectra (from Fig.4. 62).

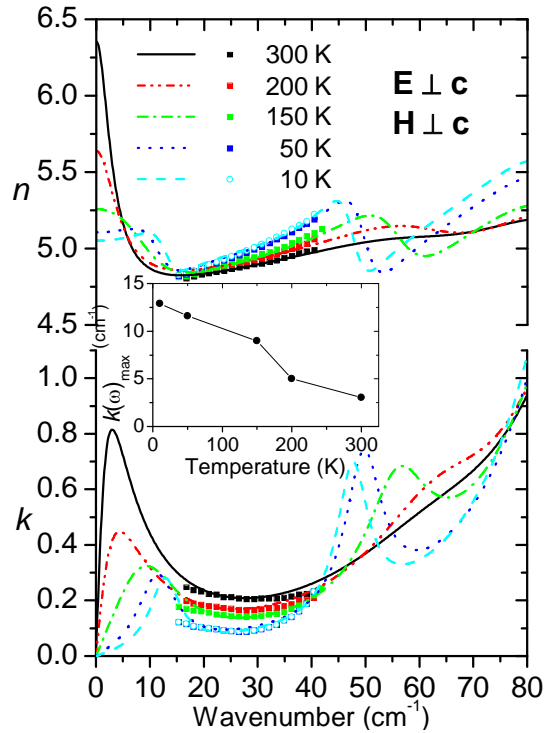


Fig.4.63. Temperature dependence of the experimental THz spectra (symbols) of the real and imaginary parts of index of refraction together with the damped oscillator fit (lines) of THz and IR spectra of BSZFO crystal. Electric  $\mathbf{E}$  and magnetic ( $\mathbf{H}$ ) vectors of the THz beam are polarized perpendicular to the  $c$  crystal axis. Inset shows temperature dependence of frequency of the peak in extinction coefficient  $k(\omega)$ .

One can see that some new excitation near  $50 \text{ cm}^{-1}$  develops on cooling. Similar mode was observed in  $\text{Ba}_2\text{Mg}_2\text{Fe}_{12}\text{O}_{22}$  near  $64 \text{ cm}^{-1}$  and Kida et al<sup>166</sup> claimed, based on detailed analysis of their polarized THz spectra, that this excitation contributes only to  $\epsilon'$  (not  $\mu'$ ), so it is a phonon or electromagnon. Kida et al did not report any temperature or magnetic field dependence of this excitation, but our experiments show a heavily damped mode at room temperature which becomes underdamped on cooling. Moreover, its frequency remarkably softens on cooling. The data are insufficient for distinguishing of phonon or electromagnon origin of this mode. New data on single crystal with polarization  $\mathbf{E}||c$  are necessary. An interesting behavior is seen in the THz spectra below  $30 \text{ cm}^{-1}$  (Fig.4.63) where the saturation or even increase in extinction coefficient  $k$  is seen on decreasing frequency. Intrinsic dielectric loss  $\epsilon''$  in classical dielectrics should have a

completely different behavior. It should be proportional to frequency ( $\varepsilon''(\omega) \propto \omega$ ) below phonon frequencies, because it originates from multiphonon absorption.<sup>94</sup> It means that  $\varepsilon''(\omega)$  (or  $k(\omega)$ ) should decrease to zero at low frequencies. The observed enhanced  $k$  gives us evidence about an additional absorption contribution.

Extrinsic absorption is not probable. MW data (Fig.4.60) revealed that magnetic susceptibility spectrum exhibits a critical relaxation, which has relaxation frequency of 5.8 GHz at  $T_C - 10$  K (Fig.4.60). The  $\omega_R$  increases on cooling below  $T_C$  (as well as on heating above  $T_C$ ) and its strength in the spectra should decrease. This is exactly seen in our THz spectra (Fig.4.63). To fit the relaxation in the THz spectra we used an overdamped harmonic oscillator (Eq. 3.8).<sup>94</sup> The relaxation frequency corresponds to frequency of maxima in  $k(\omega)$  spectra. Its temperature dependence is seen in inset of Fig.4.63. The strength of the relaxation decreases on cooling but it does not disappear down to 10 K. This excitation has probably origin in a spin wave. Unfortunately, it cannot be determined whether it gives dispersion to  $\varepsilon^*(\omega)$  (electromagnon) or  $\mu^*(\omega)$  (magnon), because the (0001) BSZFO crystal plate does not allow us to perform a THz experiment with polarization  $\mathbf{E} \parallel \mathbf{c}$  or  $\mathbf{H} \parallel \mathbf{c}$ . Magnetic resonance lies in microwave region near  $T_C$  and the electromagnon can be active only in  $\mathbf{E} \parallel \mathbf{c}$  spectra.<sup>166</sup> Based on all these facts, it is assumed that below  $20 \text{ cm}^{-1}$  we see probably a pure magnetic dispersion in  $\mu^*(\omega)$ , i.e. the excitation is a magnon. Its frequency corresponding to  $k(\omega)$  maximum (see inset in Fig. 4.63) increases on cooling and reaches  $13 \text{ cm}^{-1}$  (390 GHz) at 10 K. This value has a rather large error, because just the high frequency wing of this absorption is seen, but qualitatively it is clear that some magnetic absorption exists below the THz frequency range. Note that Talbayev et al.<sup>242</sup> investigated BSZFO using time-domain pump-probe reflectance spectroscopy and detected coherent magnons near 50 GHz ( $\sim 2 \text{ cm}^{-1}$ ) at 10 K.

The THz spectra of A' ceramics have qualitatively similar behavior as in Fig.4.63, only the absolute value of index of refraction was lower due to 30% porosity of the ceramics. THz spectra of single crystal were observed both before and after annealing and no change was observed. So the magnon properties are not sensitive to sample annealing.



## Chapter 5 Conclusions

In this work we have analyzed the lattice dynamics, dielectric and magnetic properties of some selected multiferroic and magnetoelectric materials.

Using the IR reflectivity spectroscopy, we investigated the phonon behavior in a broad temperature range. We focused mainly on the soft optical modes which drive the displacive ferroelectric phase transitions.

In bulk  $\text{EuTiO}_3$  single crystal and ceramics we discovered an antiferrodistortive phase transition around 300 K. The cubic  $Pm\bar{3}m$  phase becomes tetragonal  $I4/mcm$  below room temperature. Simultaneously we found a large anisotropy in magnetocapacitance  $\Delta\epsilon(B)/\epsilon(0)$  data, which we explained by anisotropy of the tetragonal phase. Also, we have demonstrated that the incipient-ferroelectric temperature dependence of  $\epsilon'$  observed in the paramagnetic phase of  $\text{EuTiO}_3$ , is due to the TO1 phonon softening. We have determined, based on the analysis of mode plasma frequencies, that the soft TO1 phonon is so called Slater mode, i.e. it includes Ti vibrations against the  $\text{O}_6$ -octahedra. TO2 mode seen near  $150 \text{ cm}^{-1}$  is so called Last mode which involves the Eu vibrations against the the  $\text{TiO}_6$  octahedra. Both TO1 and TO2 modes are coupled; therefore the soft mode frequency is strongly influenced by antiferromagnetic order of spins in Eu positions.

The main results were obtained on strained  $\text{EuTiO}_3$  thin films. Tensile strained  $\text{EuTiO}_3$  thin film deposited on  $\text{DyScO}_3$  becomes ferroelectric below 250 K, which was demonstrated by the temperature dependence of the soft mode. At low temperatures (below 4.2 K) the film becomes ferromagnetic, although the bulk  $\text{EuTiO}_3$  is antiferromagnetic. In this case we have demonstrated a new route how to prepare new multiferroics with a strong magnetoelectric effect – just using the strain in the materials exhibiting a strong spin-phonon coupling.

In compressively strained films the strain was not high enough for inducing the ferroelectric phase. Nevertheless, the stiffened phonons showed so low damping, that we were able to measure the dependence of the lowest phonon frequency on magnetic field. In such a way we have demonstrated that the magnetodielectric effect in  $\text{EuTiO}_3$  is caused by a shift of polar phonon frequencies with magnetic field. It is so far unique result in the literature, up to now mainly tuning of polar phonons by external electric field was observed.

We have taken active part in the suggestion to use multiferroic  $\text{Eu}_{0.5}\text{Ba}_{0.5}\text{TiO}_3$  and  $\text{Eu}_{0.5}\text{Ba}_{0.25}\text{Sr}_{0.25}\text{TiO}_3$  ceramics for the search of permanent electric dipole moment (EDM) of the electron. Here we have described briefly the method of measuring the EDM and its importance for development of new particle theories which will go beyond Standard model of particles. We have also investigated the magnetic and dielectric properties of these new multiferroics and from IR spectra we have determined that they exhibit displacive ferroelectric phase transitions.

In the bulk  $\text{YMnO}_3$  ceramics we have confirmed that the ferroelectric phase transition above 900 K is an improper one. This is in agreement with the first principle calculations. In  $\text{YMnO}_3$  single crystal we have discovered new broad polar excitations in the frequency range 40-100  $\text{cm}^{-1}$ . These are not phonons and because they lie in the range of magnons and contribute to dielectric permittivity, they remind electromagnons. However, their temperature dependence is completely different and we have explained them by magnon-phonon and multiphonon absorption. Such multiparticle excitations seem to be rather common in multiferroics, but were never assigned.

In hexagonal  $\text{InMnO}_3$  we did not find any ferroelectric phase transition up to 900 K, although it was previously reported. Also  $\text{Sr}_2\text{TiMnO}_6$  does not exhibit any ferroelectric or structural phase transition below 900 K.

In the case of  $\text{Bi}_{0.85}\text{Nd}_{0.15}\text{FeO}_3$  ceramics we have characterized the phonon behavior obtained from the IR and THz spectra.  $\text{Bi}_{0.85}\text{Nd}_{0.15}\text{FeO}_3$  undergoes an antiferroelectric phase transition around 600 K, which is manifested by a step-like decrease of permittivity at  $T_C$ . We found an unusually strong THz dielectric relaxation above  $T_C$ , and several explanations for it were suggested. We characterized Y-type hexaferrite  $\text{Ba}_{0.5}\text{Sr}_{1.5}\text{Zn}_2\text{Fe}_{12}\text{O}_{22}$  ceramics and compared their dielectric and magnetic properties with those of single crystal. The magnetic phase transition was revealed not only in magnetic susceptibility data, but also in microwave data. We determined the ferroelectric phase diagram in  $\text{Ba}_{0.5}\text{Sr}_{1.5}\text{Zn}_2\text{Fe}_{12}\text{O}_{22}$  ceramics and single crystal and have shown that the sample annealing in oxygen has positive influence on broadening of the ferroelectric phase region. Spin-wave excitations were identified in the THz and IR reflectivity spectra. However, no evidence for a structural phase transition was found in our IR and Raman spectra on cooling nor at room temperature with an external static magnetic field up to 0.3 T.

---

## Bibliography:

- <sup>1</sup> Röntgen W. C. 1888, Ann. Phys. **35**, 264;
- <sup>2</sup> Wilson H. A. 1905, Phil. Trans. R. Soc. A **204**, 129 ;
- <sup>3</sup> Curie P. 1894 J. Physique **3**, 393;
- <sup>4</sup> Landau L. D. and Lifshitz E. M. 1960 Electrodynamics of Continuous Media (Oxford Pergamon);
- <sup>5</sup> Dzyaloshinskii I.E. 1959, Sov. Phys.-JETP **10**, 628;
- <sup>6</sup> Astrov D. N 1960 Sov. Phys. – JETP **11** 708 ;
- <sup>7</sup> Astrov D. N. 1961 Sov. Phys.-JETP **13** 729;
- <sup>8</sup> Rado G. T. and Folen V J 1961 Phys. Rev. Lett. **7**, 310;
- <sup>9</sup> Folen V.J., Rado G. T. and Stalder E. W. 1961 Phys. Rev. Lett **6** 607;
- <sup>10</sup> Indenbom V.L., Kristallografiya, **5**, 513(1960);
- <sup>11</sup> Bhagaivantam S., Crystal Symmetry and Physical properties, Academic Press, London- New-York, 1966;
- <sup>12</sup> Birss R. P., Symmetry and magnetism, North-Holland, Amsterdam (1966);
- <sup>13</sup> Siratori K et al., Acta Physica Polonica, **A81**, 431(1992);
- <sup>14</sup> Rivera J. P. 1993, Ferroelectrics **161** 65;
- <sup>15</sup> Krichevtsov B. B. Pavlov V V and Pisarev R V 1989 JETP Lett. **49**, 535;
- <sup>16</sup> Rado G T., Ferrari J. M. and Maisch W. G. 1984 Phys. Rev. B **29**, 4041;
- <sup>17</sup> Schmidt H., Ferroelectrics, 1994, **162**, 317;
- <sup>18</sup> Smolenskii G. A., Agronovskaya A. I. and Isupov V.A. 1959 Sov. Phys.-Solid State **1**, 149
- <sup>19</sup> Smolenskii G.A. and Chupis I. E, 1982 Sov. Phys.-Usp, **25**, 475 ;
- <sup>20</sup> Kimura T et al., 2003, Nature, **426**, 55 ;
- <sup>21</sup> Goto T. et al. 2004, Phys. Rev. Lett., **92**, 257201;
- <sup>22</sup> Fiebig M. J. 2005, J. Phys. D: Appl. Phys., **38**, R123;
- <sup>23</sup> Brown W.F. Jr. et al. 1968, Phys. Rev., **168**, 574;
- <sup>24</sup> Khomskii D., 2009, Physics, **2**, 20;
- <sup>25</sup> Hill N.A. 2000, J. Phys. Chem. B, **104**, 6694;
- <sup>26</sup> Hill N.A. et al., 2002, J. Magn. Magn. Mater., **242-245**, 976;
- <sup>27</sup> Hill N.A. et al., 2002, J. Phys. Chem B **106**, 3383;
- <sup>28</sup> Hill N.A et al., 1999, Phys. Rev. B. **59**, 8759;
- <sup>29</sup> Neaton J. et al., 2005, Phys. Rev. B, **71**, 014113 ;
- <sup>30</sup> Kiselev S.V. et al., 1963, Sov. Phys. Dokl., **7**, 742;
- <sup>31</sup> Sosnowska I et al., 1982, J. Phys. C, **15**, 4835;
- <sup>32</sup> Wang J. et al., 2003, Science, **299**, 1719;
- <sup>33</sup> Tokunaga M. et al., 2010, J. Phys. Soc. Jap, **79**, 064713 ;
- <sup>34</sup> Efremov D. V. et al., 2004, Nature Mater., **3**, 853;
- <sup>35</sup> Ikeda N et al., 2005, Nature, **436**, 1136;
- <sup>36</sup> Verwey E. J. W. & Haayman P. W. 1941, Physica, **8**, 879;
- <sup>37</sup> van Aken B. B. et al., 2004, Nature Mater, **3**, 164;
- <sup>38</sup> Aikawa Y. et al., 2005, Phys. Rev. B, **71**, 184418 ;
- <sup>39</sup> Scott J.F. et al., 2011, J. Phys.: Condens. Matter **23**, 113202;
- <sup>40</sup> Ascher E. et al., 1964, Solid State Commun., **2**, 45;
- <sup>41</sup> Schmid H et al., 1965, Solid State Commun., **3**, 327 ;

- 
- <sup>42</sup> Cheong S.-W & Mostovoy M, 2007, *Nature Mater.*, **6**, 13;
- <sup>43</sup> Toledano P. 2009, *Phys. Rev. B*, **79**, 094416 ;
- <sup>44</sup> Kajimoto K. et al., 2004, *Phys. Rev. B*, **70**, 012401;
- <sup>45</sup> Kenzelmann M. et al., 2005, *Phys. Rev. Lett.*, **95**, 087206;
- <sup>46</sup> Kimura T. et al., 2005, *Phys. Rev. B*, **71**, 224425 ;
- <sup>47</sup> Katsura H et al., 2005, *Phys. Rev. Lett*, **95**, 057205;
- <sup>48</sup> Mostovoy M., 2006, *Phys. Rev. Lett*, **96**, 067601;
- <sup>49</sup> Stremper J. et al., 2007, *Phys. Rev. B*, **75**, 212402;
- <sup>50</sup> Lawes G. et al., 2005, *Phys. Rev. Lett*, **95**, 087205 ;
- <sup>51</sup> Kimura. T. et al. 2005, *Phys. Rev. Lett*. **94**, 137201;
- <sup>52</sup> Ficher M. et al., 1980, *Phys. Rev. Lett.*, **44**, 1502 ;
- <sup>53</sup> Choi I. J. et al., 2008, *Phys. Rev. Lett.*, **100**, 047601 ;
- <sup>54</sup> Hur N et al., 2004, *Nature*, **429**, 392 ;
- <sup>55</sup> Fennie C., 2008, *Phys. Rev. Lett*, **100**, 167203;
- <sup>56</sup> Varga T et al., 2009, **103**, 0476011;
- <sup>57</sup> Fox D.L. and Scott J.F. 1977, *J. Phys. C: Solid State Phys.* **10**, L329
- <sup>58</sup> Dubovnik V.M. & Tugushev V.V. 1990, *Phys. Rep.*, **187**, 145
- <sup>59</sup> Zel'dovich Ya. B., 1957, *Zh. Eksp. Teor. Fiz.* **33**, 1531; [*Sov. Phys.*, *JETP*, **6**, 1184 (19580)]
- <sup>60</sup> Ginzburg V.L. et al., 1984, *Solid State Commun.*, **50**, 339;
- <sup>61</sup> Schmid H., 2001, *Ferroelectrics*, **22**, 41;
- <sup>62</sup> Van Aken B.B. et al., 2007, *Nature*, **449**, 702;
- <sup>63</sup> Jung J.H. et al., 2004, *Phys. Rev. Lett*, **93**, 037403;
- <sup>64</sup> Arima T., 2005, *J. Phys. Soc. Jpn*, **74**, 1419;
- <sup>65</sup> Kornev I et al., 2000, *Phys. Rev. B*, **62**, 2247;
- <sup>66</sup> Nan Ce-Wen et al., 2008, *J. Appl. Phys.* **103**, 031101 ;
- <sup>67</sup> Scott J. F., 2007, *Nature Mater.* **6**, 256;
- <sup>68</sup> Ramesh R & Spaldin N., 2007, **6**, 21;
- <sup>69</sup> Fujimura N et al., 1996, *Appl. Phys. Lett.*, **69**, 1011 ;
- <sup>70</sup> Gajek M. et al., 2002, *Phys. Rev. B*, **66**, 064425;
- <sup>71</sup> Son J.Y. et al., 2004, *Appl. Phys. Lett.*, **84**, 4971;
- <sup>72</sup> Murakami M. et al., 2006, *Appl. Phys. Lett.*, **88**, 152902;
- <sup>73</sup> Kumar A. et al., 2007, *Phys. Rev. B*, **75**, 060101(R);
- <sup>74</sup> Haeni J. H. et al., 2004, *Nature*, **430**, 758;
- <sup>75</sup> Zheng H. et al., 2004, *Science*, **303**, 661;
- <sup>76</sup> Bibes M. and Barthelemy A. 2008, *Nature Materials*, **7**, 425;
- <sup>77</sup> Zhou L. et al. 2004, *Phys. Status. Solidi A*, **201**, 497 ;
- <sup>78</sup> <http://www.chembio.uoguelph.ca/educmat/chm729/phonons/vector.htm>
- <sup>79</sup> Bruesch P., 1987, *Phonons: Theory and Experiments I*, Springer-Verlag Berlin;
- <sup>80</sup> M.E. Lines and A.M. Glass, 1977, *Principles and application of ferroelectrics and related materials*, Clarendon Press, Oxford;
- <sup>81</sup> Gervais F., Chapter 7 *High-Temperature Infrared Reflectivity Spectroscopy by Scanning Interferometer* of vol.8 *Infrared and Milimeter Waves*, Edited by Kenneth J. Button, Academic Press, 1983;
- <sup>82</sup> Lyddane L.H. et al., 1941, *Phys. Rev.*, **59**, 673;
- <sup>83</sup> Rabe K et al., *Physics of Ferroelectrics (A Modern Perspective)*, Springer- Verlag, 2007, available online at SpringerLink.com

- 
- <sup>84</sup> Kittel Ch. Introduction to Solid State Physics, 8<sup>th</sup> Edition;
- <sup>85</sup> Kingery W.D., Bowen H.K. and D.R. Uhlmann, Introduction to ceramics, 2<sup>nd</sup> ed., John Wiley & Sons, 1976;
- <sup>86</sup> Bruesch P., Phonons: Theory and Experiments III, Springer-Verlag Berlin, 1987
- <sup>87</sup> Petzelt J., Kamba S. and Hlinka J., New Developments in Advanced Functional Ceramics- Chapter 14, 2007, 387-421, ISBN:81-7895-248-3;
- <sup>88</sup> <http://www.answers.com/topic/magnon>;
- <sup>89</sup> Blundell St., 2001, Magnetism in Condensed matter, Oxford Master Series in Condensed Master Physics, Oxford University Press Inc. New York;
- <sup>90</sup> Brinkman W. et al., 1967, J. Appl. Phys., **38**, 939;
- <sup>91</sup> Brinkman W. and Elliott R.J., 1966, J. Appl. Phys., **37**, 1457
- <sup>92</sup> Brüesch P, Phonons: Theory and Experiments II, Springer-Verlag Berlin Heidelberg 1986
- <sup>93</sup> Bell, R.J. (1972). Introductory Fourier Transform Spectroscopy. New York: Academic Press
- <sup>94</sup> Petzelt J. et al., 1987, Ferroelectrics, **73**, 101;
- <sup>95</sup> Barker A.S. et al., 1964, Phys. Rev., **135**, A1732;
- <sup>96</sup> Železný V. et al., 1998, Czechoslovak Journal of Physics, **48**, 537;
- <sup>97</sup> Hwang J.S. 2007, Research Express, **1**, 9-13;
- <sup>98</sup> Rubens H. et al., 1893, Philosophical Magazines Series 5, **35**, 35-45 ;
- <sup>99</sup> Kimmitt M.F., 2003, Journal of Biological Physics, **29**, 77-85;
- <sup>100</sup> Born M and Wolf E., Principles of Optics: Electromagnetic theory of Propagation, Interface and Diffraction of Light, Cambridge University Press, 7<sup>th</sup> Edition, October 1999, ISBN 0521642221
- <sup>101</sup> William G.P., 2004, Philosophical Transaction: Mathematical, Physical and Engineering Sciences, **362**, 403-414;
- <sup>102</sup> Coherent Inc Stabilized integrated FIR (THz) laser system, March 2007 URL [https://www.coherent.com/downloads/SIFIR50\\_DSrevB.pdf](https://www.coherent.com/downloads/SIFIR50_DSrevB.pdf);
- <sup>103</sup> Winnerl S. et al., 2008, IEEE Journal of Selected Topics in Quantum Electronics **14(2)**, 449-457;
- <sup>104</sup> Auston D.H. et al., 1988, Journal of Quantum Electronics, **24**, 184-197 ;
- <sup>105</sup> Nahata A. et al., 1996, Appl. Phys. Lett, **69**, 2321-2323;
- <sup>106</sup> Fattinger C. et al., 1988, Applied Physics Letters, 53(16), 1480-1482;
- <sup>107</sup> Kuzel P. et al, 2000, Ferroelectrics, **239**, 79-86;
- <sup>108</sup> <http://www.ptb.de/cms/en/fachabteilungen/abt2/fb-24/ag-245/forschung-245.html>
- <sup>109</sup> <http://www.qdusa.com/sitedocs/appNotes/mpms/FundPrimer.pdf>;
- <sup>110</sup> Prokleska J. et al. private communication;
- <sup>111</sup> Kachlik et al., 2011, submitted to Materials Letters;
- <sup>112</sup> Belik A. et al, 2009, Phys. Rev. B, **79**, 054411;
- <sup>113</sup> Søndena R et al., 2006, Phys. Rev. B, **74**, 144102;
- <sup>114</sup> Meher Preethi K.R.S. et al., 2010, J. Appl. Phys., **108**, 094108;
- <sup>115</sup> Karimi S et al., 2009, Appl. Phys. Lett., **94**, 112903;
- <sup>116</sup> Karimi S. et al., 2009, J. Mater. Sci., **44**, 5102;
- <sup>117</sup> Ferreira W.S. et al., 2009, Phys. Rev. B, **79**, 054303;
- <sup>118</sup> Yamagichi H et al., 2000, Ferrites: Proceedings of the Eighth International Conference on Ferrites (ICF 8) Kyoto and Tokyo, Japan
- <sup>119</sup> Momozawa N et al., 1993, J. Phys. Soc. Jpn., **62**, 1292;

- 
- <sup>120</sup> Kamba S. et al., 2010, J. Appl. Phys., **107**, 104109;  
<sup>121</sup> McGuire T.R. et al., 1966, J. Appl. Phys., **37**, 981 ;  
<sup>122</sup> Katsufuji T & Takagi H., 2001, Phys. Rev. B, **64**, 054415 ;  
<sup>123</sup> van Mechelen J.L.M et al., 2011, PRL, **106**, 217601;  
<sup>124</sup> Bussmann-Holder A. et al., 2011, Phys. Rev. B, **83**, 212102;  
<sup>125</sup> Jiang Q et al, 2003, J. Appl. Phys., **93**, 2121;  
<sup>126</sup> Brous J. et al., 1953, Acta Crystallogr., **6**, 67 ;  
<sup>127</sup> Shafer M.W. et al., 1965, J. Appl. Phys., **36**, 1145;  
<sup>128</sup> Goian V. et al, 2009, E PJB, **71**, 429;  
<sup>129</sup> Cochran W., 1959, Phys. Rev. Lett., **3**, 412  
<sup>130</sup> Barrett J.H., 1952, Phys. Rev., **86**, 118;  
<sup>131</sup> Hlinka J et al., 2006, Phase Transitions, **79**, 41;  
<sup>132</sup> Zhong W et al., 2004, Phys. Rev. Lett., **72**, 3618;  
<sup>133</sup> Fennie C. and Rabe K., 2006, PRL, **97**, 267602;  
<sup>134</sup> Akamatsu H. et al., 2011, **83**, 214421;  
<sup>135</sup> Rushchanskii K. and Lezaic M., private communications;  
<sup>136</sup> Glazer A. M., 1972, Acta Cryst. **B28**, 3384;  
<sup>137</sup> Rushchanskii K. et al., 2010, Nat. Mater., **9**, 649;  
<sup>138</sup> Purcell E.M. et al., 1950, Phys. Rev., **78**, 807;  
<sup>139</sup> Khriplovich I B and Lamoreaux S K 1997 Springer CP Violation without Strangeness;  
<sup>140</sup> McGuire T R et al, 1966, J. Appl. Phys. **37**, 981  
<sup>141</sup> Goian V. et al, 2011, J. Phys. : Condens. Matter., **23**, 025904 ;  
<sup>142</sup> Hlinka J. Et al., 2008, Phys. Rev. Lett., **101**, 167402;  
<sup>143</sup> Barker A.S. et al, 1975, Rev. of Mod. Phys., **47**, S1;  
<sup>144</sup> Lee J.-H. et al., 2010, Nature, **466**, 954;  
<sup>145</sup> Kugimiya K. et al., 2007, JMMM, **310**, 2268;  
<sup>146</sup> Fujita K. et al, 2009, Appl. Phys. Lett., **94**, 062512;  
<sup>147</sup> Lee J-H et al., 2009, Appl. Phys. Lett., **94**, 212509;  
<sup>148</sup> Kamba et al., 2007, Europhys. Lett., **80**, 27002;  
<sup>149</sup> Kamba S et al., 1995, Phys. Rev. B, **51**, 14998;  
<sup>150</sup> Fleury P.A. et al, 1968, Phys. Rev. Lett., **21**, 16;  
<sup>151</sup> Nuzhnyy D. et al., 2009, Appl. Phys. Lett., **95**, 232902;  
<sup>152</sup> Wang K.F. et al., 2009, Advanced in Physics, **58**, 321;  
<sup>153</sup> Abrahams S.C. et al., 1968, Phys. Rev., **172**, 551;  
<sup>154</sup> Lee J-H. et al, 2011, Addendum Nature, **476**, 114;  
<sup>155</sup> Schlom D.G. et al., 2007, Annu. Rev. Mater. Res. **37**, 589;  
<sup>156</sup> Nuzhnyy D. et al., 2009, Journal of Electroceramics, **22**, 297;  
<sup>157</sup> Ruf. T et al., 1988, Phys. Rev. B, **38**, 11985 ;  
<sup>158</sup> Pimenov A. Et al., 2006, Phys. Rev. B, **74**, 100403(R);  
<sup>159</sup> Skoromets V. et al., 2010, J. Appl. Phys. **107**, 124116;  
<sup>160</sup> Nuzhnyy D. et al., 2011, J. Phys.:Condens. Matter., **23**, 045901 ;  
<sup>161</sup> Pimenov A. et al., 2006, Nature Phys., **2**, 100;  
<sup>162</sup> Sushkov A. B. et al., 2007, Phys. Rev. Lett., **98**, 027202;  
<sup>163</sup> Baryakhtar V.G. et al., 1970, Sov. Phys.-Solid State, **11**, 2628;  
<sup>164</sup> Pimenov A. et al., 2008, J. Phys.: Condens. Matter., **20**, 434209;  
<sup>165</sup> Shuvaev A. M. et al., 2011, J. Phys.:Condens. Matter., **23**, 113201;

- 
- <sup>166</sup> Kida N. et al., 2009, Phys. Rev. B., **80**, 220406®;  
<sup>167</sup> Lee J.S. et al, 2009, Phys. Rev. B., **79**, 180403®;  
<sup>168</sup> Valdes Aguilar R. et al., 2009, Phys. Rev. Lett., **102**, 047203;  
<sup>169</sup> Kida N et al., 2009, J. Opt. Soc. Am. B, **26**, A35  
<sup>170</sup> Shuvaev A.M. et al., 2011, J. Phys.:Condens. Matter., **23** 113201,  
<sup>171</sup> Mochizuki M. et al., 2010, Phys. Rev. Lett., **104**, 177206;  
<sup>172</sup> Cazayou M. et al., 2008, Phys. Rev. Lett, **101**, 037601;  
<sup>173</sup> Komandin G. et al., 2010, Phys. Sol.State, **52**, 734;  
<sup>174</sup> Talbayev D. et al., 2011, Phys. Rev. B, **83**, 094403;  
<sup>175</sup> Gibbs A.S. et al., 2011, Phys. Rev. B, **83**, 094111;  
<sup>176</sup> Bertaut E. and Mercier M., 1963, Phys. Lett., **5**, 27;  
<sup>177</sup> Chatterji T. et al., 2007, Phys. Rev. B, **76**, 144406;  
<sup>178</sup> Lukaszewicz K. et al., 1974, Ferroelectrics, **7**, 81;  
<sup>179</sup> Abrahams S.C. et al., 2001, Acta Crystallogr.Sect. B: Struct. Sci. , **57**, 485;  
<sup>180</sup> Smolenskii G.A. et al., 1964, J. Appl. Phys., **35**,915;  
<sup>181</sup> Fiebig M. et al., 2000, Phys. Rev. Lett., **84**, 5620;  
<sup>182</sup> Fiebig M. et al., 2004, Nature, **419**, 818;  
<sup>183</sup> Goltsev A.V. et al, 2003, Phys. Rev. Lett, **90**, 177204;  
<sup>184</sup> Zaghrioui M. et al., 2008, Phys. Rev. B, **78**, 184305;  
<sup>185</sup> Nenert G. et al., 2007, J. Phys.: Condens. Matter., **19**, 466212;  
<sup>186</sup> Fennie C. et al., 2005, Phys. Rev. B, **72**, 100103®;  
<sup>187</sup> Sato T.J. et al., 2003, Phys. Rev. B, **68**, 014432;  
<sup>188</sup> Goian V. et al., 2010, Phase Transitions, **83**, 931;  
<sup>189</sup> Penney T et al., 1969, J.Appl. Phys., **40**, 1234;  
<sup>190</sup> Iliev M.N. et al., 1997, Phys. Rev. B, **56**, 2488;  
<sup>191</sup> Petit S. et al., 2007, Phys. Rev. Lett., **99**, 266604;  
<sup>192</sup> Lee S. et al., 2008, Nature, **451**, 805;  
<sup>193</sup> Sato T.J. et al., 2003, Phys. Rev. B, **68**, 014432;  
<sup>194</sup> Sharma P.A. et al., Phys. Rev. Lett., **93**, 177202;  
<sup>195</sup> Poirier M et al., 2007, Phys. Rev. B, **76**, 174426;  
<sup>196</sup> Park J. et al., 2003, Phys. Rev. B, **68**, 014432;  
<sup>197</sup> Roessli B. et al., 2005, JETP Letters, **51**, 287;  
<sup>198</sup> Demmel F et al., 2007, Phys. Rev. B, **76**, 212402;  
<sup>199</sup> Perdew J. P. et al., 1981, Phys. Rev. B, **23**, 5048;  
<sup>200</sup> Giaquinta D.M. et al., 1992, J.Am. Chem. Soc., **114**, 10952;  
<sup>201</sup> Greedan J.E. et al., 1995, J. Solid Sate Chem., **116**, 118;  
<sup>202</sup> Vajenine G. V. et al., 1996, Chem, Phys. **204**, 469;  
<sup>203</sup> Serrao C.R. et al., 2006, J. Appl. Phys. , **100**, 076104;  
<sup>204</sup> Katsufuji T et al., 2001, Phys. Rev. B, **64**, 104419;  
<sup>205</sup> Scott J.F., 2007, J. Mater. Res., **22**, 2053;  
<sup>206</sup> Wollan E.O et al., 1955, Phys. Rev., **100**, 545;  
<sup>207</sup> Takeda T et al, 1974, J. Phys. Soc. Jpn., **37**, 275;  
<sup>208</sup> Kikuchi K et al., 1999, J. Solid State Chem, **146**, 1;  
<sup>209</sup> Chmaissem O. et al., 2001, Phys. Rev. B., **64**, 134412;  
<sup>210</sup> Lee J. H. et al, 2010, Phys. Rev. Lett., **104**, 207204 ;  
<sup>211</sup> Roa-Rojas J. et al., 2008, J. Magn. Magn. Mater.,**320**, e104;

- 
- <sup>212</sup> Preethi-Meher K.R.S. et al., 2009, J. Appl. Phys., **105**, 034113;  
<sup>213</sup> Alvarez-Serrano I. et al., 2010, J. Am. Ceram. Soc., **93**, 2311;  
<sup>214</sup> Shvartsman V.V. et al. 2008, Phys. Rev. Lett. **101**, 165704.  
<sup>215</sup> Fujioka Y. et al., 2006, J. Phys. Chem. B, **110**, 777;  
<sup>216</sup> Catalan G. et al., 2009, Adv. Mater., **21**, 2463;  
<sup>217</sup> Yuan G.L. et al., 2006, Appl. Phys. Lett., **92**, 202904;  
<sup>218</sup> Kan D. et al, 2009, J. Mater. Sci., **44**, 5102;  
<sup>219</sup> Levin I. et al., 2010, Phys. Rev. B, **81**, 020103;  
<sup>220</sup> Khomchenko V.A. et al., 2010, Mat. Res. Bull., **45**, 426;  
<sup>221</sup> Levin I et al., 2011, Chem. Matter., **23**, 2166;  
<sup>222</sup> D.Y. Smith, Dispersion theory, sum rules, and their application to the analysis of optical data, in Handbook of Optical Constants of Solids, ed. E.D. Palik, Academic Press, San Diego 1998, p. 35-68  
<sup>223</sup> Petzelt J. and Dvořák V., 1984, *Infrared Spectroscopy of Structural Phase Transitions in Crystals*, in Vibrational Spectroscopy of Phase Transitions, p. 55, Eds. J. Owen and Z. Iqbal, Academic Press,  
<sup>224</sup> Comes R et al., 1968, Solid State Commun. **6**, 715;  
<sup>225</sup> Buixaderas E. et al., 2004, Ferroelectrics, **308**, 131;  
<sup>226</sup> B.A. Strukov and A.P. Levanyuk, Ferroelectric Phenomena in Crystals, Springer, Berlin 1998.  
<sup>227</sup> Ostapchuk T. et al., 2001, J. Phys.: Condens. Matter. **13**, 2677;  
<sup>228</sup> Ostapchuk T. Et al., 2004, Ferroelectrics **298**, 211;  
<sup>229</sup> Eisner I.Ya., 1960, Bull. Acad. Sci. USSR, Phys. Ser. **24**, 1327;  
<sup>230</sup> Polina R.J. et al., 1975, Phys. Rev. B **12**, 362;  
<sup>231</sup> Yagi T. et al., 1969, J. Phys. Soc. Jpn. **26**, 865;  
<sup>232</sup> Matsuo T. et al., 1977, Sol. St. Commun. **21**, 923;  
<sup>233</sup> Rousseau D.L. et al., 1981, J. Raman Spectr. **10**, 253;  
<sup>234</sup> Kamba S. et al., 2007, Phys. Rev. B, **75**, 024403;  
<sup>235</sup> Reaney I.M. et al., 2011, J. Am. Ceram. Soc., **94**, 2242;  
<sup>236</sup> Momozawa N. et al., 1985, J. Phys. Soc. Jpn, **54**, 3895;  
<sup>237</sup> Utsumi S. et al., 2007, J. Phys. Soc. Jpn, **76**, 034704;  
<sup>238</sup> Chun S. H. et al., 2010, Phys. Rev. Lett., **104**, 037204;  
<sup>239</sup> Zhao Y.M. et al., 2004, J. Magn. Magn. Mater. **281**, 214;  
<sup>240</sup> Iqbal M. J. et al., 2009, Mater. Chem. Phys., **118**, 308;  
<sup>241</sup> Kimura T, 2007, Annu. Rev. Mater. Res., **37**, 387;  
<sup>242</sup> Talbayev D. et al., 2008, Phys. Rev. Lett. **101**, 097603;



---

## Publications

My publications related to the thesis

1. A. Belik, S. Kamba, M. Savinov, D. Nuzhnyy, M. Tachibana, E. Takayama-Muromachi and V. Goian, „Magnetic and Dielectric Properties of Hexagonal  $\text{InMnO}_3$ ”, *Physical Review B*, **79**, 054411 (2009);
2. V. Goian, S. Kamba, J. Hlinka, P. Vaněk, A.A. Belik, T. Kolodiazhnyi, J. Petzelt, „Polar phonon mixing in magnetoelectric  $\text{EuTiO}_3$ “, *European Physical Journal B*, **71(3)**, 429, (2009);
3. S. Kamba, V. Goian, M. Savinov, E. Buixaderas, D. Nuzhnyy, M. Maryško, M. Kempa, J. Hlinka, K. Knížek, P. Vaněk, P. Novák, J. Buršík, Y. Hiraoka, T. Kimura, K. Kouřil, H. Štěpánková, „Dielectrics, magnetic and, lattice dynamics properties of Y-type hexaferrite  $\text{Ba}_{0.5}\text{Sr}_{1.5}\text{Zn}_2\text{Fe}_{12}\text{O}_{22}$ “, *Journal of Applied Physics*, **107**, 1041099 (2010);
4. K. Z. Rushchanskii, S. Kamba, V. Goian, P. Vaněk, M. Savinov, J. Prokleška, D. Nuzhnyy, K. Knížek, F. Laufek, S. Eckel, S. K. Lamoreaux, A. O. Sushkov, M. Ležaić and N. Spaldin, „A multiferroic material to search for the permanent electric dipole moment of the electron“, *Nature Materials*, **9**, 649 (2010);
5. J.Hyuk Lee, L. Fang, E. Vlahos, X. Ke, Y. W. Jung, L. F. Kourkoutis, Jong-Woo Kim, Philip J. Ryan, T. Heeg, M. Roeckerath, V. Goian, M. Bernhagen, R. Uecker, P.C. Hammel, K. Rabe, S. Kamba, J. Schubert, J. W. Freeland, D. A. Muller, C. J. Fennie, V. Gopalan, E. Johnston-Halperin & D. G. Schlom, „A strong ferroelectric ferromagnet created by means of spin-lattice coupling“, *Nature*, **466**, 954(2010) + electronic supplement <http://www.nature.com/nature/journal/v466/n7309/extref/nature09331-s1.pdf>
6. V. Goian, S. Kamba, C. Kadlec, D. Nuzhnyy, P. Kužel, J. Agostinho Moreira, A. Almeida, P.B. Tavares, „THz and infrared studies of multiferroic hexagonal  $\text{Y}_{1-x}\text{Eu}_x\text{MnO}_3$  ( $x=0 - 0.2$ ) ceramics”, *Phase Transitions*, **83**, 931(2010);
7. K.R.S. Preethi Meher, M. Savinov, S. Kamba, V. Goian and K.B.R Varma, „Structure, dielectric and magnetic properties of  $\text{Sr}_2\text{TiMnO}_6$  ceramics”, *Journal of Applied Physics*, **108**, 094108 (2010);
8. V. Goian, S. Kamba, D. Nuzhnyy, P. Vaněk, M. Kempa, V. Bovtun, K. Knížek, J. Prokleška, F. Borodavka, M. Ledinský and I. Gregora, „Dielectric, magnetic and

- 
- structural properties of novel multiferroic  $\text{Eu}_{0.5}\text{Ba}_{0.5}\text{TiO}_3$  ceramics”, *Journal of Physics:Condensed Matter*, **23**, 025904(2011);
9. J.Hyuk Lee, L. Fang, E. Vlahos, X. Ke, Y. W. Jung, L. F. Kourkoutis, Jong-Woo Kim, Philip J. Ryan, T. Heeg, M. Roeckerath, V. Goian, M. Bernhagen, R. Uecker, P.C. Hammel, K. Rabe, S. Kamba, J. Schubert, J. W. Freeland, D. A. Muller, C. J. Fennie, V. Gopalan, E. Johnston-Halperin&D. G. Schlom, „A strong ferroelectric ferromagnet created by means of spin-lattice coupling“, *Addendum - Nature*, **476**, 114 (2011);
  10. V. Goian, S. Kamba, S. Greicius, D. Nuzhnyy, S. Karimi, and I. M. Reaney, „Terahertz and Infrared Studies of Antiferroelectric Phase Transition in Multiferroic  $\text{Bi}_{0.85}\text{Nd}_{0.15}\text{FeO}_3$ “, *Journal of Applied Physics*, in press;
  11. M. Kachlik, K. Maca, V. Goian, and S. Kamba, „Processing of phase pure and dense bulk  $\text{EuTiO}_3$  ceramics and their infrared reflectivity spectra”, submitted to *Materials Letters*;
  12. C. Kadlec, V. Goian, K. Z. Rushchanskii, P. Kužel, M. Ležaić, K. Kohn, R. V. Pisarev, and S. Kamba, “Terahertz and infrared spectroscopic evidence of phonon-paramagnon coupling in piezomagnetic  $\text{YMnO}_3$ ”, submitted to *Phys. Rev. B*;

---

## List of Tables

<i>Table I</i> Mode parameters obtained from the fits at 100 and 900 K.	116
<i>Table II</i> Factor group analysis of all vibrational modes (including acoustic) in various crystal phases of $\text{Bi}_{1-x}\text{Nd}_x\text{FeO}_3$ .	117

---

## List of variables

$n^*$ - complex refractive index	$n$ - real refractive index
$k$ - imaginary refractive index	$R_{(k,f)}$ - Reflectivity
$T_{(k,f)}$ - Transmittance	$q$ - wave vector of the phonon modes
$\omega$ - frequency of the phonon modes	$\omega_{TO}$ - transverse optical phonon frequency
$\omega_{LO}$ - longitudinal optical phonon frequency	$\alpha$ - coupling constant
$\gamma$ - damping of the phonon modes	$\chi_{e,m}$ -(electric or <b>m</b> agnetic) susceptibility
$\gamma_{TO}$ - damping of the transverse optical phonon	$\epsilon^*$ - complex dielectric permittivity
$\gamma_{LO}$ -damping of the longitudinal phonon	$\mu^*$ - magnetic permeability
$\Delta\epsilon$ - dielectric strength of the polar phonon	$\epsilon'$ - permittivity (real part of $\epsilon^*$ )
$\epsilon''$ - dielectric losses (imaginary part of $\epsilon^*$ )	$\epsilon'(0)$ - static permittivity
$\mu'$ - real part of magnetic permeability	$\omega_R$ - relaxation frequency
$\mu''$ - imaginary part of magnetic permeability	$\hat{S}$ -vector spin operator;
$J$ - exchange integral	$\tilde{\delta}$ - complex phase shift
$\lambda_0$ - wavelength of the radiation in vacuum	$H$ - Hamiltonian operator
$\tilde{r}_f, \tilde{t}_f$ -Fresnel coefficient from the thin film	$e_i$ - effective charge
$E_{i,r,t}$ - incident, reflected and transmitted electric field component of the electromagnetic field	
$d$ - thickness of the thin film	
$f$ - oscillator strength ( $=\Delta\epsilon/\omega^2$ ) of the polar phonon	
$\epsilon_{\infty}$ - permittivity for frequencies much higher than the phonon frequencies	
$T_{AFD}$ - temperature of antiferrodistortive phase transition	
$T_C$ - Currie temperature (ferroelectric phase transition temperature)	
$\Gamma_j$ - damping of the $j^{\text{th}}$ uncoupled (bare) mode	

---

## List of abbreviations

AFD – Antiferrodistortive	IMO – InMnO <sub>3</sub>
AFE – antiferroelectric	INS – inelastic neutron scattering
AFM – antiferromagnetic	IR - infrared
<b>B</b> – magnetic field	LAO – LaAlO <sub>3</sub>
BZ – Brillouin zone	LSAT – (LaAlO <sub>3</sub> ) <sub>0.29</sub> –(SrAl <sub>1/2</sub> Ta <sub>1/2</sub> O <sub>3</sub> ) <sub>0.71</sub>
BNFO – Bi <sub>0.85</sub> Nd <sub>0.15</sub> FeO <sub>3</sub>	ME – magnetoelectric
BSZFO – Ba <sub>0.5</sub> Sr <sub>1.5</sub> Zn <sub>2</sub> Fe <sub>12</sub> O <sub>22</sub>	MW – microwave
CM – Central Mode	NGO – NdGaO <sub>3</sub>
DM - Dzyaloshinskii-Moriya (mechanism)	<b>P</b> <sub>s</sub> – spontaneous polarization
DSO – DyScO <sub>3</sub>	PE – paraelectric
<b>E</b> – electric field	PM – paramagnetic
EBTO – Eu <sub>0.5</sub> Ba <sub>0.5</sub> TiO <sub>3</sub>	PT – phase transition
EBSTO – Eu <sub>0.5</sub> Ba <sub>0.25</sub> Sr <sub>0.25</sub> TiO <sub>3</sub>	SHG – second harmonic generation
EDM – electric dipole moment	SM – soft mode
ETO - EuTiO <sub>3</sub>	SMO – SrMnO <sub>3</sub>
FE – ferroelectric	STMO – Sr <sub>2</sub> TiMnO <sub>6</sub>
FIR – far infrared	STO – SrTiO <sub>3</sub>
FM – ferromagnetic	T <sub>N</sub> – Néel temperature
	THz – terahertz
	TO – transverse optical (phonon)
	TM - Transition Metals